Remote Focusing in Optical Microscopy

A thesis submitted to the University of Exeter for the degree of

Doctor of Philosophy in Physics.

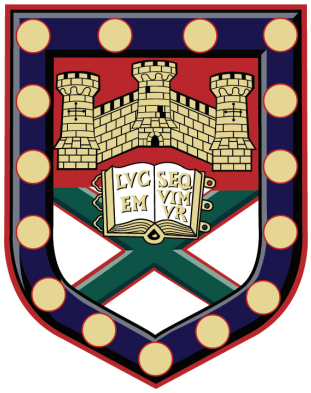

Sharika Mohanan

Department of Physics, University of Exeter.

March 2022

COPYRIGHT DECLARATION

AUTHOR DECLARATION

The work presented in this thesis is my own except for the following:

Chapter 4 was joint research performed along with Dr. Michele Gintoli and Dr. Elizabeth Williams. Their individual contributions have been stated in section 4.6.

Sharika Mohanan, March 2022.

ABSTRACT

Current developments in optical microscopy aim to visualise complex dynamic biomolecular processes close to their native state. To capture transient phenomena, rapid three-dimensional stacks are acquired by translating the objective or sample stage to refocus into different depths of the specimen. Such conventional refocusing strategies introduce vibrational artefacts when imaging specimens that are in direct contact with the immersion media of the objective.

Remote focusing is a methodology in which agitation-free refocusing can be performed using high numerical aperture (NA) objectives without compromising on resolution or imaging speed. It compensates for aberrations from the imaging objective by introducing equal and opposite aberration with a second microscope placed in reverse to the first. As the NA of the imaging objective increases, there are significant constraints placed on the tolerance in optical design to reach perfect phase-matching condition.

In the first part of the thesis, the computational model developed to predict the performance of remote focusing microscopes is presented. From the model, the increased sensitivity of high-NA systems to magnification mismatch is inferred where the diffraction limited volume reduces by half for a 1% error.

Informed by the sensitivity analysis, the decrease in resolution across depth for a remote focusing microscope with a 4% magnification mismatch is demonstrated. A protocol for magnification and resolution characterisation is presented and is applied to a novel Spinning Disk Remote Focusing microscope. The microscope is then applied to perform live volumetric imaging to study the normal neural activity of *Platynereis dumerilii* larvae. The studies presented here paves way for a standardised characterisation of remote focusing systems allowing for wider implementation.

In the final part of the thesis, the spherical aberration generated by the correction collar on an immersion objective is exploited to compensate for residual spherical aberration in an ideal remote focusing system. The wavefront aberrations are measured using a Shack-Hartmann sensor and sub-resolution beads are imaged for point spread function measurements. Results from the Shack-Hartmann measurements show a 60% increase in axial range compensated for spherical aberration. In addition, the contribution of off-axis aberrations to the overall image quality at defocussed positions is explored further.

PUBLICATIONS & PRESENTATIONS

Mohanan S, Corbett AD. (2020) Sensitivity of remote focusing microscopes to magnification mismatch, Journal of Microscopy, DOI:10.1111/jmi.12991.

Gintoli, M., **Mohanan, S.**, Salter, P., Williams, E., Beard, J. D., Jekely, G., & Corbett, A. D. (2020). Spinning disk-remote focusing microscopy. Biomedical Optics Express, 11(6), 2874-2888.

Mohanan S, Corbett AD. (2021) Remote Focusing Microscopes - Tolerance Analysis. Focus on Microscopy, Virtual. Conference presentation.

Mohanan S, Corbett AD. (2019) Theory and Practice of Remote Focusing in Optical Microscopy. Focus on Microscopy, London. Conference presentation.

ACKNOWLEDGEMENTS

I would like to start by thanking my sister who has had the unenviable task of being my champion. I am extremely grateful to my mother and aunt for the unconditional support they have provided during my studies. I would like to thank my friends Kamala and Harshi, for always lending a ear despite us being in three different time zones. And to Maria, for exploring the Devon countryside with me.

This thesis would not be possible without Dr. Alex Corbett and the valuable feedback they have supplied towards my research and writing. I thank them for bringing clarity to my ideas. I would like to thank Prof. Christian Soeller for being generous with their time and for the many helpful discussions - I always left our combined group meetings with renewed enthusiasm. Many thanks to EMPS college for extending my funding for an extra six months - a considerable portion of the research presented in this thesis was made possible because of it. I gratefully acknowledge the Biophysics group and the Physics department for providing a wonderful environment to practise my research, teaching and communication skills.

TABLE OF CONTENTS

CHAPTER 1

INTRODUCTION

1.1 A Brief History

Optical microscopes have been the pivotal tool in aiding the visualisation of biological processes that are invisible to human eyes. The magnification properties of optical lenses and its ability to enhance human vision has been known since ancient times [1]. Its application in studying living systems can be traced back to the 17th century with Antonie van Leeuwenhoek using a single lens microscope to study microorganisms [2]. He was an amateur lens maker and kept the fabrication process a secret but his lenses with diameters as small as 1.5 mm could reach magnifications of up to 270x [3]. His contemporary, Robert Hooke, produced *Micrographia* in 1665 which included detailed illustrations of minute organisms and microstructures [4]. Hooke mostly used compound microscopes for his observations.

Even though simple microscopes produced higher quality images, they were awkward to use especially for lengthy observations. Compound microscopes allowed for an increased overall magnification and improved ergonomics. However, as these systems contained multiple lenses, they suffered from chromatic aberration.

It took about 150 years for compound microscopes to obtain the same image quality as Leeuwenhoek's simple microscope. In 1873, Ernst Abbe showed that a microscope cannot resolve structures beyond a fundamental limit governed by diffraction [5]. This minimum resolvable distance was defined as $D = \frac{\lambda}{2n \sin \alpha}$ where λ is the wavelength of light, n is the refractive index of the medium and $\sin \alpha$ is the angular aperture of the lens. Consequently, even if all imperfections in the design

of optical lenses are overcome, the quality of the final image cannot be improved beyond that predicted by Abbe's diffraction limit. The use of apochromatic lenses, advances in objective lens design and improvements in illumination schemes helped in the construction of diffraction-limited compound microscopes [6].

In current research, improving the image quality beyond the diffraction limit is the motivation behind advances in super-resolution techniques which enable visualisation of intracellular activity [7, 8]. In addition, observing cells, their structure and function, in a minimally invasive manner introduces unique bottlenecks when imaging with the traditional microscope architecture [9].

1.2 Imaging Properties of a Microscope

Most modern microscopes contain two main optical elements. The objective lens which is the lens closest to the sample and the tube lens that focuses the light from the objective on to the detector. In this thesis we have used a standard widefield epifluorescence microscope as shown in Figure 1.1 [10]. An arc lamp is used as the illumination source with the excitation wavelength isolated using a bandpass excitation filter. The dichroic mirror reflects the excitation light into the objective which then illuminates the sample. The excited fluorophores in the specimen emits red-shifted fluorescence which is collected by the same objective lens. The fluorescence emission is separated from the excitation light with the help of the dichroic mirror and the emission filter. A CMOS camera is placed at the focal plane of the tube lens and captures a two-dimensional (2D) image of the sample.

Imaging systems function to collect a portion of the light originating from the object and redirects it to form the image. The objective and tube lens are rotationally symmetric with the optical axis passing through their geometric centres. The maximum cone of light collected by the lens depends on the size of the aperture stop. It is a physical stop in the system that limits the maximum ray angle for a point object on the optical axis and defines the Numerical Aperture (NA). Here,

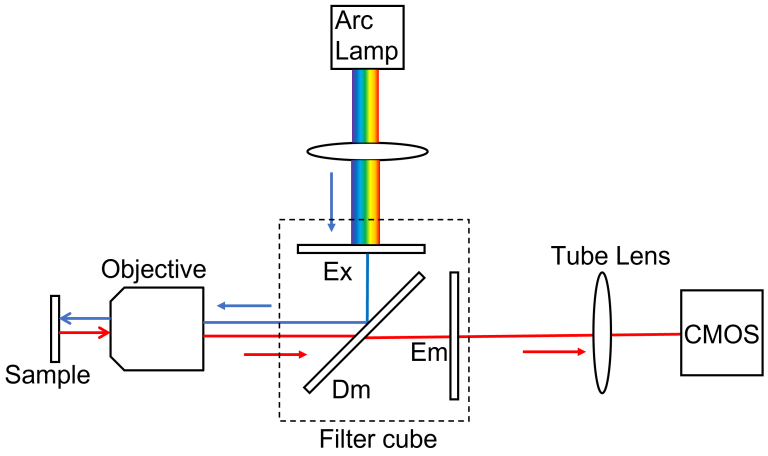

Figure 1.1: A modern epifluorescence microscope where the excitation and emission light pass through the same objective. The filter cube contains the Excitation filter (Ex), Dichroic mirror (Dm) and the Emission filter (Em). The filter cube ensures that the fluorescence signal is isolated from the excitation light.

$\mathrm{NA} = n \sin \alpha$, where α is the semi-angular aperture of the optical system (Figure 1.2a). In a multi-lens system, such as an objective lens, the apparent size of the aperture stop changes as light refracts through lenses placed before and after the stop. The image of the aperture stop from the object space is called the entrance pupil and from the image space is called the exit pupil.

We can study some of the image forming properties of a microscope using geometrical optics. It is a useful approximation when relating spatial scales larger than the wavelength of light. Here, light rays travel outwards from the point source following the rules of rectilinear propagation. When a ray encounters a reflecting or refracting surface it can change direction based on the rules of reflection and refraction.

Under geometrical optics, an imaging system can be reduced to six cardinal planes which allows us to easily calculate the object and image distances in addition to the image size and orientation. The cardinal planes intersect the optical axis to form the cardinal points. Rays incident and exiting the lens appear to refract at the principal planes P and P'. The distance to the object, image and focal planes are defined from the principal planes of the optical system. The second set of cardinal

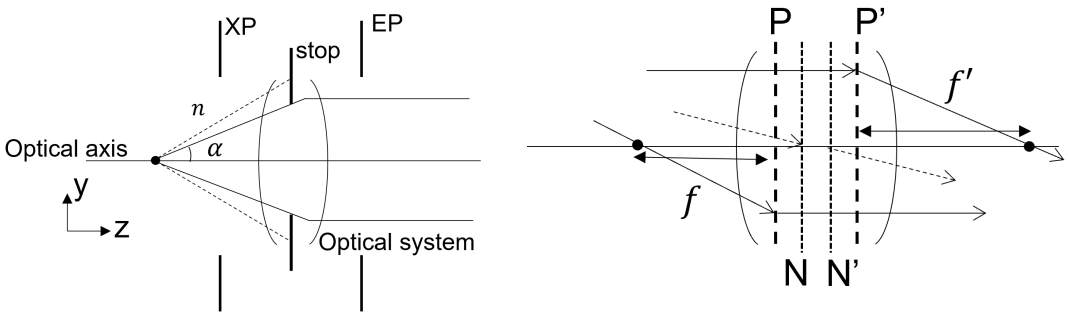

(a) (b)

Figure 1.2: (a) The diameter of the aperture stop determines the maximum cone angle entering the optical system and therefore limits the amount of light forming the image. EP- entrance pupil, XP- exit pupil. The position of the aperture stop and the corresponding pupil planes depend on the imaging geometry. For example, if the point object in the figure is axially shifted (in z), the aperture that limits the maximum ray angle might change. (b) Schematic depicting the cardinal planes. P and P' are the principal planes. N and N' are the nodal planes. f and f' are the focal points in the object and image space respectively. The cardinal planes are fixed for a given optical system.

planes are the nodal planes. A ray aimed at the front nodal point N emerges from the back nodal point N' undeviated. The final set are the focal planes. Rays that pass through the front focal point f emerge parallel to the optical axis in the image space and in reverse, rays passing through the back focal point f' are parallel to the optical axis in the object space.

For easy calculation of the imaging properties using geometrical optics, we only consider shallow rays that form small angles with respect to the optical axis. This is called paraxial approximation where $\sin\theta = \tan\theta = \theta$ and $\cos\theta = 1$ when in reality the terms can be expanded as

$$\sin\theta = \theta - \frac{\theta^3}{3!} + \frac{\theta^5}{5!} - \frac{\theta^7}{7!} + ... \tag{1.1a}$$

$$\cos\theta = 1 - \frac{\theta^2}{2!} + \frac{\theta^4}{4!} - \frac{\theta^6}{6!} + ... \tag{1.1b}$$

Equations derived from paraxial approximation is called first-order theory. An important assumption made here is that all rays emerging from a point source on

the optical axis and incident on the lens travel the same optical path length as the ray along the optical axis.

1.2.1 Magnification

The primary function of the microscope is to magnify fine structures that are invisible to the human eye. To derive the magnification from geometrical optics, we make a further simplification by considering thin lenses. For a thin lens, the principal and nodal planes coincide into a single plane. As a consequence of paraxial approximation, the relationship between the object (s) and image ($s^{'}$) distance is greatly simplified to give the thin lens equation

$$\frac{1}{f} = \frac{1}{s} + \frac{1}{s'}. \tag{1.2}$$

This is also called the Gaussian lens formula. For a thin lens, the focal lengths $f = f'$. The planes containing the object and the image are termed conjugate planes. If the light direction is reversed, the rays originating from the image plane will be imaged at the corresponding position on the object plane.

A lens, depending on the position of the object, can either magnify or demagnify an extended object (Figure 1.3a). This lateral (x-y) magnification (M_L) of the image can be written as

$$M_L = -\frac{s^{'}}{s} = \frac{n \tan\theta}{n' \tan\theta'}. \tag{1.3}$$

The above equation is also written with respect to the object and image height as $M_L = -\dfrac{h^{'}}{h}$. A negative magnification denotes the inverted orientation of the image with respect to the object.

If we consider two objects that are axially shifted by Δz in three-dimensional (3D) space, each object has a lateral magnification of $M_1 = -\dfrac{h_1^{'}}{h_1}$ and $M_2 = -\dfrac{h_2^{'}}{h_2}$. As shown in Figure 1.3b, we can define the axial magnification, M_A, for the axially shifted objects as

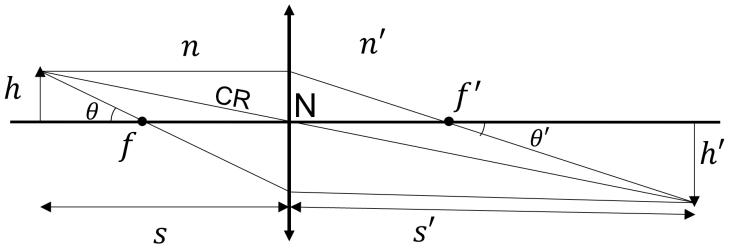

(a)

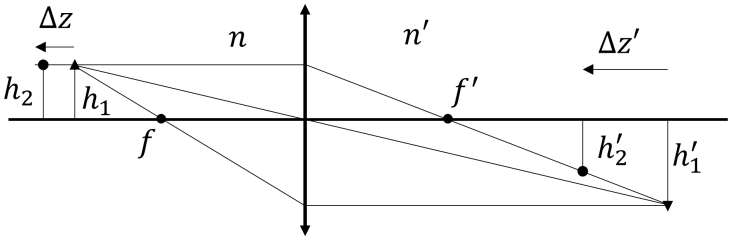

(b)

Figure 1.3: (a) Ray diagram for an extended object imaged by a positive thin lens. (b) Imaging of axially shifted objects.

$$M_A = \frac{\Delta z^{'}}{\Delta z} = \frac{n^{'}}{n} M_1 M_2, \tag{1.4}$$

where n and $n^{'}$ are the refractive indices of the medium in the object and image space respectively. As Δz approaches zero, equation 1.4 reduces to

$$M_A = \frac{n^{'}}{n} M_L^2. \tag{1.5}$$

For example, when imaging with a 40x objective with $n = n^{'} = 1$, an object that has axial planes separated by $\Delta z = 1\,\mu\text{m}$ is imaged $1600\,\mu\text{m}$ apart.

For a lens with a given focal length, increasing the object distance decreases the lateral magnification. Therefore, an object far away seems smaller when compared to the same object placed closer to the lens. This dependence of magnification with distance is an important visual cue in the depth perception for human vision. However, for 3D imaging applications, the depth-dependant magnification property is not desirable as it results in a non-uniform scaling of the 3D image.

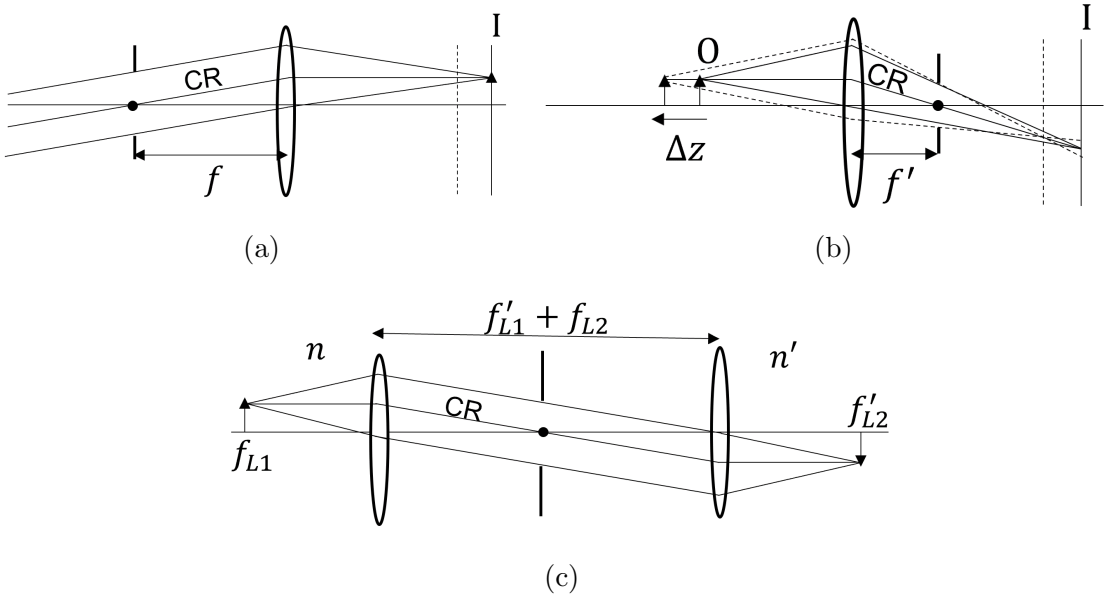

Figure 1.4: Ray diagram for (a) image-space telecentric, (b) object-space telecentric and (c) double telecentric system

Telecentricity

Lens systems can be designed such that the magnification is independent of object distance (s), imaging distance ($s^{'}$) or both. Such systems are termed telecentric. We define the chief ray (CR) which starts from the edge of the extended object, intersects the optical axis at the aperture stop and defines the height of the image (Figure 1.3a). As we aim to build a system where the image height (magnification) is independent of s and/or $s^{'}$, the chief ray needs to be parallel to the optical axis in the object and/or image space. One way to implement telecentricity is to place an aperture stop at the focal planes of the lens.

In an image-space telecentric system (Figure 1.4a), the aperture stop is placed at the front focal plane (f) of the lens. This forces the chief rays in the image space to be parallel to the optical axis and the exit pupil to be imaged at infinity. Here, shifting the imaging plane (I) towards the vertical dashed line introduces defocus centered around the object but with no change in the relative size of the object being imaged.

In an object-space telecentric system (Figure 1.4b), the aperture stop is placed at

the Back focal plane (BFP) ,$f^{'}$, of the lens. The chief rays are parallel to the optical axis in the object space with the entrance pupil imaged at infinity. Objective lenses are usually designed to be object-space telecentric with the aperture stop placed at the BFP [11]. Therefore, objects at an axially shifted position are imaged with the same magnification ensuring we do not zoom in and out of the field of view (FOV) as we find the object of interest. It should be noted that in such a system, axially shifting the image plane (I) does not maintain telecentricity.

A double telecentric system (Figure 1.4c) is an afocal system with the two lenses spaced at the sum of their focal lengths. The aperture stop is set at the common focal plane which is at the BFP of the first lens and at the front focal plane of the second lens. Therefore, the chief ray is parallel to the optical axis in both the object and image space with the exit and entrance pupil imaged at infinity. As the effective focal length for an afocal system is at infinity, the only valid conjugate planes are the planes containing the two focal points f_{L1} and $f^{'}_{L2}$. Therefore, the lateral magnification for an afocal system is defined as $M_L = \frac{f_{L2}}{f_{L1}}$. This makes both the lateral and axial magnification independent of object and imaging distance. For the special case where $\frac{f_{L2}}{f_{L1}} = \frac{n}{n^{'}}$, the lateral and axial magnification are equal (from equation 1.5).

The remote focusing methodology discussed in this thesis requires the construction of two double telecentric systems back-to-back. We show in chapter 3 how telecentricity can be achieved if the distance between the objective and the tube lens is not equal to the sum of their focal lengths.

1.2.2 Resolution

In order to define resolution, we veer away from geometrical optics and consider light propagating as waves. Light waves emitted by the point object diffract as they pass through the lens and interfere with each other as they reach the imaging plane. Therefore, a point object is not imaged as an infinitely small point as predicted

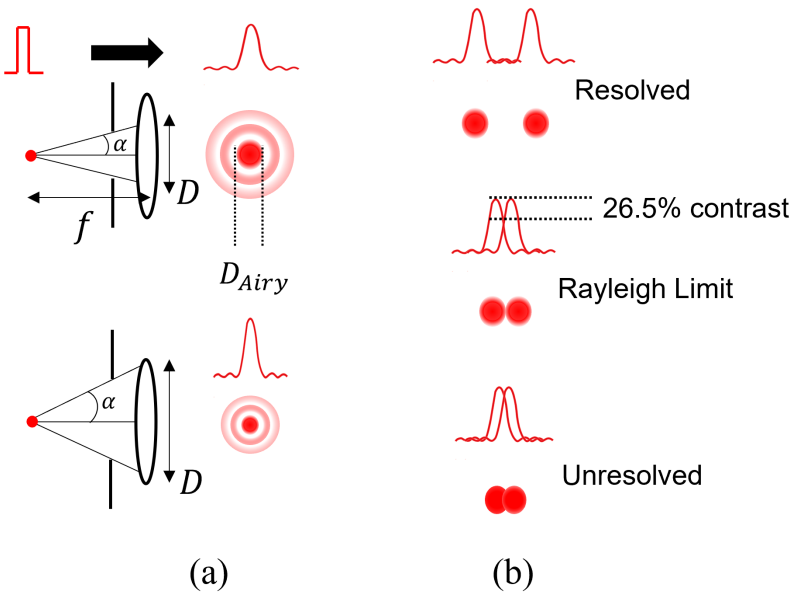

Figure 1.5: (a) Decrease in the diameter of the Airy disc with increase in NA. (b) Resolving two point sources. Rayleigh criterion states that if the peak of one Airy disc falls on the first minima of another, the image is just resolved.

by geometrical optics. Rather the intensity is distributed as a three-dimensional diffraction pattern around the imaging plane. This effect defines the fundamental limit to resolution that can be obtained by an imaging system.

If we assume the objective and tube lens to be perfect lenses, the diffraction pattern is symmetric and periodic along the optical axis and radially around the axis. Figure 1.5a shows the lateral cross section of such a diffraction pattern with the central maxima called the Airy disc. The diameter of the Airy disc is defined as

$$D_{Airy} = \frac{2.44 f \lambda}{D}, \tag{1.6}$$

where f is the focal length, D is the aperture diameter of the objective lens and λ is the imaging wavelength. Equation 1.6 can be written as $D_{Airy} = \frac{1.22\lambda}{\mathrm{NA}}$. Therefore, to get sharper central peaks, the sample should be imaged at shorter wavelengths or by accepting light entering the system at higher angles. When imaging self-luminous objects, such as in an epifluorescence microscope, the imaging objective fully defines the NA of the system.

We can consider the fluorescent specimen under observation to be an extended object made up of countless incoherent point sources. Each of them is imaged as an independent Airy pattern which might overlap depending on its proximity to one another. Resolution is the measure of the smallest distance between two points in the sample that can be imaged by the microscope as two separate objects (Figure 1.5b) or its ability to separate between two closely spaced Airy discs. For a self-luminous object, the minimum resolvable distance in the lateral direction is defined as

$$D_l = \frac{0.61\lambda}{\mathrm{NA}}. \tag{1.7}$$

D_l is also called the Rayleigh limit. In the axial direction, we define the depth of field as

$$D_a = \frac{2n\lambda}{\mathrm{NA}^2}, \tag{1.8}$$

which is the distance within which the microscope can be defocused without affecting the sharpness of the image.

For an oil immersion objective with an NA of 1.45 and imaging at the shortest wavelength ($\lambda = 400\,\mathrm{nm}$), the highest achievable resolution is around 200 nm. Advances in super-resolution techniques makes it possible to break the diffraction limit to achieve resolution in the order of tens of nanometre. Electron microscopes where the electron beams have wavelengths 10^{-5} times that of visible light, can reach resolutions of about 2 Å.

Contrast

Resolution depends on the geometric properties and imaging wavelength of the optical system. Contrast on the other hand is the measure of resolution in the presence of various factors that can affect it. For example, the Rayleigh criterion defines the minimum distance required between the image of two point sources for them to be

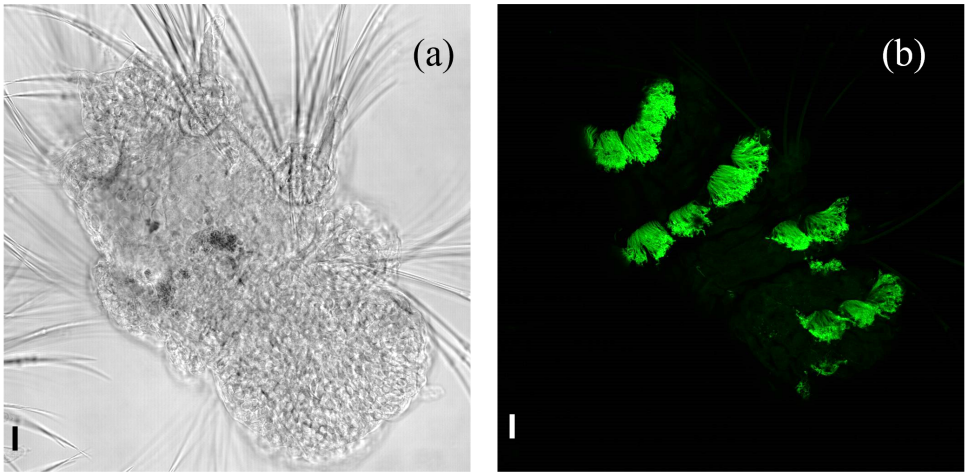

Figure 1.6: The same axial section of a fixed *Platynereis Dumerilii* larva imaged in (a) brightfield and (b) confocal fluorescence mode. Small structures such as the cilia are not visible using brightfield imaging. To image in fluorescence, the acetylated tubulin present in the cilia was attached to a fluorophore allowing for imaging with greater contrast and specificity. Scale bar: 12 µm

resolved. As shown in Figure 1.5b, it assumes that the intensity dip between the two central maxima provides at least a 26.5% contrast [12]. Contrast is reduced due to the presence of noise in the system which can change the relative intensity of the central maximas and therefore make the two Airy discs indistinguishable. Noise can originate from multiple sources such as photon noise, electronic readout noise and stray light. In addition to this, image contrast is reduced due to the presence of aberrations and scattering.

A key part in visualising the specimen using a microscope is how well the features of interest are in contrast with respect to the background. This is not an inherent property of the biological sample. Contrast is generated as the specimen interacts with the illumination light and the imaging optics further modulate the light leaving the sample. In the simplest form, the specimen can be viewed in brightfield mode (Figure 1.6a). Here, contrast is generated by the scattering of the illumination light as it diffracts through the substructures present in the specimen. Therefore, on a bright uniform background formed by the illumination source, features on the sample appear dark if the phase difference introduced produces destructive interference in

the image plane. The disadvantage being that for small, unstained, transparent features, the contrast is very low.

In a fluorescence microscope, the sample should interact with the illumination light and emit fluorescence. If the specimen inherently contains fluorescing molecules, it generates autofluorescence. The main advantage here is the increased specificity in imaging molecules of interest. This can be accomplished by using fluorescent stains that bind to specific molecules (eg: DAPI for staining the nucleus) or modifying proteins to exhibit fluorescence (eg: GFP) or using fluorescent labelled antibodies that bind to specific proteins [10]. No matter which method is used, as only the fluorophores emit light, it indicates the presence and distribution of the specific molecule within the cell. As the dichroic mirror filters out the excitation wavelength, a high contrast image with the bright fluorescence against a dark background is formed.

1.2.3 Aberrations

We have seen that the resolution of an optical system is fundamentally limited by diffraction. In practice, the image of a point source can be further smeared out in the presence of aberrations. These distortions can arise from the optical elements present in the microscope or from the specimen being observed.

Stigmatic or aberration free imaging is obtained if the optical system transforms the spherical wavefront emitted by the point source to a spherical wavefront which converges to a point in the image plane (Figure 1.7a). If the radius of curvature of the incident wavefront is infinite, the transformed wavefront has a radius equal to the back focal length of the lens. In the presence of aberrations, the wavefront at the exit pupil deviates from the reference spherical wavefront (Figure 1.7b). The amount of aberration in an optical system can be determined by calculating the optical path difference of the aberrated wavefront from the reference wavefront to get the wavefront error. A common metric used is the Root Mean Square (RMS)

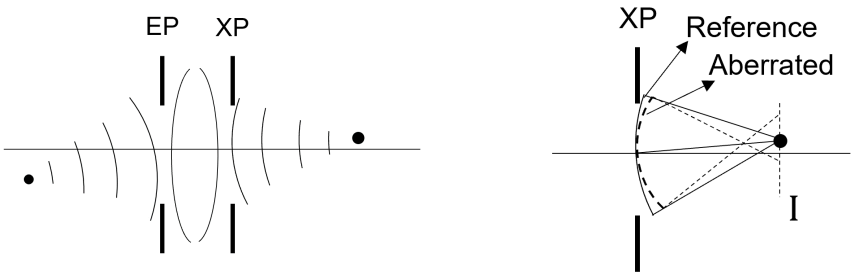

(a) (b)

Figure 1.7: (a) Stigmatic imaging of a point by an optical system. (b) The aberrated wavefront has deviated from the spherical reference wavefront leading to a blurred image at I.

wavefront error which is the statistical deviation of the aberrated wavefront from reference sphere averaged over the entire wavefront.

Aberrations can be chromatic or monochromatic. Chromatic aberrations arise due to dispersion effects of the glass used in the lenses. As refractive index varies inversely with wavelength, each wavelength has a different focal length and is focussed at different positions leading to varying lateral and axial magnifications. Compensation is performed by combining multiple lenses with different dispersion properties to minimise the effective chromatic aberration. If the objective used in the imaging application are apochromats, they are typically designed to correct for 4-5 wavelengths across the visible range.

In the discussion of magnification in section 1.2.1, we considered first order theory or paraxial approximation. This is useful as it provides a simple way to calculate the position and size of the image from just a few optical parameters. However, in order to understand the quality of image produced, the paraxial approximation of $\sin\theta = \theta$ will not provide a complete understanding of the image formation. Paraxiality is lost when considering high aperture angles (as in the case of high-NA objectives), high field angles or both.

To account for the loss of paraxiality, $\sin\theta$ must be expanded to higher order terms. When we restrict the expansion to $\sin\theta = \theta - \frac{\theta^3}{3!}$ the equations derived

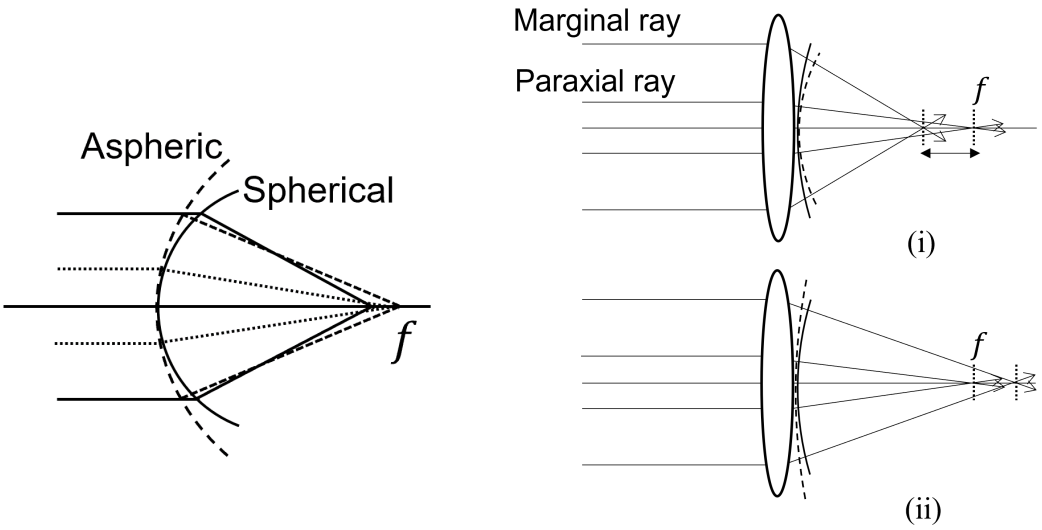

(a) (b)

Figure 1.8: (a)Spherical aberration generated because of imaging with a spherical lens surface. The aspheric surface performs stigmatic imaging of both the paraxial (dotted line) and marginal rays (solid line). (b) Positive (i) and negative (ii) spherical aberration.

falls under the third-order theory. It results in the description of the five classical monochromatic aberrations also called the Siedel aberrations. Spherical aberration is generated for an on-axis object imaged at large aperture angles. The other four aberrations are coma, astigmatism, distortion and field curvature generated when considering off-axis objects at large field angles. Spherical aberration, coma and astigmatism degrade the image quality whereas distortion and field curvature, warp the image without affecting its sharpness. If we consider more terms in the series expansion, it results in explaining higher-order aberrations.

Spherical aberration can be understood as the focal length of the ray changing with ray height for a point object on the optical axis (Figure 1.8). It is possible to construct an ideal optical surface where the optical path lengths for all rays from an object point to the image is a constant. Such an ideal lens surface for stigmatic imaging of a point object placed at the focal point would be hyperbolic [13]. Due to ease of fabrication, lens surfaces are usually designed to be spherical.

As observed in Figure 1.8a, for paraxial rays, the curvature between the spherical and aspherical surface is almost the same leading to stigmatic imaging at the paraxial

focus f. As the marginal ray height increases so does the deviation from the ideal aspheric surface. This leads to the marginal rays being focused at a different axial location which is observed as spherical aberration.

As illustrated in Figure 1.8b, for a system with positive spherical aberration, the focus of the marginal rays falls closer to the lens. For negative spherical aberration, the marginal rays are imaged outside the paraxial focus. Due to this axial spread of the image, the position of best focus is shifted away from the paraxial focus for a system with spherical aberration.

Optical Sine Condition

Spherical aberration can be reduced in a system by either using aspheric lenses or by combining multiple spherical surfaces to minimise the aberration. High-NA objectives work at high aperture angles across a small FOV. Due to the loss of paraxiality, imaging an off-axis object results in the introduction of comatic aberration. For aberration-free imaging of a laterally shifted objects on a unique plane perpendicular to the optical axis, the design of the lens should be optimised to follow the sine condition which is defined as

$$n \sin\theta = M_L n' \sin\theta'. \tag{1.9}$$

This ensures that all aperture zones are imaged with the same magnification ensuring a constant focal length for all rays (Figure 1.9a) [14]. Here, the lateral magnification is the ratio of the sine of the angles rather than the tangent. This results in the principal plane no longer being a 'plane' but a spherical surface (Figure 1.9b). For small ray angles, $\sin\theta = \tan\theta = \theta$ satisfying equation 1.3.

In an optical system corrected for spherical aberration, the consequence of following the sine condition is the correction of coma that has a linear dependence to the object height. As a zero condition, the sine condition is not strictly followed across the entire field and depends on how well the lens design is optimised to equa-

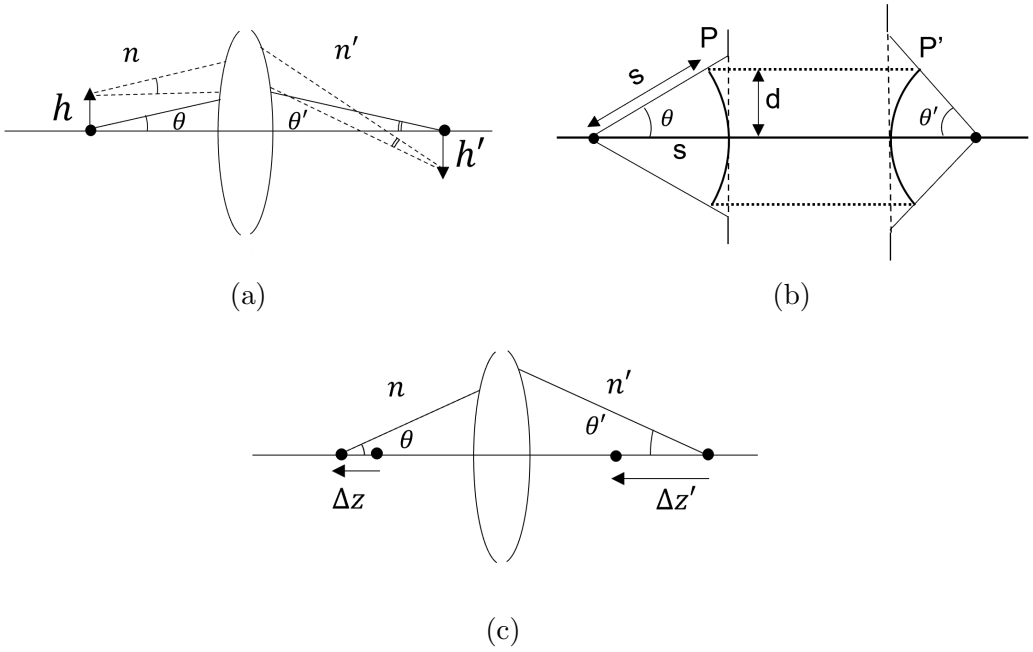

Figure 1.9: (a) Optical system following the sine condition results in aberration free imaging of laterally shifted points. (b) Under sine condition, principal planes P and P' are spherical surfaces centered at the object and image point with the ray height defined as $d = s \sin\theta$. (c) Optical system following the Herschel condition results in aberration free imaging of axially shifted points.

tion 1.9. However, the deviation from it can be quantified and forms a metric to signify the adherence to sine condition across a flat and finite FOV.

Most objectives are 'infinity-corrected', where the objective design is optimised to correct for aberrations at the focal plane. However, this does not ensure that the objective will perform well when imaging objects outside the focal plane.

Herschel Condition

In contrast to the sine condition, the Herschel condition needs to be satisfied to perform stigmatic imaging of axially shifted points (Figure 1.9c). It is written as

$$n \sin^2\left(\frac{\theta}{2}\right) = M_A n' \sin^2\left(\frac{\theta'}{2}\right). \tag{1.10}$$

Here, the optical design is optimised to ensure invariance in axial magnification across the depth of imaging. The consequence of satisfying the Herschel condition is the correction of spherical aberration that has a linear dependence on the axial

position of the object. Using equation 1.5, the above condition can also be written as

$$n \sin\left(\frac{\theta}{2}\right) = M_L n^{'} \sin\left(\frac{\theta^{'}}{2}\right). \tag{1.11}$$

As θ increases, the sine and Herschel condition conflict with each other and therefore cannot be satisfied simultaneously for high-NA systems.

In objective lenses following the sine condition, as the NA increases, the axial region within which perfect imaging can be obtained without introducing significant *depth-dependant spherical aberration* reduces. This has been previously defined as the depth of field, D_a, of the microscope. In contrast, systems following the Herschel condition can perform stigmatic imaging within a very narrow lateral FOV for extended regions along the optical axis.

A perfect imaging system is one where both sine and Herschel conditions are followed simultaneously. As a result, a point source irrespective of its position in 3D object space is imaged stigmatically in the image space. Maxwell's theorems put forward that if an optical system is constructed to have an isotropic magnification of $M_L = M_A = \frac{n}{n^{'}}$, equations 1.9 and 1.10 reduce to $\theta = \theta^{'}$. Such a system behaves more like a plane mirror located between the principal surfaces with no magnification properties ($n/n^{'}$ is close to one even when using immersion media) but provides 3D stigmatic imaging. This is an important imaging condition that remote focusing systems are designed to provide. As objectives used in microscopes have very high magnifications, the method of achieving near-unity magnification is discussed in Chapter 2.

1.2.4 Image Quality

So far, we have looked at the some of the imaging properties of a microscope and factors that can affect the quality of the image formed on the detector. To characterise the microscope, we need to measure the accuracy with which the microscope

relays information from the object plane to the imaging plane. In this thesis, we use a couple of metrics to quantify the departure from ideal imaging conditions.

Point Spread Function

In an aberration-free system, a point source will be imaged as a diffraction-limited 3D Airy pattern known as the Point Spread Function (PSF). More generally, if the point source can be modelled as a delta function, the PSF is the impulse response of the optical system. Therefore, the object convolved with the PSF forms the image. This is written as

$$\text{Object} \otimes \text{PSF} = \text{Image} \tag{1.12}$$

where $\otimes$ is the convolution operator. For a lens with a circular aperture, the 3D PSF is defined as

$$\text{PSF}(u, v) = \left| 2 \int_0^1 P(\rho) J_o(\nu\rho) \exp\left(iu\rho^2/2\right) \rho d\rho \right|^2 . \tag{1.13}$$

u and v are the normalised optical coordinates that scale with the NA and wavelength as

$$u = knz \sin^2 \alpha \tag{1.14a}$$

$$v = knr \sin \alpha. \tag{1.14b}$$

$k = \dfrac{2\pi}{\lambda}$ is the wavenumber, α is the semi-angular aperture of the objective lens, z is the object distance and $r = \sqrt{x^2 + y^2}$ is the radial distance of the object from the optical axis. J_o is the Bessel function of the first kind of zero order. ρ is the normalised pupil radius and $i = \sqrt{-1}$. The PSF is a function of the complex pupil function

$$P(\rho) = A(\rho) \exp(i\phi(\rho)), \tag{1.15}$$

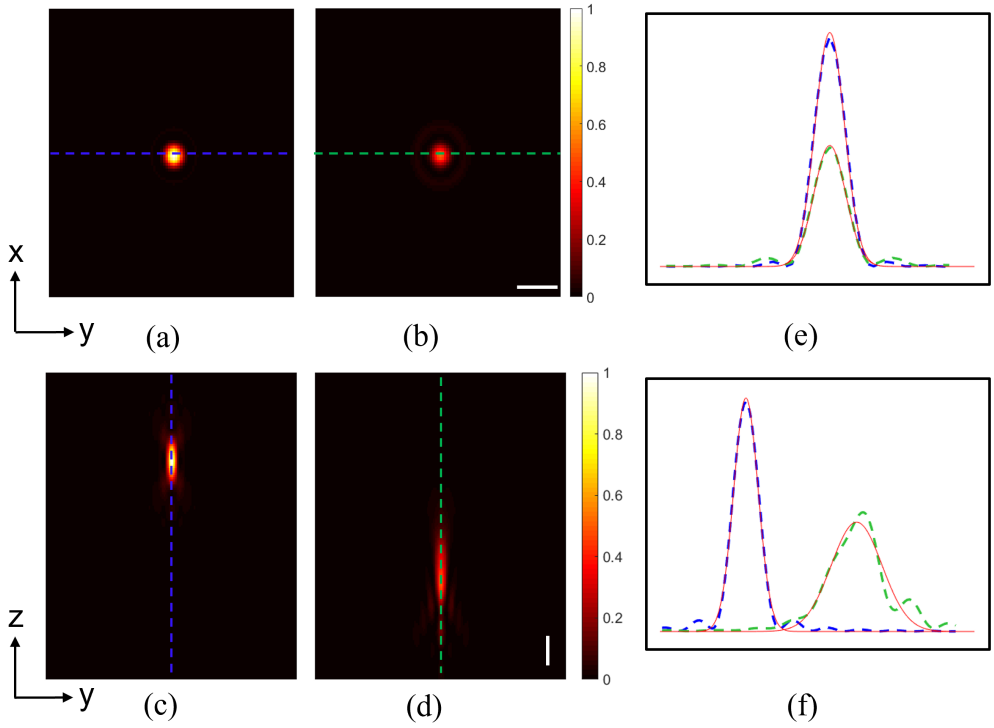

Figure 1.10: (a,c) Lateral and axial normalised intensity PSF for 1.15 NA water immersion objective. (b,d) PSF distorted due to spherical aberration. (e,f) Intensity variation for ideal (blue dashed line) and aberrated (green dashed line) PSF. Solid red lines indicates the Gaussian fit to the central Airy disc from which the FWHM is calculated. Scale bar: 1 µm.

where $A(\rho)$ is the amplitude and $\phi(\rho)$ is the phase of the wavefront over the exit pupil. As discussed in section 1.2.3, due to aberrations, the actual wavefront at the exit pupil may not be strictly spherical. This wavefront error at the pupil plane is reflected in the shape of the PSF (Figure 1.10). When the system has no aberrations, $P(\rho) = 1$. At the focal plane ($z = 0$), Equation 1.13 can be simplified to give the lateral PSF

$$\mathrm{PSF}(0, v) = C \left| \frac{2J_1(v)}{v} \right|^2 . \tag{1.16}$$

J_1 is the first order Bessel function and C is a constant. The central maxima of the Bessel function corresponds to the Airy disc discussed in section 1.2.2. When $v = 3.83$, the Bessel function crosses zero which corresponds to the centre of the first minima of the diffraction pattern. We can calculate the lateral size of the spot

to be $\Delta r = \frac{1.22\lambda}{NA}$ which is the same as equation 1.6. To obtain the axial spread of intensity when $P(\rho) = 1$, equation 1.13 is solved as

$$\mathrm{PSF}(u, 0) = B \left| \frac{\sin(u/4)}{u/4} \right|^2 . \tag{1.17}$$

B is a constant. Along the optical axis, the intensity reaches its first minimum at $u/4 = \pm\pi$ to give $\Delta z = \frac{4n\lambda}{\mathrm{NA}^2}$. It should be noted that the above equations are derived for small angle approximations. However, for high-NA objectives, they still provide a useful measure of the increase in resolution with increasing NA.

To quantify the variation between an 'ideal' PSF to a PSF from a real system, it is common to image sub-diffraction fluorescence beads which can be approximated as point sources [15, 16]. The resulting diffraction pattern in the image space is the impulse response of the microscope and characterises the imaging quality. A consequence of imaging with aberrations is the redistribution of energy from the central Airy disc to the outer rings of the diffraction pattern. It generally leads to reduction in the effective resolution and contrast of the optical system. For example, with the introduction of spherical aberration, light intensity is transferred away from the central maxima to the axial regions of the diffraction pattern (Figure 1.10 b,d).

Ignoring the higher order diffraction rings, the central Airy disc is approximated as a Gaussian function. The Full-Width Half-Maximum (FWHM) of the central maxima is calculated as 2.355 σ, where σ is the standard deviation of the Gaussian fit. The FWHM measure relates to the theoretical resolution as

$$\mathrm{FWHM}_{x,y} = 0.84 D_l \text{ and} \tag{1.18a}$$

$$\mathrm{FWHM}_z = 0.88 D_a, \tag{1.18b}$$

and provides an empirical measure of the effective resolution of the system.

Wavefront error

Another method of assessing the imaging quality of the optical system is by measuring the phase of the wavefront at the exit pupil of the objective. This is the measurement of $\phi(\rho)$ from equation 1.15. The measured wavefront can be decomposed into a series of Zernike polynomials, $Z_k(\rho, \varphi)$, which are a complete set of orthonormal polynomials defined over a unit circle.

$$\phi(\rho, \varphi) = \sum_{k=1}^{\infty} a_k Z_k(\rho, \varphi). \tag{1.19}$$

Here, φ is the azimuthal angle over the pupil. The aberration coefficient, a_k, signifies the contribution of the k^{th} Zernike term to the measured wavefront. The Zernike polynomials are related to classical aberrations such as coma, spherical aberration and astigmatism with higher values of k indicating higher order aberrations. In measuring the phase of the wavefront, the individual Zernike modes contributing to the final PSF shape can be quantitatively assessed. This is an advantage from PSF FWHM measurement techniques. The shape of the PSF might give the seasoned microscopist an idea of the aberration causing image degradation. However, this might not always be straight forward in the presence of multiple aberrations. Another advantage is that wavefront aberrations are additive. If we measure the amount of wavefront error in the system, introducing equal and opposite amounts of the aberration term can cancel it out. By contrast, contributions to the PSF FWHM cannot be easily decomposed.

There are various metrological techniques for wavefront measurement [17, 18]. In this thesis we use a Shack-Hartmann sensor to map the exit pupil of the objective. Details of the sensor setup and analysis of the data are described in Chapter 2.

1.3 3D Imaging

A microscope in the absence of aberrations will produce a sharp image of a thin object placed at the focal plane. When imaging thick biological specimens, the feature of interest extends in all directions. To accurately reconstruct these features, the sample stage or the objective is translated in z to image a series of 2D slices which are stitched together to form a 3D volume (Figure 1.11).

In the widefield epifluorescence microscope illustrated in Figure 1.1, the sample is flood illuminated with excitation light which excites all the fluorescing molecules in the sample. It is obvious from equation 1.8, due to the spread in the axial PSF, the detector is not only capturing the signal emitted by the fluorescing molecules at the focal plane but also the defocused light from the adjacent planes. This defocused light contributes to the background blur in the imaging plane reducing contrast. This effect is further exacerbated if aberrations are present in the imaging system.

One way to ensure improved contrast in 3D imaging is by employing sectioning techniques. In case of electron microscopy, thick samples are sectioned by cutting out ultra-thin layers. The advantage of optical microscopy is that sectioning can be performed without destroying the sample. In such sectioning techniques, spatial sparsity of the fluorescence signal is induced by selective illumination of a point or plane of interest and isolating detection to the corresponding region. In the case of samples that have sparse features, sectioning may not be required if the contrast in the focal plane is not diminished.

1.3.1 The Need for Agitation-free Refocusing

To better understand the structure and function of biological systems, it is essential to capture dynamic molecular processes close to their natural conditions. This requires imaging specimens in-vivo which adds an extra dimension of time to the image acquisition. Depending on the process being observed, the image scanning should be fast enough to capture its effect across the 3D volume. This requires rapid

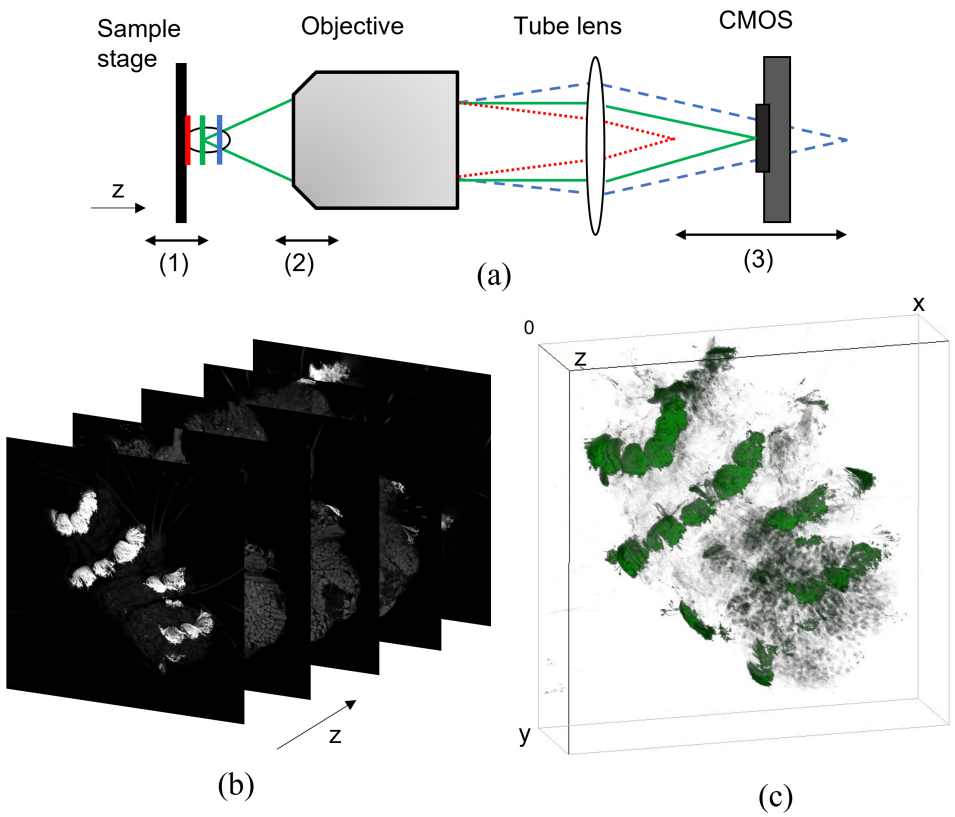

Figure 1.11: (a) For a microscope to image at different axial positions, either the sample stage (1) or the objective(2) is translated. A possible alternative is shifting the camera (3) in z to refocus the system. (b) Series of x-y slices taken at different depths. (c) They are stitched together to form a volumetric image.

movement of the objective or sample stage.

Biological specimens are usually imaged using immersion or dipping objectives. This is so that the refractive index of the immersion media matches closely with the index of the sample. It is well known that index mismatch can lead to the introduction of spherical aberration [19, 20]. As the sample is in contact with the objective, rapid movement of the objective lens or the sample stage to refocus the microscope into different depths introduces vibrational artefacts. This can hinder the observation of transient biological phenomena or even harm the specimen. In addition to this, translating these relatively heavy components can reduce the temporal resolution of the system.

It is then advantageous to decouple refocusing from the object space to a remote location in the optical train of the microscope. As seen in Figure 1.11a, defocused positions in the sample (red and blue solid vertical lines) shifted by Δz will be focused at axial locations $\frac{n'}{n} M_L^2 \Delta z$ in the image space. It is then possible to remotely focus the microscope into different planes in the sample by moving the camera axially. However, translating a heavy camera across magnified axial distances will be time consuming. In addition to this, the objective is designed to match the sine condition and not the Herschel condition. Refocusing to axially shifted positions introduces spherical aberration that increases linearly with z.

In the next section, we provide a brief review of methodologies that have been implemented for agitation-free refocusing which compensate for both defocus and depth-dependant spherical aberration.

1.4 Agitation-free Refocusing methodologies

Refocusing strategies fall into two categories - passive and active methods. In passive refocusing, optical elements are inserted into the path of microscope which allows for simultaneous imaging of multiple depths in the sample. In active methods, each depth is corrected for defocus and imaged in a sequential manner.

1.4.1 Passive Refocusing

As discussed in section 1.3.1, agitation-free refocusing can be accomplished by shifting the position of the detector with respect to the tube lens. In the study presented in references [21] and [22], the temporal limitation of translating the detector was circumvented by splitting the detection paths into two. A camera placed in each of these optical paths imaged a distinct axial plane. The two depths were separated only by 300 nm as any further shift would introduce depth-dependant spherical aberration. If additional axial planes are to be imaged using this method, multiple cameras are required, introducing Signal to Noise Ratio (SNR) limitations and increasing system complexity.

Abrahamsson et al developed multifocus microscopes which introduce distorted diffraction gratings into the Fourier plane [23]. The shape of the grating pattern is custom-made to compensate for spherical aberration introduced at specific depths in the object space. These distinct axial planes are laterally separated on the detector allowing for instantaneous imaging of the sample volume in a single exposure of a large sensor chip camera. Using this method, they have imaged nine axial planes covering a 3.5 micron depth using a 1.4 NA 100x oil immersion objective.

Light field microscopes were further developed by Prevedel et al for performing snap-shot volumetric imaging of neural activity in a whole *C. Elegans* and in the brain of a larval zebrafish [24]. In this method, a lenslet array is placed at the native imaging plane which is in turn imaged on to the camera sensor using a set of relay lenses. In such a setup, both the spatial and angular information of the wavefront is sampled by the lenslet array. Due to the curvature of the wavefront from defocussed positions, they are imaged in a spatially shifted position on the detector. Therefore, light field microscopes have an inherent trade-off between the extended depth of field of imaging and the spatial resolution of the microscope.

Other passive techniques include the use of phase masks to engineer the pupil function of the objective to reduce its sensitivity to defocus [25]. This method has

been implemented along with a light sheet fluorescence microscope to scan through samples at 70 volumes per second (vps) with a ten-fold increase in the depth of field. As introducing a phase mask modifies the Optical Transfer Function of the objective, the images require post-processing using deconvolution techniques to retrieve the original spatial resolution.

1.4.2 Active Refocusing

Active refocusing methods include the use of variable focal length lenses such as Electro Tunable Lenses (ETL) and Tunable Acoustic Gradient (TAG) lenses. Fahrbach et al have used ETLs along with light sheet microscopes for rapid scanning across the focal volume [26]. The focal length of ETLs is adjusted by electrically tuning the curvature of the meniscus between two immiscible liquids. When placed at the Fourier plane of the optical system, it changes the effective focal length of the objective. However, ETLs and TAG lenses cannot compensate for high-NA defocus for a large axial range [27, 28]. TAG lenses combined with light sheet microscopes have been implemented to provide adaptable patterned illumination [29]. As shown in Figure 1.12c, such imaging schemes deliver light to portions of the sample only where and when necessary, greatly reducing phototoxicity and data size.

Another low-NA refocusing methodology consists of using an Alvarez lens pair. Here, the effective focal length is tuned by laterally shifting the lens pair with respect to each other. The Alvarez lenses have a cubic surface profile and are therefore difficult to fabricate. Development of diffractive lens elements with the lateral shift implemented using galvo-scanning has allowed for its application in confocal microscopy [30].

Deformable mirror (DM) based refocusing, coupled with a two-photon microscope has been used to study the neuronal activity in intact *Drosophila* brain by Žurauskas et al in [31]. In a SNR limited live specimen, the spatial resolution was reduced to increase the temporal resolution of the system to achieve 2Hz of vol-

umetric scanning. Despite introducing complexity in instrumentation, DM based approaches have the added flexibility of being able to correct for both system and sample induced aberrations.

To summarise the different agitation-free refocusing methods, passive techniques have the advantage of improved temporal resolution. However, both multifocus and light field microscopes come with reduced flexibility in choosing the planes of interest within the sample volume as the optical elements are selected for a specific FOV. In contrast, despite being relatively slow, active methods allow for arbitrary selection of the axial planes of interest.

1.5 Remote Focusing and 3D Imaging

In this thesis, we have implemented the agitation-free refocusing method called 'Remote Focusing' (RF) as developed by Botcherby et al in reference [32]. The depth-dependant spherical aberration at defocused positions is cancelled by introducing a second matching-NA microscope in reverse with the first. This forms a diffraction-limited 3D image around the focal plane of the second objective. However, as stigmatic imaging requires the object volume to be imaged with a magnification of $\frac{n}{n'}$, a third microscope is used to magnify and scan through the remote volume. The method by which RF cancels aberration at defocussed positions is explained in detail in Chapter 2. In this introduction chapter, we focus on the application of remote focusing in volumetric imaging.

In chapters 2, 3 and 5 of this thesis, RF has been implemented along with an epi-fluorescence widefield microscope. Widefield imaging is the simplest volumetric imaging modality wherein the entire specimen is excited for fluorescence (Figure 1.12). Each image acquired with this technique contains low spatial frequency components from defocused positions. Therefore, high spatial frequency information from the focal plane is imaged with low-contrast. It should be noted here that in this thesis, widefield modality is implemented only when imaging sparse bead sam-

ples. When using RF to image thick biological samples, it should be implemented along with sectioning techniques to remove out-of-focus information.

Ideally, the applied refocusing technique should not limit the spatial and temporal resolution of the microscope. For example, ETL and TAG lenses can only be implemented for low-NA refocusing. These two techniques and DM-based refocusing require extensive calibration procedures to ensure each depth is accurately compensated for defocus. Remote focusing can be used with high-NA objectives and once aligned, requires no further calibration. Compared to passive refocusing techniques such as multifocus and light field microscopes, RF does not restrict the accessible FOV within the specimen. This allows for imaging of the sample features with high fidelity and the temporal resolution limited only by the camera speed. One added advantage from objective or stage scanning is the possibility of selective illumination within the sample (Figure 1.12c). In the following sections, I present the implementation of RF along with various sectioning techniques.

Confocal Laser Scanning Microscopy

Confocal laser scanning microscopy (CLSM) is the most widely used sectioning method for routine biological imaging [33]. The illumination beam is focused into a diffraction-limited spot within the sample. The image of the FOV is built by illuminating each pixel in sequence (Figure 1.12). Sectioning or removal of fluorescence signal outside the depth of field is implemented by introducing a pinhole at the imaging plane conjugate to the position of the illumination spot. This allows CLSM to provide high contrast images compared to widefield fluorescence microscopy. In addition to improved contrast, CLSM provides increased resolution, usually around 1.4x better than a widefield microscope.

Due to the pixel by pixel scanning of the sample, confocal systems are inherently speed limited for volumetric imaging. Improvement in the speed of image acquisition can be implemented by scanning line illumination back and forth across the focal plane (x-y) and replacing the pinhole with a slit. This improves on the temporal

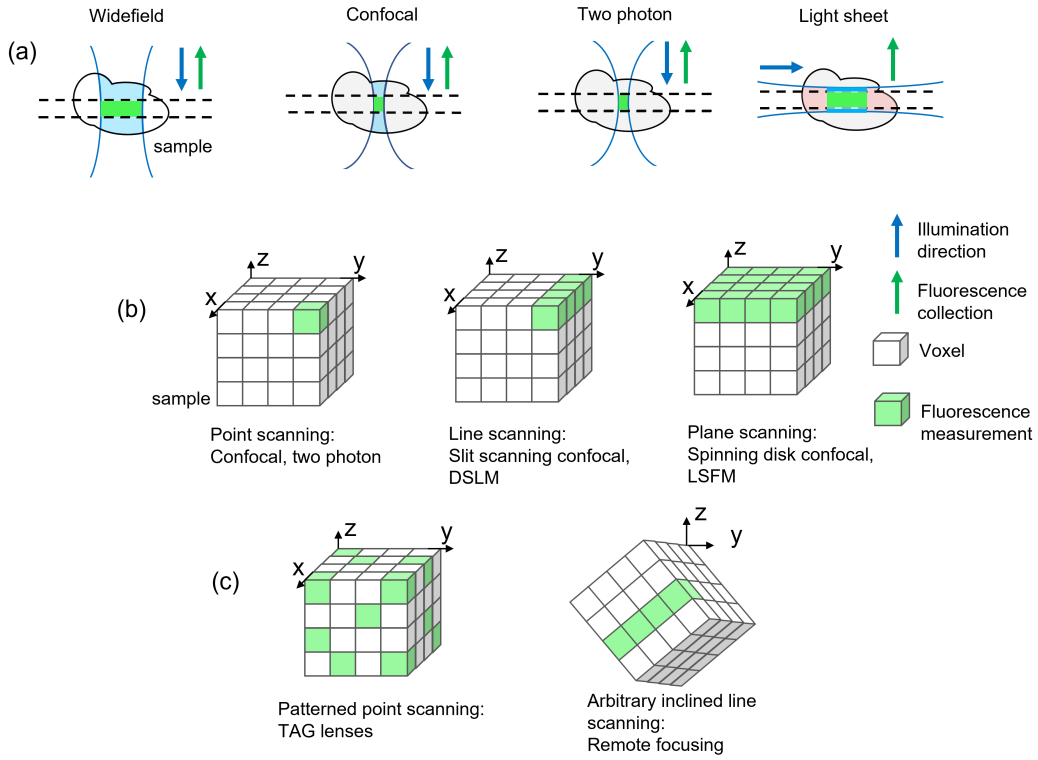

Figure 1.12: (a) Excitation profiles for the commonly used volumetric imaging techniques in fluorescence microscopy. Parts of the sample excited outside the depth of field (dashed lines) are shaded in blue. Portion of the fluorescence signal that contributes to a single measurement for each technique is indicated in green. Red indicates the area excited by the illumination beam outside the lateral FOV. (b) Degree of parallelization for various volumetric sectioning modalities. (c) Flexible illumination schemes made possible using refocusing techniques allowing for sample-adaptive imaging modality. Figure adapted from reference [34].

resolution from a conventional CLSM with the cost of a slight decrease in spatial resolution and sectioning capabilities [35]. Slit-scanning increases the speed from a few frames per second to a few hundred frames per second. When combined with RF, Botcherby et al used a slit scanning confocal microscope to image the meridional plane (x-z) without translating the sample or the imaging objective.

It should be noted here that increase in imaging speed from a CLSM requires simultaneous imaging of multiple regions of interest. For such parallelization, it is necessary to implement distributed excitation combined with 2D array detectors (CCD, sCMOS). Such configuration results in the capture of higher amount of scattered photons resulting in reduced contrast and localisation precision.

Spinning Disk Confocal Microscopy

Instead of scanning each spot sequentially, the speed of image acquisition can be increased by illuminating multiple points simultaneously. Based on the use of structured illumination, the spinning disk scans the sample with many light points formed from multiple pinholes present on the disk. As the disk sits conjugate to the imaging plane, the fluorescence emission is spatially filtered as it passes through the same pinhole. Due to the parallelisation, an excitation spot can dwell on a point for longer requiring lower excitation energy compared to CLSM. This decreased incident intensity reduces phototoxicity and photobleaching which is especially advantageous for imaging live organisms. In the case of spinning disk systems, array detectors are used to image the 2D field of view.

One disadvantage of spinning disk is the crosstalk between the multiple illumination PSFs. Due to this overlap of PSFs, the excitation intensity at defocused regions remains constant - albeit at lower levels than widefield systems. However, increasing the distance between pinholes decreases the efficiency of using the illumination light leading to the requirement of strong laser light sources.

In Chapter 4, we demonstrate a novel approach of combining sectioning capabilities of a differential spinning disk system and refocusing using remote focusing.

The off-the-shelf Aurox Clarity unit uses a quartz spinning disk imprinted with a reflective binary grating pattern. The use of grid pattern rather than pinholes allows for the use of LED illumination rather than expensive lasers. The confocal imaging principle for this spinning disk architecture is explained in detail in reference [36]. Due to the implementation of agitation-free refocusing, we were able to image normal spontaneous neural activity of *Platynereis dumerilii* larvae at multiple axial planes within the sample.

Multiphoton Microscopy

Two-Photon Excitation Microscopy (2PEM) is another method to optically section thick samples [37]. Two-photon absorption process was first described by Maria Göppert Mayer in 1931 [38]. Under normal conditions, fluorescence involves the absorption of a single photon to excite the molecule and subsequently release a photon of lesser energy as fluorescence. The same fluorescence can be obtained by exciting the molecule by simultaneous absorption of two less energetic photons (typically in infrared) under intense laser illumination. This nonlinear absorption process occurs if the sum of the energies of the two photons is greater than the energy gap between the molecule's ground and excited states. Since this process depends on the simultaneous absorption of two photons, the probability of two-photon absorption by a fluorescent molecule is a quadratic function of the excitation radiance. Due to this quadratic dependence, fluorescent signal is confined to the focal volume where the photon density is high enough for simultaneous two photon absorption (Figure 1.12). Light sources used for 2PEM are pulsed lasers with high repetition rates (100 MHz) and pulse widths in the range of femtoseconds to picoseconds to provide high peak power to induce two-photon absorption.

In confocal imaging, scanning a single plane excites the entire 3D FOV causing photodamage. Additionally, fluorescence signal originating from the focal volume and scattered on the way out is rejected by the pinhole. This becomes increasingly wasteful when imaging deeper into the biological sample. In 2PEM, as the fluo-

rescence is known to originate only from the focal volume, the detection scheme captures both the ballistic and scattered fluorescence in a widefield detection mode preserving high SNR for deep tissue imaging.

The high spatial selectivity of 2PEM provides an invaluable tool for biologists to probe deep within the tissue without photobleaching the fluorophores in the areas above and below the focal volume. The use of infrared wavelengths allows for less scattering within the specimen media, enabling two-photon microscopes to image six-fold deeper (about 1 mm deep) compared to single photon techniques. Under sufficiently intense excitation, three-photon and higher photon excitation is also possible allowing for even deeper imaging into biological samples [39, 40]. Similar to confocal modality, one of the major drawbacks of multiphoton microscopy is the point scanning acquisition which limits the speed of volumetric imaging of large specimens.

Two-photon and three-photon microscopy has been combined with remote focusing to perform in vivo Ca^{2+} imaging of the mouse cortex [41]. This spanned a volume of 1 mm x 1 mm x 1.22 mm imaged at 17 Hz. As this system was implemented at low resolution (xy = 5 µm, z = 15 µm), depth dependant spherical aberration was cancelled using a low-NA tube lens.

Due to reduced scattering, multiphoton microscopes are usually used to image large sample volumes. Traditionally, successive 2D planes are captured to form a 3D volume which amounts to large data size with many voxels irrelevant to the biological question of interest. When combined with remote focusing, the imaging geometry can be matched with the structure of interest within the sample reducing the amount of data acquired from the entire volume. This improves the spatial and temporal bandwidth of the system and reduces the post-processing burden. This technique has been implemented to scan oblique region-of-interest (ROI) providing a smarter scanning methodology [42]. It has been combined along with 2PEM to image orthogonal planes or non-contiguous areas within the sample [43, 44].

Light-Sheet Microscopy

It is seen from the above techniques that improvement in either contrast, temporal resolution or penetration depth often leads to the degradation of performance in the other two. In modern biology accurate information in 4D (x-y-z-t) domain plays an important role in investigating complex dynamic molecular processes in thick specimens. Light Sheet Fluorescence Microscopy (LSFM) allows for imaging into thicker samples with reduced photobleaching, high resolution and faster imaging [45]. This makes LSFM especially suited for gentle, long term in vivo imaging allowing for visualisation of normal cellular activity across the organism.

One of the main differences of LSFM from other fluorescence microscopy techniques is the de-coupled and orthogonal illumination to detection geometry [46]. Confocal microscopy follows an epi-illumination path where a single lens overlaps the illumination and detection PSFs. The resultant PSF is the volume common to these two geometries. To improve on the axial resolution obtained by confocal systems, Lindek et al employed an oblique illumination confocal microscope also called as a confocal theta microscope [47, 48]. Rotating the detection path by 90 degrees showed the least overlap between the illumination and detection volumes improving the axial resolution.

LSFM improved on the temporal resolution of confocal theta microscope by configuring it to perform widefield detection. LSFM uses thin planar sheets of light to optically section thick tissues by restricting illumination to the focal plane of the detection objective. Depending on the thickness of the light sheet, fluorescent molecules are only excited within the depth of field greatly reducing photobleaching/photodamage. LSFM was first utilised by Voie et al to image cochlea features to improve cochlea implants [49]. It was applied by Huisken et al in 2005 in the field of developmental biology to image in vivo embryogenesis of *Drosophila melanogaster* [50]. After this followed an explosion in the development and use of this technology.

Depending on the imaging requirements, the architecture of a standard LSFM

has been varied leading to a multitude of configurations. One variation of LSFM is the Digitally scanned laser light-sheet microscopy (DSLM) where a line shaped laser beam is used to scan across the specimen. Here, a laser scanner is used to rapidly move the beam across the lateral FOV. This allows for the use of self-reconstructing Airy or Bessel beams which improve penetration in thick tissue [51]. LSFM can also be combined with two-photon excitation improving deep tissue imaging in scattering samples [52].

Oblique Plane Microscopy

A variation of DSLM relevant to this thesis is Oblique Plane Microscopy (OPM). In LSFM, the orthogonal orientation of the illumination and detection objective requires custom sample mounting procedures. Additionally, in high-NA systems, the plane of illumination and detection should coincide within a precision of a micron to not introduce defocus in the system. In 2008, Chris Dunsby developed OPM which uses a single objective for both illumination and detection [53]. As seen in Figure 1.13, the excitation beam is incident at the edge of the BFP of the objective, resulting in an inclined light sheet in object space. By tilting the beam at the back aperture, the inclined light sheet is laterally shifted across the sample. The fluorescence from this inclined plane is collected by the same objective. This removes the need for specialised sample mounting, and due to the epi-illumination geometry, it can be implemented on standard inverted or upright microscopes.

In 2015, Hillman's group developed the Swept confocally-aligned planar excitation (SCAPE) microscope [54]. Rather than scanning the sample using a piezo-driven objective, a hexagonal mirror was used to scan the light-sheet across the sample and de-scan the fluorescence. This improved the temporal resolution of subsequent OPM systems.

OPM uses remote focusing to bring the oblique plane into focus. This requires the final re-imaging objective to be in off-axis orientation leading to a reduction in the effective NA of the microscope. This issue was addressed by Yang et al by

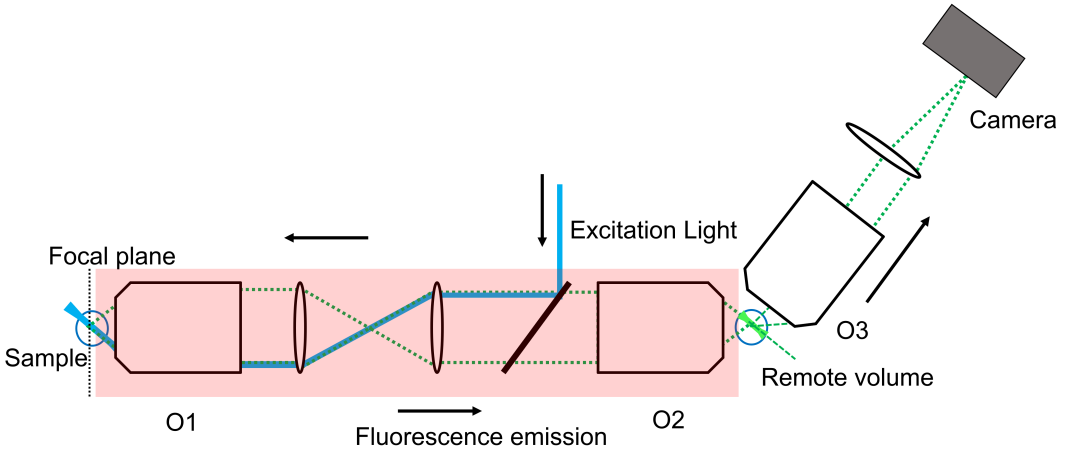

Figure 1.13: OPM system where the excitation light is incident at the edge of the BFP of the objective resulting in an oblique light sheet. The fluorescence from this oblique plane is brought into focus of the third re-imaging objective, O3, using the RF system (highlighted in pink). O3 is aligned at the same angle as the light sheet. Due to the off-axis orientation of O3, the cone of light forming the image at the remote volume is shifted outside the collection cone of O3, reducing the effective NA of the system.

using a final immersion objective to preserve the native NA of the system [55]. As this leads to stringent alignment and mechanical constraints, a custom glass tipped objective was developed [56]. This current version of OPM has been implemented for high spatio-temporal resolution and agitation-free imaging to study a wide range of biological phenomena [57].

Remote focusing has gained renewed interest in recent years due to its implementation in OPM. OPM takes advantage of the fact that RF provides an instantaneous diffraction-limited remote volume. This allows for imaging oblique planes of interest without the need for additional aberration correction. This same feature of RF systems translates into increased flexibility in choosing imaging planes that match with the geometry of the sample features [42, 58].

1.5.1 Limitations of RF systems

The choice of the focal length of the tube lenses in the RF system is not trivial as the effective magnification should be $\frac{n}{n'}$ for diffraction-limited imaging. For example, in

the high-NA RF system built by Lawton et al, the magnification of the RF system is 1.6x compared to the required magnification of 1.5x [59]. In the SCAPE system described in the previous section, the RF unit has a magnification of 1x compared to the required 1.33x. However, the effect of the resulting reduction in diffraction-limited imaging has not been studied.

So far, to my knowledge, remote focusing systems have only been built in labs with in-house optics expertise. This could be due to the increased sensitivity to the alignment of multiple high-NA objectives and the constraints in the choice of optics that can be used. This has proven to be a bottleneck for its adoption as a routine volumetric refocusing module.

The work presented in this thesis goes some way in addressing these two limitations. We provide a computational model that allows the user to predict the performance of the system if the effective magnification of the RF system is not $\frac{n}{n'}$. Furthermore, combining RF systems with an inverted microscope reduces system complexity and at the same time allowing for standard sample mounting protocols.

It should be noted here that when using RF systems, the primary objective is being used outside of its optimum design conditions. This issue becomes more relevant in OPM systems where the RF unit is used to enable the imaging of planes that are inclined with respect to the native focal plane. This calls for further understanding of the imaging properties at defocused and off-axis positions of the primary objective. With respect to this, the studies presented in this thesis furthers our understanding of the improvements required to enable advances from the current remote focusing techniques.

1.6 Research Contributions

The original research contributions in this thesis are listed here:

- Magnification sensitivity: This project studies the precision of phase match-

ing required for attaining the best performance from an RF system. This was accomplished by building a computational model that reflects non-ideal RF conditions. This is further verified experimentally using two high-NA RF systems built with non-ideal magnifications. The motivation here was to advance our understanding of the image formation in high-NA RF systems. I was responsible for project conception, design and implementation. Publication resulting from this project can be found in reference [60].

- Characterisation of RF system: For easier implementation, we coupled the RF system along with a standard inverted microscope. I have provided a detailed alignment protocol and thorough characterisation of telecentricity and resolution.

  This protocol has been applied in designing a Spinning Disk Remote Focusing (SDRF) microscope. This novel microscope has been applied to study neural activity of *Platynereis dumerilii* larvae. Publication resulting from this collaborative project can be found in reference [61].

- Residual aberration compensation: In this project, I present a method for reducing residual spherical aberration in the RF system. The compensation is performed using the correction collar on the imaging objective. I have developed automated correction collar rotation hardware and control algorithm and experimental quantification of spherical aberration in RF systems.

  To understand the nature of residual aberrations across the FOV, I have performed empirical assessment of off-axis aberrations in RF systems. This has been additionally verified using simulations and assessing imaging metrics at off-axis positions. I was responsible for project conception, design and implementation.

1.7 Thesis Overview

In this introduction chapter, I have explored the image forming properties of an optical microscope and key concepts regarding aberrations, resolution, and telecentricity that will be used in the rest of this thesis. I have reviewed various methods for high contrast volumetric imaging and the advantage of each sectioning technique. Additionally, I have provided a brief overview of agitation-free refocusing techniques and discussed the advantages of the RF methodology.

In Chapter 2, the working principle of an RF system is formally introduced. I look at the conditions that needs to be met to obtain a diffraction-limited 3D volume. A computational model is developed to predict the tolerance of the remote focusing system to non-ideal imaging conditions. The predictions are confirmed using an experimental high-NA RF system with non-ideal magnifications.

In Chapter 3, informed by the computational model, the loss in resolution of the RF system by applying a small deviation from ideal magnification condition is studied. The degradation in system performance using PSF measurements is calculated. The alignment protocol for RF systems with a standard inverted microscope is presented.

In Chapter 4, the characterisation procedure explained in Chapter 3 is applied to a novel spinning disk remote focusing microscope. The microscope is used to perform live volumetric imaging of *Platynereis dumerilii* larvae.

In Chapter 5, I investigate a possible method of correcting for residual spherical aberration in the RF system using the correction collar on a water immersion objective. I also discuss the effect of off-axis aberrations towards the image quality at defocused positions.

In Appendix A, the commonly used acronyms used in this thesis are listed.

In Appendix B, the links to the online repository containing the codes and datasets presented in this thesis is provided.

CHAPTER 2

TOLERANCE ANALYSIS OF REMOTE FOCUSING SYSTEMS

This chapter has been adapted from the research article *'Sensitivity of remote focusing microscopes to magnification mismatch'* [60].

In the introduction we discussed the application of remote focusing in various volumetric imaging modalities. In addition, we briefly considered the limitations when implementing RF methodology. When compared to the various refocusing strategies discussed in section 1.4, RF is unique in its ability to correct for both defocus and depth-dependant spherical aberration. However, it has been observed that when using high-NA objectives, RF provides only half of the theoretically determined diffraction-limited axial range [32, 62]. An explanation for this discrepancy could be the assumption made by Botcherby regarding the ideality of the objective lenses in his analytical formalism of the RF system [32]. In addition to this, it should be noted that the potential of using RF systems comes along with its increased sensitivity to alignment. Perfect phase matching between two high-NA objectives is required to cancel out the tremendous amounts of depth-dependant spherical aberration that is generated when imaging outside the focal plane. The motivation here is to understand the sensitivity of RF systems to non-ideal phase matching conditions. In systems built with non-ideal magnification leading to incomplete aberration compensation, we provide a method to predict the attainable diffraction-limited range.

In this chapter, I start by introducing the working principle of an RF microscope and the method in which it corrects for depth-dependant spherical aberration. This is followed by the description of the computational model that has been developed for predicting the diffraction-limited range for non-ideal configurations. We experimentally verify these predictions and finally discuss their implications when building high-NA RF microscopes.

2.1 Remote Focusing Principle

In section 1.5, we looked at the application of remote focusing systems in volumetric imaging and I briefly mentioned the method in which an RF unit implements depth-dependant spherical aberration correction. In this section, I review the theoretical framework explaining the introduction of depth dependant spherical aberration and the method by which the RF system compensates for it.

For a lens, the defocus function describes the phase of the wavefront when a point source on the optical axis is shifted away from the focal plane. For a low NA lens, the phase term, ψ, can be written as a quadratic function:

$$\psi = nkz\left(1 - \frac{\rho^2 \sin^2 \alpha}{2}\right). \tag{2.1}$$

Here n is the refractive index of the immersion medium of the lens, k is the wavenumber equal to $2\pi/\lambda$ where λ is the wavelength of light and z is the axial shift from the focal plane of the lens. The normalised pupil radius, ρ, is defined as $\frac{\sin\theta}{\sin\alpha}$ where θ is the angle of the ray leaving the sample and α is the maximum acceptance angle of the lens. This defocus term can be easily compensated by shifting the detector until the image of the point source is in focus. However, for high-NA lenses, defocus is described by a spherical function [63]:

$$\psi = nkz\sqrt{1 - \rho^2 \sin^2 \alpha}. \tag{2.2}$$

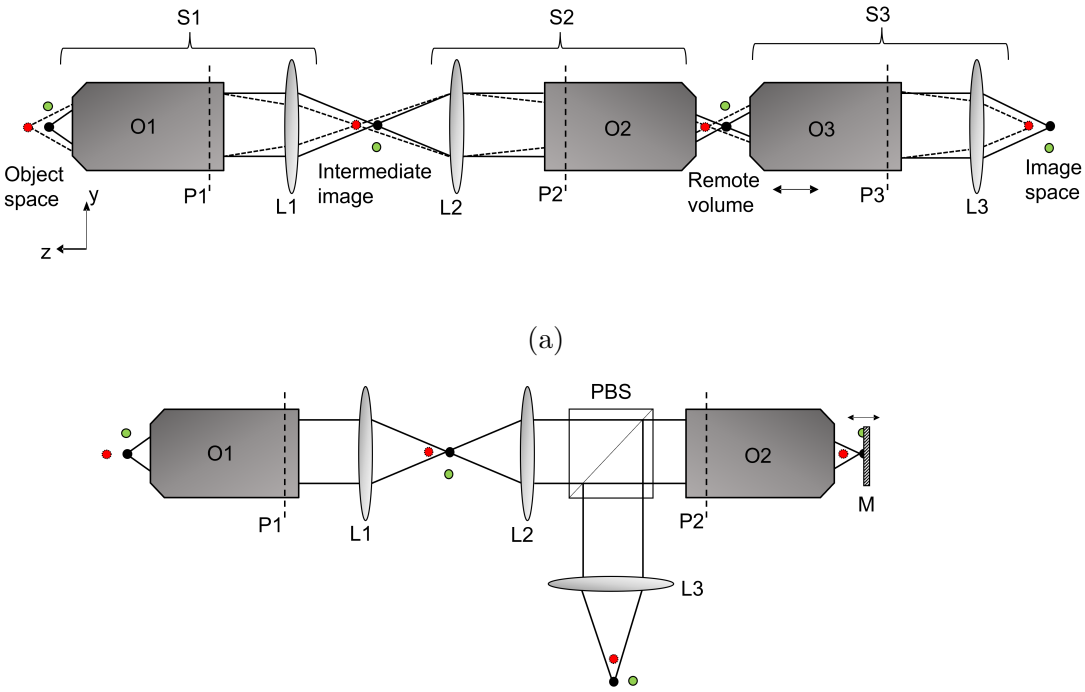

Figure 2.1: An RF system in the (a) 'unfolded' geometry with three microscopes S1, S2 and S3 in series. Microscope S1 forms an intermediate image with magnification M_{S1}. The remote volume has a uniform magnification of $M_{S1}M_{S2} = \frac{n_1}{n_2}$, with M_{S2} being a demagnification of the intermediate image. The final image formed by S3 on the detector has a magnification of $M_{S1}M_{S2}M_{S3}$. O3 is translated axially to image different depths of the remote volume. The vertical dashed lines on the objectives signify the position of the exit pupil plane (P) for each objective. (b) The 'folded' geometry where O2 is reused as the reimaging objective. A mirror (M) at the focal plane of O2 is scanned in z to refocus the system at different depths. PBS - Polarising Beam Splitter.

Equation 2.1 approximates equation 2.2 for small $\sin\alpha$. The term in the square root can be expanded to give higher orders of ρ which is observed as depth dependant spherical aberration for high-NA lenses. Point sources outside of the focal plane (away from the objective) generate positive spherical aberration, with points inside focus generating negative spherical aberration. Any remote system used for refocusing high-NA objectives needs to produce equal and opposite amounts of the phase term described by equation 2.2 to compensate for the spherical aberration. An RF system does this exactly by introducing a matching high-NA lens in the optical path.

Figure 2.1a shows the optical layout of an RF system in the unfolded geometry. It consists of three infinity-corrected microscopes (S1, S2 and S3) in series. S1 consists of the imaging objective, O1, which is closest to the sample being imaged and remains stationary. S2 is placed back to back with S1 so that it demagnifies the intermediate image to form an aberration free remote volume around the focal plane of the refocusing objective O2. The first two tube lenses, L1 and L2, form the relay optics (4f-system) and map the pupil planes of O1 and O2. A third microscope, S3, containing the reimaging objective O3 relays individual planes from the remote volume to the detector.

This arrangement can also be configured in the folded geometry where O2 is reused as the reimaging objective by axially translating a mirror at its focal plane (Figure 2.1b). As mirrors have lower inertia than objectives, this configuration allows for fast scan rates. However, in the folded geometry, half of the fluorescence signal is lost due to the presence of a polarising beamsplitter (placed immediately before O2). In this chapter, subscripts 1, 2 and 3 denote parameters relating to the three microscopes shown in Figure 2.1.

As discussed in section 1.2.3, the formation of the aberration free remote volume can be understood by looking at two design conditions that are used to characterise lenses. The sine condition ensures that all points on a plane perpendicular to the optical axis are imaged stigmatically [64]. Microscope objectives are designed using the sine condition which allows distortion-free imaging of laterally shifted points on the focal plane. Complimentary to the sine condition, the Herschel condition allows for stigmatic imaging of points lying on the optical axis but displaced axially. As we require the formation of a volume that has no distortion laterally or axially, the RF system needs to simultaneously follow both the sine and Herschel condition. To do this, the magnification of the system should be equal to the ratio of the refractive indices of the immersion media in the object and image space (n_1 and n_2 , respectively)[65]. As objectives are designed to provide very high magnifications, the image formed by S1 is demagnified by S2 to form the remote volume having

uniform magnification of

$$M_{RF}^{Id} = M_{S1}M_{S2} = \frac{n_1}{n_2}. \tag{2.3}$$

Where the magnification of the microscopes S1 and S2 are defined as

$$M_{S1} = \frac{M_1 f_{L1}}{f_{L1,nom}}, \tag{2.4}$$

$$M_{S2} = \left[\frac{M_2 f_{L2}}{f_{L2,nom}}\right]^{-1}. \tag{2.5}$$

Here $f_{L1,nom}$ and $f_{L2,nom}$ are the nominal focal lengths of the tube lenses required to provide the design magnifications M_1 and M_2 for objectives O1 and O2 respectively. These nominal values are specified by the manufacturer as for example f=180 mm for Olympus objectives. f_{L1} and f_{L2} are the focal lengths of the lenses used in the relay system.

For the remote volume to have a magnification defined by Equation 2.3, it requires the magnification of the relay lenses to be

$$M_{RF}^{Id} = \frac{f_{L2}}{f_{L1}} = \frac{n_2 M_1}{n_1 M_2} \tag{2.6}$$

For the simplest case of having identical objectives for O1 and O2 and the same immersion media for both, M_{4f}^{Id} will be equal to 1. However, for biological applications, O1 is chosen such that the refractive index of the immersion media matches with that of the sample. O2 is preferred to be an air spaced objective so that inertial artefacts during refocusing can be avoided. This leads to reduced flexibility in the choice of lenses for the relay system. To get the maximum axial extent of aberration free imaging (diffraction-limited range) requires the relay lenses to closely follow Equation 2.6, which will lead to the RF system having the ideal magnification defined by Equation 2.3. Deviation leads to breaking the Herschel condition which again results in the introduction of spherical aberration terms and reduction in the

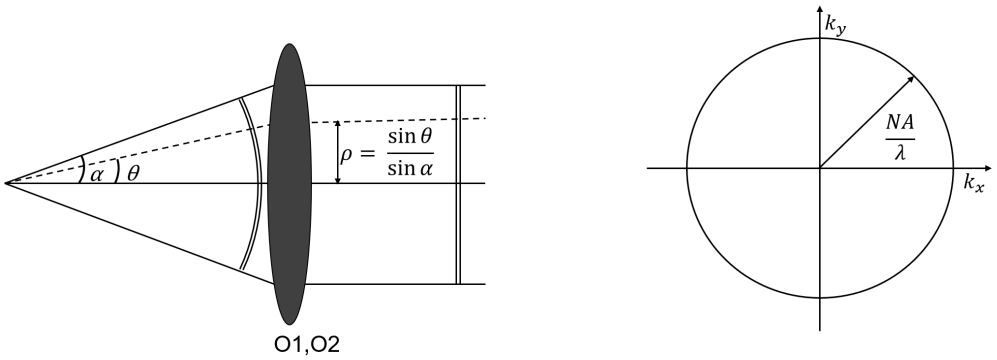

(a) (b)

Figure 2.2: (a) Schematic describing the relation between ray angles and normalised pupil radius. (b) Schematic showing the radial extent of the pupil in frequency space.

diffraction-limited range.

In the following sections we determine the sensitivity of the diffraction-limited range to the choice of lenses, L1 and L2. We first build a computational model that can predict the amount of spherical aberration present at each depth for different amounts of magnification mismatch. We then validate this model against experimental measurements of pupil plane aberrations in a folded remote focusing system using a Shack-Hartmann wavefront sensor. Finally, we use the simulation to quantify the sensitivity of the diffraction-limited range to the magnification mismatch.

2.2 Methods

2.2.1 Remote Focusing Model

As magnification mismatch introduces aberrations into the RF system at defocussed positions, this can be represented as phase variations in the wavefront at the pupil plane. Following the RF theoretical model built by Botcherby in reference [32], we consider a point source on the optical axis shifted by a distance 'z' from the focal plane, which in turn is located a distance 'f' from the principal surface. In the condition that $z \ll f$, the generalised phase at the pupil planes P1 and P2 are given by

$$\psi_1 = n_1 k \left[f_1 \left(1 - \frac{2}{f_1} \left(1 - \rho_1^2 \sin^2 \alpha_1 \right)^{\frac{1}{2}} + \frac{z_1^2}{f_1^2} \right)^{\frac{1}{2}} - f_1 \right], \tag{2.7}$$

$$\psi_2 = n_2 k \left[f_2 \left(1 + \frac{2}{f_2} \left(1 - \rho_2^2 \sin^2 \alpha_2 \right)^{\frac{1}{2}} + \frac{z_2^2}{f_2^2} \right)^{\frac{1}{2}} - f_2 \right]. \tag{2.8}$$

Here $f_{1,2}$ is the front focal length of the objectives (O1 and O2) and can be calculated by dividing the nominal focal length of the tube lens by the design magnification of the objective. The parameters z_1 and z_2 are the distances of the point source and its image from the focal planes of O1 and O2 respectively. The normalised pupil radius, ρ, ranges from 0 to 1 from the centre to the edge of the pupil (Figure 2.2a).

The phase of the wavefront forming the remote volume, $\Delta\psi_{RF}$, is calculated by taking the sum of the phase terms defined by Equations 2.7 and 2.8 which we approximate and rewrite as:

$$\psi_1 = n_1 k \left[1 - z_1 \left(1 - \rho_1^2 \sin^2 \alpha_1 \right)^{\frac{1}{2}} + \frac{z_1^2 \left(1 - \rho_1^2 \sin^2 \alpha_1 \right)}{2 f_1} \right], \tag{2.9}$$

$$\psi_2 = n_2 k \left[1 + z_2 \left(1 - \rho_2^2 \sin^2 \alpha_2 \right)^{\frac{1}{2}} + \frac{z_2^2 \left(1 - \rho_2^2 \sin^2 \alpha_2 \right)}{2 f_2} \right], \tag{2.10}$$

$$\Delta\psi_{RF} = \psi_1 + \psi_2. \tag{2.11}$$

We introduce a factor, β, which is the ratio of the actual relay lens magnification to the ideal magnification.

$$\beta = \frac{M_{4f}}{M_{4f}^{Id}}. \tag{2.12}$$

When $\beta = 1$, the mapping is ideal and both Herschel and sine conditions are satisfied (Equation 2.3). The magnification of the relay lenses ensure that the angular ray span in object space is equal to ray span in image space. This results

in the spatial frequencies being accurately mapped leading to $\rho_1 \sin\alpha_1 = \rho_2 \sin\alpha_2$, for all rays, cancelling the linear z terms in Equations 2.9 and 2.10. Therefore, the wavefront formed by a point object at axial displacement z_1 is stigmatically imaged by O2 at $-\frac{n_1}{n_2} z_2$.

As z_1 increases, the z^2 terms relating to higher order spherical aberration add up to contribute to $\Delta\psi_{RF}$, limiting the theoretical diffraction-limited range of an ideal RF system. In a nonideal system, where M_{4f} is not equal to M_{4f}^{Id}, noncancellation of the linear z terms results in increased amounts of spherical aberration even for small shifts in z_1. $\beta < 1$ and $\beta > 1$ signifies overmagnification and undermagnification by the relay lenses respectively.

2.2.2 Computational Model

We characterise the sensitivity of the RF system to magnification mismatch by quantifying the amount of spherical aberration generated by a point source translated by a distance z from the focal plane of O1. This can be done by using Equations 2.9 and 2.10 to calculate the phase at the pupil plane of O1 and O2 for different β and deriving the resulting $\Delta\psi_{RF}$. The pupil plane is described using spatial frequency coordinates k_x and k_y (Figure 2.2b). This pupil plane is subdivided into 2N $\times$ 2N regions, such that the smallest increment in k_x or k_y is defined by:

$$\gamma_x = \gamma_y = \frac{\mathrm{NA}}{\lambda N}. \tag{2.13}$$

Here N is chosen such that the pupil plane sampling does not introduce any aliasing effects (1280 $\times$ 1280 pixels used in current simulation). The $\boldsymbol{k}$ vector within the pupil plane is therefore:

$$\boldsymbol{k} = \begin{pmatrix} k_x \\ k_y \end{pmatrix} = \begin{pmatrix} m\gamma_x \\ n\gamma_y \end{pmatrix}. \tag{2.14}$$

For each location in the pupil plane (m, n), we calculate the $\sin\theta_1$ value of the

corresponding ray to be

$$\sin\theta_1(m,n) = \frac{\lambda\gamma\sqrt{k_x^2 + k_y^2}}{n_1}. \tag{2.15}$$

From the $\sin\theta_1(m,n)$ values we can then calculate $\rho_1(m,n)$ and $\cos_1(m,n)$ as

$$\rho_1(m,n) = \frac{\sin\theta_1(m,n)}{\sin\alpha_1}, \tag{2.16}$$

$$\cos\theta_1(m,n) = \sqrt{1 - \rho_1^2\sin^2\alpha_1}. \tag{2.17}$$

where $\sin\alpha_1 = \frac{NA_1}{n_1}$. To map between the two pupil planes, we use the relation

$$\sin\theta_2(m,n) = \beta\sin\theta_1(m,n). \tag{2.18}$$

If $\beta = 1$, $\sin\theta_2(m,n) = \sin\theta_1(m,n)$. For $\beta \neq 1$, the mismatch in frequency space is reflected in the final phase of the wavefront, $\Delta\psi_{RF}$, introducing aberrations in the remote volume.

To impose the finite extent of allowed spatial frequencies we define a circular mask in the pupil plane (Figure 2.2b) as

$$\text{PupilMask} = \begin{cases} 1 & \sqrt{k_x^2 + k_y^2} \leq \frac{n_1\sin\theta_{max}}{\lambda} \\ 0 & \text{otherwise} \end{cases} \tag{2.19}$$

$\sin\theta_{max}$ is the limiting aperture of the RF system. For the spatial resolution of an RF system to be defined by the NA of O1, $\sin\alpha_2$ should be greater than or equal to $\sin\alpha_1$. This ensures that O2 does not act as an aperture stop in the RF system. This important RF design condition is considered to be true in the simulation and the pupil mask for a $\beta = 1$ system is defined as $\sin\theta_{max} = \sin\alpha_1$. For nonideal conditions, the pupil mask is calculated for the objective limiting the ray angles by looking at both the forwards and backwards geometry of the RF system.

For $\beta < 1$, O2 acts as an aperture stop to give $\sin\theta_{max} = \beta\sin\alpha_1$. For $\beta > 1$, O1

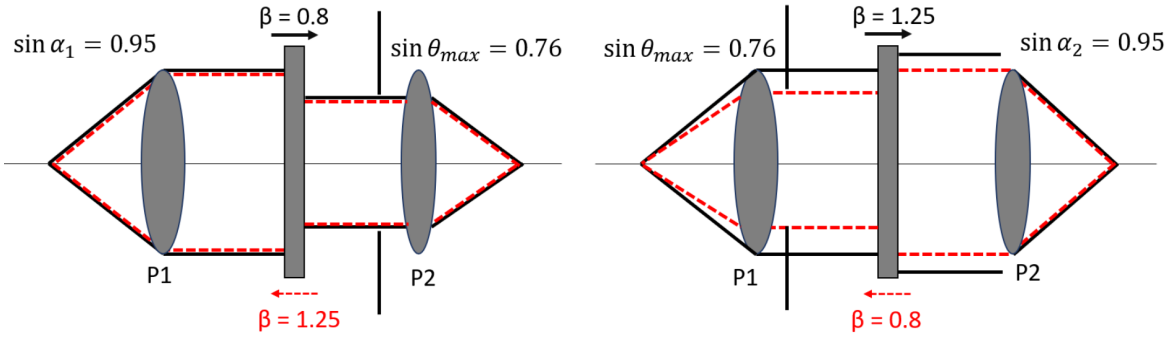

(a) (b)

Figure 2.3: Shows the selection of the limiting aperture for two identical objectives ($\sin\alpha_1 = \sin\alpha_2 = 0.95$) with nonideal relay lens magnifications (a) $\beta = 0.8$ and (b) $\beta = 1.25$. P1 and P2 indicate the pupil planes of the objectives. The solid black and red dashed lines show the forward and backward ray traces, respectively.

acts as the aperture stop to give $\sin\theta_{max} = \beta \sin\alpha_1$ (Figure 2.3). The pupil mask (Equation 2.19) multiplied by the total phase term (Equation 2.11) gives the final form of the wavefront forming the remote volume in the RF system.

2.2.3 Zernike Terms

In order to obtain the contribution of spherical aberration terms at defocused positions, z, we decompose the pupil phase into radially symmetric set of Zernike polynomials [66]. Spherical aberration introduces defocus into the imaging system shifting the refocused image from the paraxial focus by δz. This displacement aberration can be optically compensated and is therefore subtracted from $\Delta\psi_{RF}$. The defocus function ψ_d and the defocus coefficient δz are taken in the same form as Equations 2.20 and 2.21 in [32] to give the final form of the wavefront

$$\psi'_{RF} = \Delta\psi_{RF} - \delta z \psi_d. \tag{2.20}$$

ψ'_{RF} can then be expanded as a series of Zernike polynomials Z_p^q as

$$\psi'_{RF} = nk \sum_{p=0}^{\infty} \sum_{q=-p}^{n} C_p^q Z_p^q. \tag{2.21}$$

Here p is the axial order and q is the azimuthal order of the expansion terms. The polynomials, Z_p^q, are orthogonal to each other over a unit circle and C_p^q are the expansion coefficients which quantify the contribution of each aberration mode to the total phase. As the simulation models a point source shifted along the optical axis, the azimuthal terms can be ignored. This leaves the terms relating to Z_p^0 which are the rotationally symmetric aberrations. ψ'_{RF} was expanded to the first 25 terms and the fitting was performed using the MATLAB zernike_coeffs function [67]. In the expansion basis set, the polynomial associated with first order spherical aberration is

$$Z_4^0(\rho) = \sqrt{5}\left(6\rho^4 - 6\rho^2 + 1\right). \tag{2.22}$$

The corresponding first order spherical aberration coefficient, C_4^0 , was extracted for a range of z and compared with the experimentally derived values.

2.2.4 Strehl Ratio

We characterised the tolerance of the RF system to magnification mismatch by measuring the change in the diffraction-limited range for different β. To do this, we measured the Strehl ratio across z for different β values. For an RF system, the Strehl ratio (S) is defined as the ratio of the maximum intensity of the image of the point source at z to that at $z = 0$ (focal plane). An approximate expression for the Strehl ratio can be written as [68]

$$S = e^{-\left\langle \left(\psi'_{RF} - \overline{\psi'_{RF}}\right)^2 \right\rangle}. \tag{2.23}$$

An unaberrated wavefront has a Strehl ratio of 1. Due to its dependence on the variance of the wavefront across the pupil, increased amounts of aberrations reduces the Strehl ratio. Similar to the previous section, we use ψ'_{RF} to calculate S as the presence of defocus terms increases the variance which would underestimate the maximum attainable diffraction-limited range. As explained by Mahajan in

reference [66], Strehl ratio of 0.8 and above is considered nominal for perfect imaging and therefore sets the bounds of the diffraction-limited range for a given β.

2.2.5 Experimental Verification

The computational model was verified experimentally by constructing an RF system in folded geometry (Figure 2.4). A pair of 0.95 NA 40x dry objectives (UPLSAPO40x2, Olympus) were used as the imaging and refocusing objectives O1 and O2, respectively. A collimated laser beam (532 nm, CPS532, Thorlabs) was expanded to 10 mm diameter to overfill the back aperture of O1. The focal spot formed by O1 approximated as a point source for the RF system. Mirror R1, mounted on a linear stage (PT1A/M, Thorlabs) was translated axially across the focal plane. When R1 is translated by a distance z_1, the optical path length changes by a factor of 2, changing the object position by $z = -2z_1$. The corresponding refocused image was formed by O2 at $z = -2z_2$ as $n_1 = n_2$.

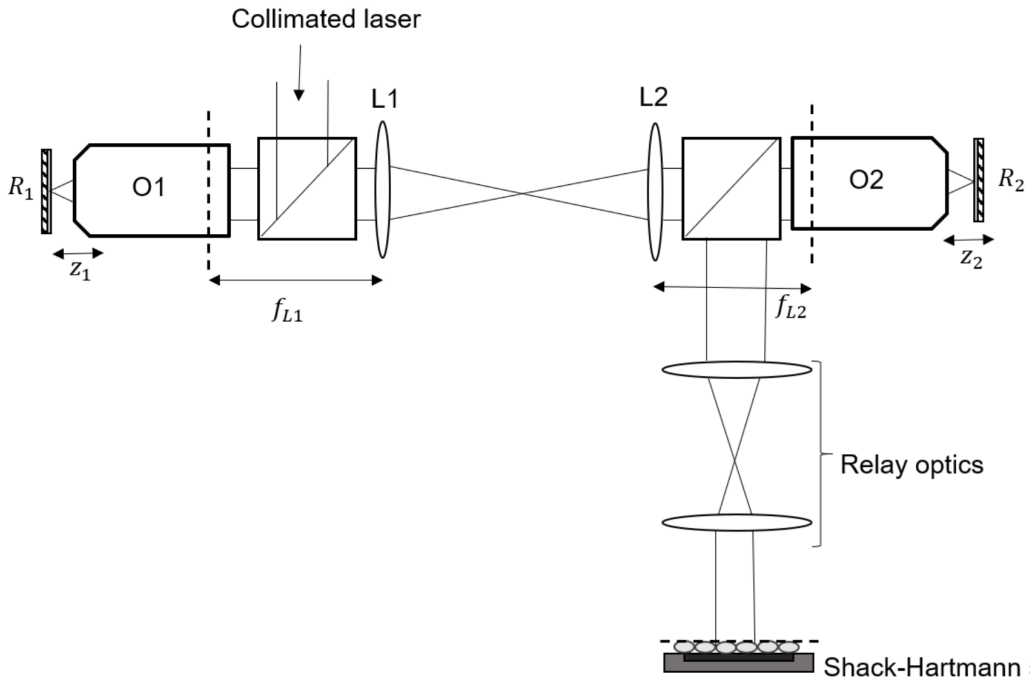

Figure 2.4: RF system aligned in folded geometry used for computational model verification

The relay lenses, L1 and L2, map the pupil planes of O1 and O2 together and

were placed in telecentric alignment. To ensure that the aberrations arising due to the misalignment of the mirrors were kept minimum, the mirrors were translated across their axial range and the reflected beam was checked to be centred across the optical layout using a pinhole.

Three achromat lens pairs were chosen for L1 and L2 to provide the following focal length combinations (f_{L1}, f_{L2}), (in mm): (125, 125), (100, 125) and (125, 100). This gave β values of 1, 0.8 and 1.25 to reflect ideal, undermagnified and overmagnified configurations.

To measure the amount of aberrations present in the final wavefront forming the remote volume, the pupil plane of O2 was made conjugate to the lenslet array of a Shack- Hartmann wavefront sensor using another pair of relay lens. For the ideal and undermagnified case, the radius of the limiting aperture over which the aberrations were measured was calculated as $\mathrm{NA}_1 f_1 \beta$ and $\mathrm{NA}_2 f_2 \beta$ for the overmagnified case.

2.2.6 Shack-Hartmann Wavefront Reconstruction

The Shack-Hartmann sensor used in thesis was built using a microlens array (Thorlabs, MLA300-14AR-M) and a CMOS camera (iDS, UI-3240LE-M-GL). When the microlens array is illuminated, discrete spots are formed as each lenslet on the microlens array focuses a part of the incoming wavefront on to the camera. The camera sensor is placed at the focal plane of the lenslets ($f = 14.6\,\mathrm{mm}$). As the sensor is imaging the exit pupil of the objective, a circular mask (Figure 2.6a) is constructed to specify the radial extent of the wavefront projected on the sensor. This is equal to the pupil diameter of the objective ($2 * \mathrm{NA} * f_{O_1}$) times the effective magnification of the relay lenses in the optical system.

Misalignment errors, such as rotation about the beam axis (θ'), between the camera and microlens array was calibrated out of the system by using a planar reference wavefront (collimated and expanded laser beam) and rotating the image until the minimum wavefront error was obtained (Figure 2.5a). This image rotation

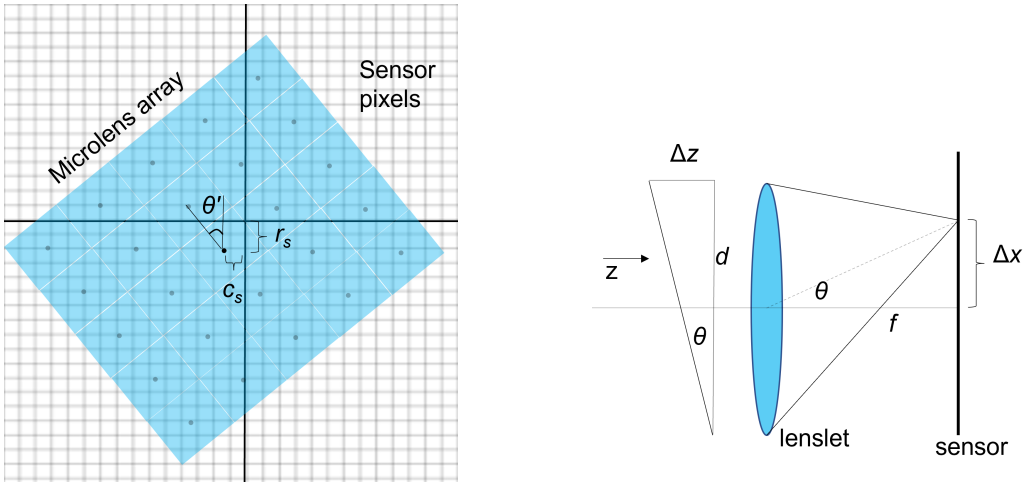

(a) (b)

Figure 2.5: (a) Rotation and lateral misalignment between the microlens array and the camera sensor. (b) Focal spot shift (Δx) on the camera sensor is related to the average wavefront slope ($\frac{\Delta z}{d}$) over the lenslet.

remains the same as long as the relative orientation between the CMOS camera and the microlens array does not change. A lateral shift (r_s, c_s) between about the centre of the microlens array and the camera was observed which results in a tilt in the final reconstructed wavefront. As this is not an actual aberration, it is removed by taking the average of all spot positions and subtracting it to the individual spot position [69].

The microlens array divides the camera sensor into N subapertures (Figure 2.6b). In the absence of aberrations the wavefront is focused at the centre of each subaperture. For an aberrated wavefront, the spot is shifted proportional to the local slope of the wavefront over each subaperture. As the slope is the gradient of the wavefront over the subaperture, measuring the spot shifts provides a method to reconstruct the original wavefront. From Figure 2.5b we see that the slope is related to the spot shift as

$$\frac{\Delta z_{(x,y)}}{d} = (S_x, S_y) = \left(\frac{\Delta x}{f}, \frac{\Delta y}{f}\right). \tag{2.24}$$

The wavefront to be reconstructed can be written as a sum of 'P' Zernike polynomials $Z_p(\rho, \theta)$. In our experiments, we set $P = 25$. The maximum number of

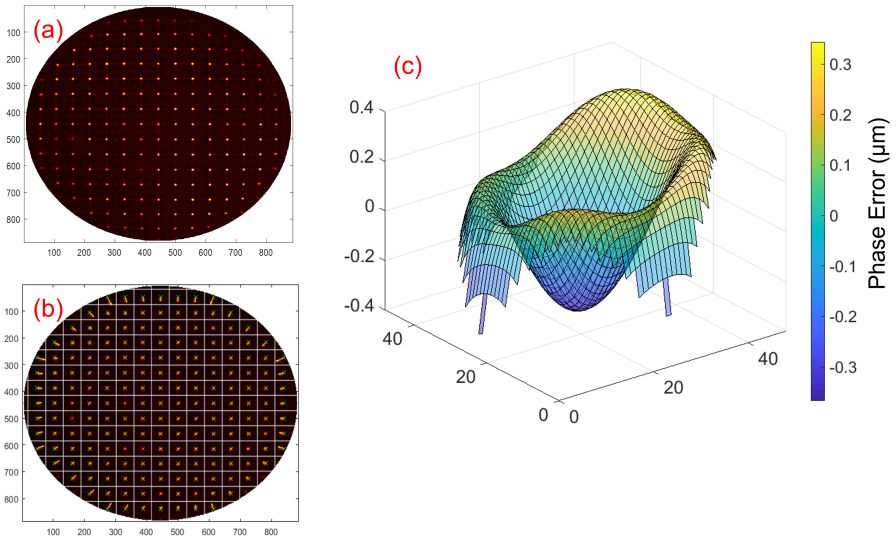

Figure 2.6: (a) The rotation corrected ($\theta^{'}$) image from the camera with a circular mask. (b) The spot array divided into sub-apertures. The centroids of the spots are measured and its shift from the centre of the sub-aperture is calculated to build the slope matrix in equation 2.27. (c) The final reconstructed wavefront using the first 25 Zernike polynomials.

Zernike modes that can be calculated is equal to the number of subapertures 'N' illuminated by the incident wavefront.

$$W(\rho,\theta) = \sum_{p=1}^{P} C_p Z_p(\rho,\theta) \tag{2.25}$$

where C_p is the coefficient of expansion. The slope (S) is related to the first derivative of the wavefront $W(\rho,\theta)$ evaluated over the n^{th} subaperture and therefore equation 2.25 can be written as

$$S_x = \frac{\partial W(\rho,\theta)}{\partial x}\Big|_n = \sum_{p=1}^{P} C_p \frac{\partial Z_p(\rho,\theta)}{\partial x}\Big|_n \qquad n = 1,2,3,...N. \tag{2.26}$$

The same can be written for the y-direction. The calculated slopes from the Shack-Hartmann sensor can be related to the Zernike polynomials as

$$\mathbf{S} = \mathbf{EC}. \tag{2.27}$$

$\mathbf{S}$ is a column matrix of size 2Nx1 containing the x slopes for each subaperture

followed by the y slopes. $\mathbf{C}$ is the column vector of size Px1 containing the unknown Zernike polynomial coefficients. $\mathbf{E}$ is the derivative of the Zernike polynomial over the subaperture of size 2NxP. The matrix is built in the form

$$\mathbf{E} = \begin{bmatrix} \frac{\partial Z_1(\rho,\theta)_1}{\partial x} & \frac{\partial Z_2(\rho,\theta)_1}{\partial x} & \dots & \frac{\partial Z_P(\rho,\theta)_1}{\partial x} \\ \frac{\partial Z_1(\rho,\theta)_1}{\partial y} & \frac{\partial Z_2(\rho,\theta)_1}{\partial y} & \dots & \frac{\partial Z_P(\rho,\theta)_1}{\partial y} \\ \vdots & \vdots & \ddots & \vdots \\ \frac{\partial Z_1(\rho,\theta)_N}{\partial x} & \frac{\partial Z_2(\rho,\theta)_N}{\partial x} & \dots & \frac{\partial Z_P(\rho,\theta)_N}{\partial x} \\ \frac{\partial Z_1(\rho,\theta)_N}{\partial y} & \frac{\partial Z_2(\rho,\theta)_N}{\partial y} & \dots & \frac{\partial Z_P(\rho,\theta)_N}{\partial y} \end{bmatrix} \tag{2.28}$$

where $\frac{\partial Z_p(\rho,\theta)_n}{\partial x}$ is the partial derivative of the p^{th} Zernike polynomial over the n^{th} subaperture in the x-direction. As $\mathbf{E}$ is a rank deficient matrix, it does not have an inverse. To obtain $\mathbf{C}$, singular value decomposition of $\mathbf{E}$ is performed to get

$$\mathbf{C} = \mathbf{V}\mathbf{\Sigma}^{-1}\mathbf{U}^{\mathbf{T}}\mathbf{S}. \tag{2.29}$$

Here $\mathbf{U}$ and $\mathbf{V}$ contain the orthogonal unit vectors and $\mathbf{\Sigma}$ is a diagonal matrix containing the singular values of $\mathbf{E}$.

The final wavefront (equation 2.25) can be reconstructed (Figure 2.6c) from the values of the Zernike expansion coefficients $\mathbf{C}$. In this thesis, we extract the contribution of the following Zernike modes (Z_p^q from equation 2.21):

$Z_2^{-2} = \sqrt{6}\rho^2 \sin 2\theta$ Y-Astigmatism

$Z_2^0 = \sqrt{3}(2\rho^2 - 1)$ Defocus

$Z_2^2 = \sqrt{6}\rho^2 \cos 2\theta$ X-Astigmatism

$Z_3^{-1} = \sqrt{8}(3\rho^3 - 2\rho) \sin\theta$ Y-Coma

$Z_3^1 = \sqrt{8}(3\rho^3 - 2\rho) \cos\theta$ X-Coma

$Z_4^0 = \sqrt{5}(6\rho^4 - 6\rho^2 + 1)$ 1^{st}-order Spherical aberration

$Z_6^0 = \sqrt{7}(20\rho^6 - 30\rho^4 + 12\rho^2 - 1)$ 2^{nd}-order Spherical aberration.

The list the first 25 Zernike polynomials as used in this thesis is listed in Appendix

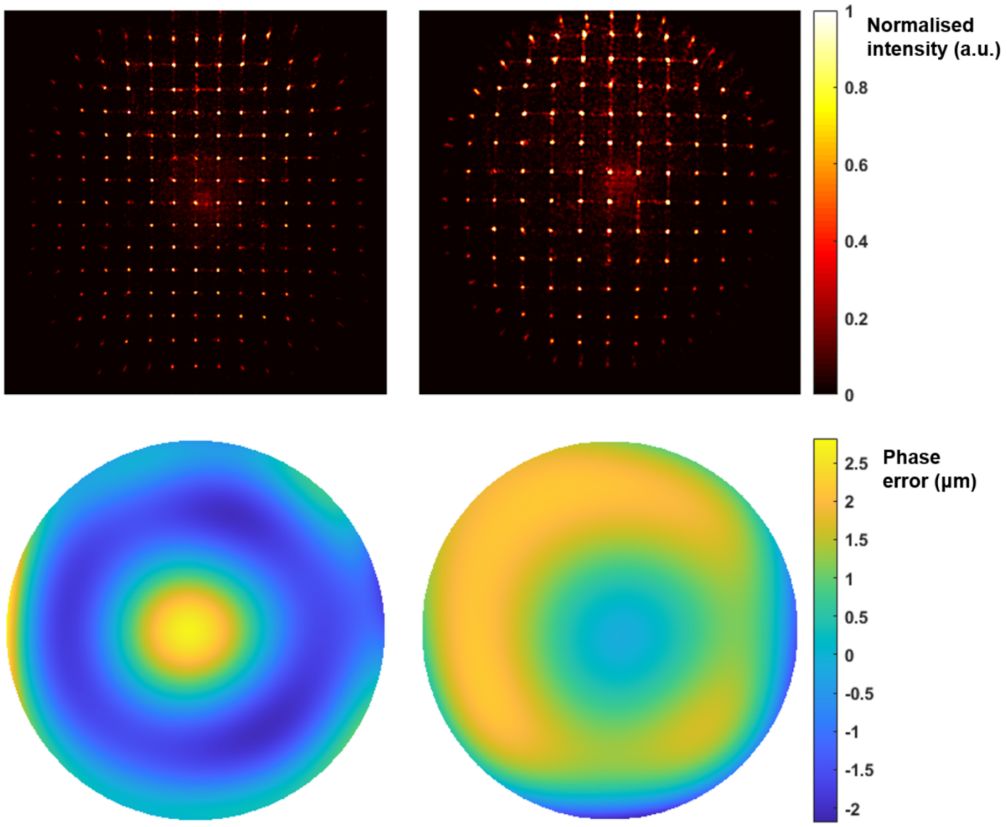

Figure 2.7: Top: Shack-Hartmann images taken for $\beta = 1.25$ (left) and $\beta = 0.8$(right) at z=50 µm. Bottom: The corresponding reconstructed wavefronts

3D of reference [70].

The maximum wavefront tilt that can be measured by the Shack-Hartmann sensor corresponded to 3 µm of Optical Path Difference across the 300 µm width of the lenslet subaperture.

For the RF system described in the previous section, for each displacement of R1, R2 was translated until the defocus term was completely cancelled ($C_2^0 = 0$). As the contribution of the second order spherical aberration was insignificant, it was not used for further analysis. The coefficient of the first order spherical aberration was extracted from the final reconstructed wavefront (Figure 2.7) to compare with the computational model results.

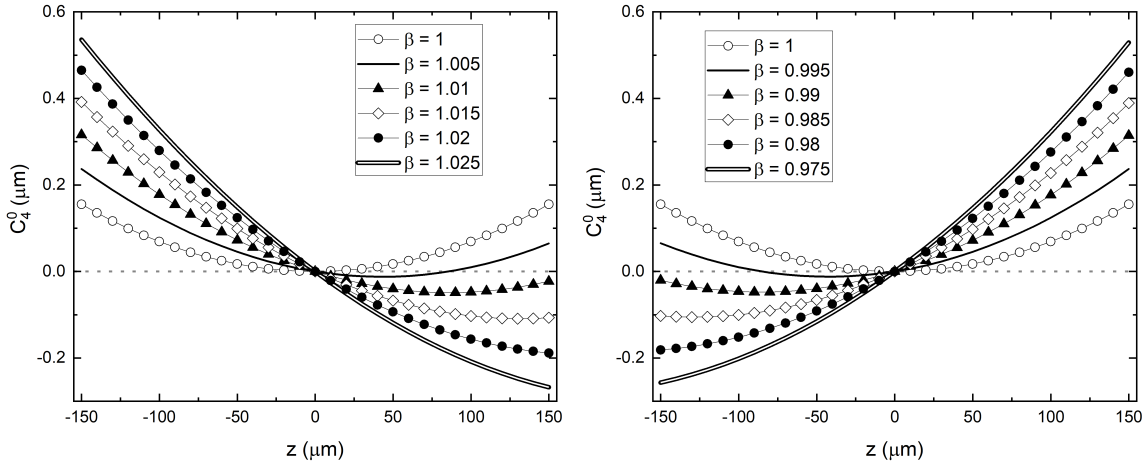

(a) (b)

Figure 2.8: Plots showing variation of spherical aberration coefficient (C_4^0) across z for small changes in magnification for (a) overmagnified ($\beta > 1$) and (b) undermagnified ($\beta < 1$) conditions.

2.3 Results and Discussion

2.3.1 Effect of Magnification Mismatch

To assess the increase in spherical aberration with depth we look at the change in first order spherical aberration coefficient (C_4^0) with z (Figure 2.8). The simulation was performed using two air lenses for O1 and O2 (0.95NA 40x, same as the experimental system in folded geometry) while changing β to reflect overmagnified and undermagnified conditions. For very small variations in β (<1.01), the contributions from the linear z terms from Equations 2.9 and 2.10 are just enough to balance out the quadratic terms. This results in an increase in the diffraction-limited range from 145 µm at $\beta = 1$ to 162 µm at $\beta = 1.005$. This aberration balancing also leads to the diffraction-limited range to be shifted on one side of the focal plane. However, as β increases, the linear z terms start to dominate showing rapid increase in spherical aberration on either side of the focus dramatically reducing the diffraction-limited range.

The spherical aberration coefficient obtained from the computational model was compared with the corresponding term from the experimental system. Figure 2.9

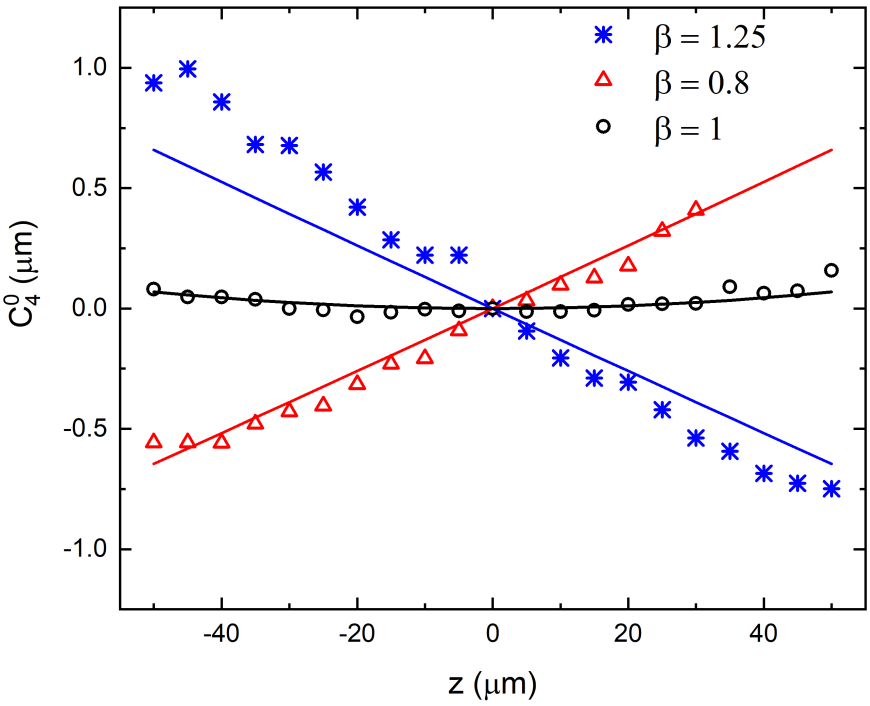

Figure 2.9: Verification of first order spherical aberration terms obtained from experiment for ideal ($\beta = 1$), overmagnified ($\beta = 1.25$) and undermagnified ($\beta = 0.8$) RF systems. These are compared against their corresponding simulation results shown in solid lines.

shows the change in C_4^0 with distance z for the three different magnifications of the relay lenses. For ideal magnification ($\beta = 1$), we see reduced amounts of spherical aberration across z. For $\beta \neq 1$ conditions, we observe the rapid increase in spherical aberration with distance from the focal plane. The deviation of the experimental values from the simulated results for $\beta = 1.25$ can be attributed to the presence of residual aberrations in the optical system due to alignment errors. The range over which the coefficient could be measured directly was limited by the dynamic range of the SH sensor. The measured coefficient can be seen to saturate close to the upper and lower limits of the axial range for both over and under magnified cases.

2.3.2 Decrease in Diffraction-Limited Range

The Strehl ratio was calculated for z ranging from -100 to +100 µm and the diffraction-limited range was defined for the axial region having Strehl ratio greater

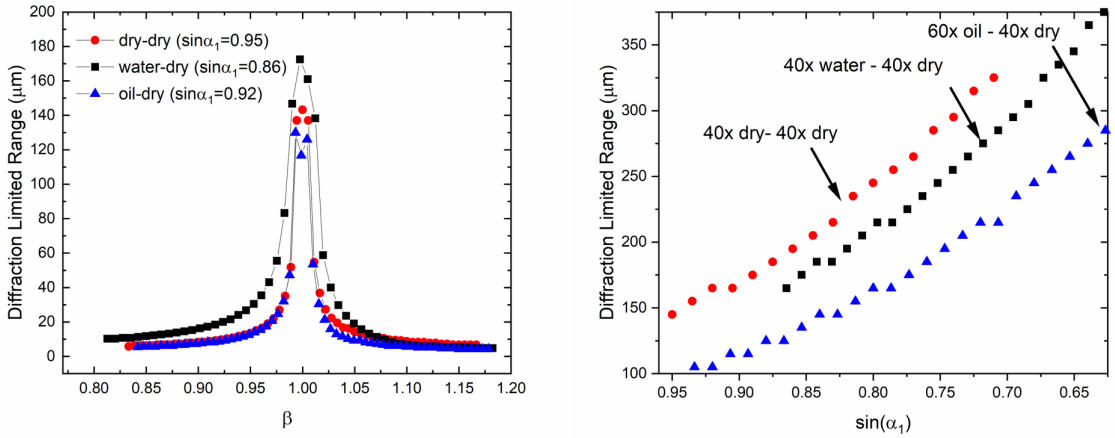

(a) (b)

Figure 2.10: (a) Plot showing the decrease in diffraction-limited range for three different O1-O2 objective pairs as a function of β. (b) The increase in diffraction-limited range with decrease in the maximum acceptance angle of O1 is plotted for the same objective pairs

than 0.8. We consider three high-NA imaging objectives for O1: 0.95 NA 40× dry, 1.15 NA 40× water immersion and 1.4 NA 60× oil immersion. For all three objectives, the same 0.95 NA 40× dry objective is used for O2. This ensures the acceptance angle for O2 is larger than or equal to O1. For all configurations, an approximate 1% change in β shows a decrease in the diffraction-limited range to at least half of the maximum value (Figure 2.10a). For this reason, we recommend measuring the magnification of the RF system directly, across the entire axial range with a precision of <0.1% in order to be able to obtain an accurate prediction of the achievable diffraction-limited range.

Higher-NA objectives generate spherical aberration at a much higher rate outside of the focal plane. The spherical aberration coefficient C_4^0 in the pupil plane of a single objective can be expanded as:

$$C_4^0 = nkz\left(c_1 \sin^4\alpha + c_2 \sin^6\alpha + c_3 \sin^8\alpha + ...\right) \tag{2.30}$$

where c_1, c_2 and c_3 are expansion coefficients [42]. This dependency on $\sin\alpha$ makes the corresponding high-NA RF system very sensitive to small deviations from the ideal configuration. In order to reduce this sensitivity, one can stop down

O1, which increases the diffraction-limited range at the loss of the system resolution (Figure 2.10b).

It should be noted that the computational model developed in this chapter uses the analytical formalism for the phase at the pupil plane for a point object shifted from the focal point in 3D object space (equations 2.7 and 2.8). The theory considers an ideal thin lens where the ray height at the pupil plane is calculated as the distance from the optical axis where the ray crosses the principal surface. In non-paraxial regimes, such as in an objective, the ray angles and the ray heights are related using the sine condition.

As illustrated in Figure 1.2a, the aperture stop is defined for an object at the focal point of the optical system and defines the maximum half-acceptance angle 'α'. For point objects shifted from this position, α might not be the limiting angle. Unlike ideal thin lenses, objectives contain multiple lens elements. The surface that acts as the aperture stop cannot be predicted without knowing the internal optical design. This effect of the change in the aperture stop position and limiting angles is not studied here. However, it will contribute to a less than ideal performance compared to that predicted by theory.

2.4 Conclusion

In this chapter, we have presented a computational method to quantify the imaging properties of a remote focusing system. This model includes non-ideal RF configurations where the magnification of the system deviates from the ideal value. A folded RF system was built with three different relay lens magnifications to verify the computational model. The first order spherical aberration term obtained from the experiments was found to be in close agreement with the simulated results. The model was then extended to calculate the decrease in diffraction-limited range for increasing magnification mismatch. We see that a 1% change in magnification decreases the diffraction-limited range to half of the maximum value.

The research presented in this chapter provides a better understanding of the tolerances of the RF system and the precision with which the magnification needs to be measured. Additionally, the computational model allows users to predict the potential loss in resolution when aligning with non-ideal magnifications. In the next chapter we apply the computational model to a microscope with an RF system used for routine biological imaging. We then characterise the system using PSF measurements in the presence and absence of magnification mismatch.

CHAPTER 3

COMPUTATIONAL MODEL APPLICATION

Sections of this chapter have been adapted from the paper *'Sensitivity of remote focusing microscopes to magnification mismatch'* [60].

From the results of Chapter 2, it is inferred that high-NA RF systems have tight alignment tolerances. An important aspect for wider utilisation of RF as a standard refocusing methodology is to provide a robust alignment procedure for the three high-NA objectives. In this chapter, the RF system is implemented along with an inverted microscope reducing alignment complexity. In addition to this, it allows for easier sample mounting on standard microscope stages. The alignment protocol and detailed characterisation for such a RF unit is discussed.

As an extension of Chapter 2, the performance of an RF system is quantified in the presence of a small amount of magnification mismatch. The motivation for this study is to perform PSF measurements across the remote volume as it is a standard procedure for resolution characterisation in microscopes. Experimental results show a clear degradation in resolution across the 3D volume for non-ideal systems. Finally, we use the results of this study to inform us on the methods by which the diffraction-limited volume can be increased further.

3.1 Methods

3.1.1 Optical Setup

Widefield RF Microscope

The RF system was built in unfolded geometry containing three microscopes in series (S1, S2 and S3). The first microscope was housed in an inverted Olympus IX73 stand. A 1.15 NA 40× water immersion objective (UAPON40XW340, Olympus) was used for O1. The correction collar on the objective was set to compensate for the spherical aberration introduced by the coverslip (#1.5 = 170 µm). The first tube lens forming the relay lens system (L1) is housed within the microscope stand and has a focal length of 180 mm.

In this configuration, the distance between O1 and L1 is unknown. To keep the distance between the back focal plane of O1 and L1 fixed, O1 is placed in the lower most position of the objective's axial travel range. This requires the sample to be brought towards O1's focal plane. This was done by mounting the sample on a piezo translator, PT1 (Q-545.140, Physik Instrumente).

The sample was illuminated using a Xenon arc lamp. A filter cube (GFP, Excitation: 457 nm /Emission: 502 nm) was used to split the excitation and emission paths.

Changing Magnification

The rest of the RF system was aligned outside the microscope stand. The refocusing and reimaging objectives (O2 and O3) are 0.95 NA 40× dry objectives (UPLSAPO40×2, Olympus). This required L2 to be a 135 mm focal length lens. The closest off-the-shelf lens $f_{L2} = 140$ mm (G063235000, Qioptiq Ltd) was initially used as L2. This resulted in $\beta = 1.04$. To get $\beta = 1$, L2 was combined with a 4000 mm focal length lens to give an effective focal length of $f_{L2} = 135 \pm 0.5$ mm.

O2 and O3 were aligned in a nose-to-nose configuration and glass coverslips (#

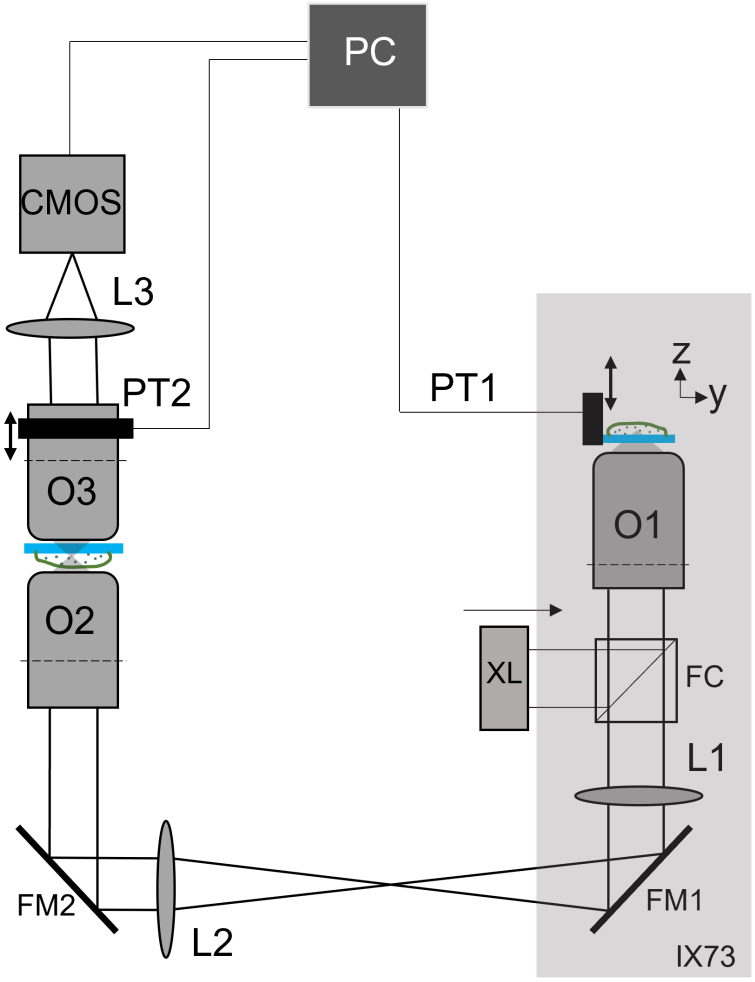

Figure 3.1: Schematic of the optical setup used for characterisation of the RF system: Collimated excitation light from a Xenon lamp is incident on the sample after passing through a filter cube (FC) and the imaging objective O1. The sample can be moved axially using a piezo translator PT1. The fluorescence emission from the sample is collected by O1. Tube lens L1 ($f_{L1} = 180\,\text{mm}$) along with the sample, O1 and FC are housed within the IX73 inverted microscope stand. Remote image of the sample volume is formed at the focal plane of O2. Depending on the focal length of L2, the system is either in an ideal ($f_{L2} = 135\,\text{mm}$, $\beta = 1$) or non-ideal magnification ($f_{L2} = 140\,\text{mm}$, $\beta = 1.04$) . The remote volume is scanned by O3 attached to a piezo translator PT2. Final image formed by tube lens L3 ($f_{L3} = 180\,\text{mm}$) is captured using a sCMOS camera. Micromanager software is used to control the two piezo translators and the scientific camera. FM1 and FM2 are fold mirrors used to steer the beam.

1.5, 12 mm diameter) were carefully glued on to the front end of the objectives. O3 was translated using a piezo translator PT2 (P-725K085 PIFOC, Physik Instrumente) to refocus the system at different depths of the remote volume. The final tube lens L3 has a focal length of 180 mm (#36-401, Edmund Optics). The images were captured using a sCMOS camera (Zyla 4.2, Andor Technology, Oxford Instruments).

Telecentric Alignment

One of the advantages of the remote focusing system used in our study is that it is coupled along with an Olympus IX73 inverted microscope. This allows us to easily swap between different NA 40x magnification water immersion objectives without introducing misalignment. O1 and L1 are contained within the IX73 microscope body and do not require additional alignment. However, the distance between these two optical elements (d_1) is unknown (Figure 3.2) and is not specified by the manufacturer. d_1 can also vary when O1 is translated axially to bring the object into focus.

In an RF system, O1 and O2 are placed in telecentric alignment for accurate mapping of the pupil planes and to eliminate depth dependant magnification in the remote volume. This requires the optical train from O1 to O2 to be in $4f$ alignment. We detail the procedure to obtain telecentric alignment for a system when d_1 is unknown.

We use an expanded and collimated laser beam to align the remote focusing system. We place an iris in the beam path to reduce the beam diameter (pencil beam) which is used for precise centring of the optical elements. In the alignment of the RF system, we toggle between getting the setup coaxially aligned and setting the correct distance between the optical elements. Here, we only discuss the latter part of that alignment procedure.

To place the optical elements at the correct distance from each other, the iris is opened to get the full diameter of the laser beam. O1 is translated to the lowermost

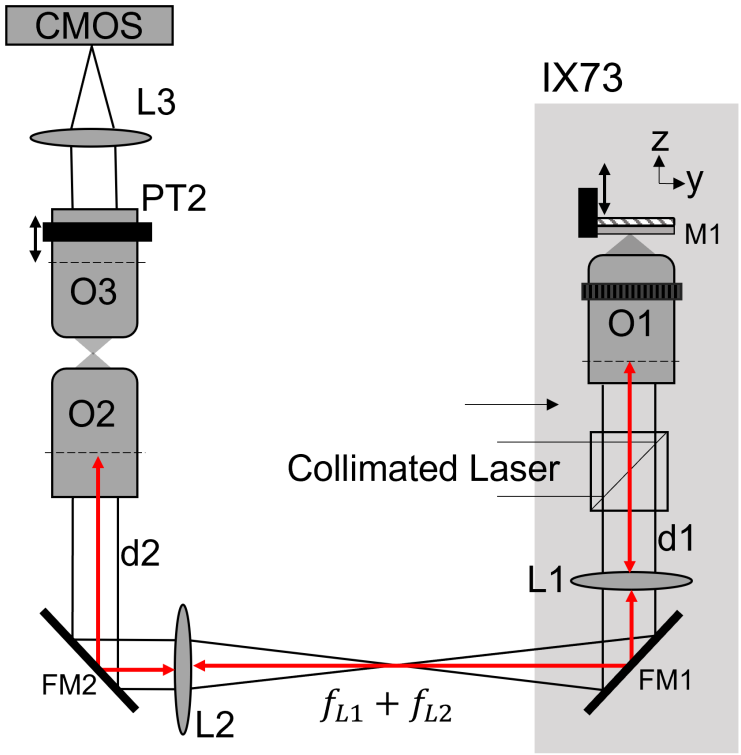

Figure 3.2: Remote Focusing system coupled along with an Olympus IX73 inverted microscope.

axial position minimising d1. The axial adjustment dial on the IX73 microscope is locked in this position. A mirror (M1) mounted on a kinematic mount is placed in the object space of O1 to reflect the beam and steer it back through O1 and out of the exit port of IX73. We ensure that M1 is at the focal plane by placing a shearing interferometer (Thorlabs, SI100) between O1 and L1 and checking if the output beam is collimated.

We then set the $2f$ distance between L1 and L2 by translating L2 in the z direction until we obtain collimated light at the output of L2.

Optical elements from O2 to the CMOS camera are placed on a rail (Thorlabs, XT95-1500 - 95 mm) perpendicular to the optical bench. The beam is steered into this path using the fold mirror FM2. Both O2 and O3 can be translated axially with respect to each other and additionally can be translated as a single unit along the rail.

As the distance d_2 is unknown we roughly place O2 at a distance equal to the

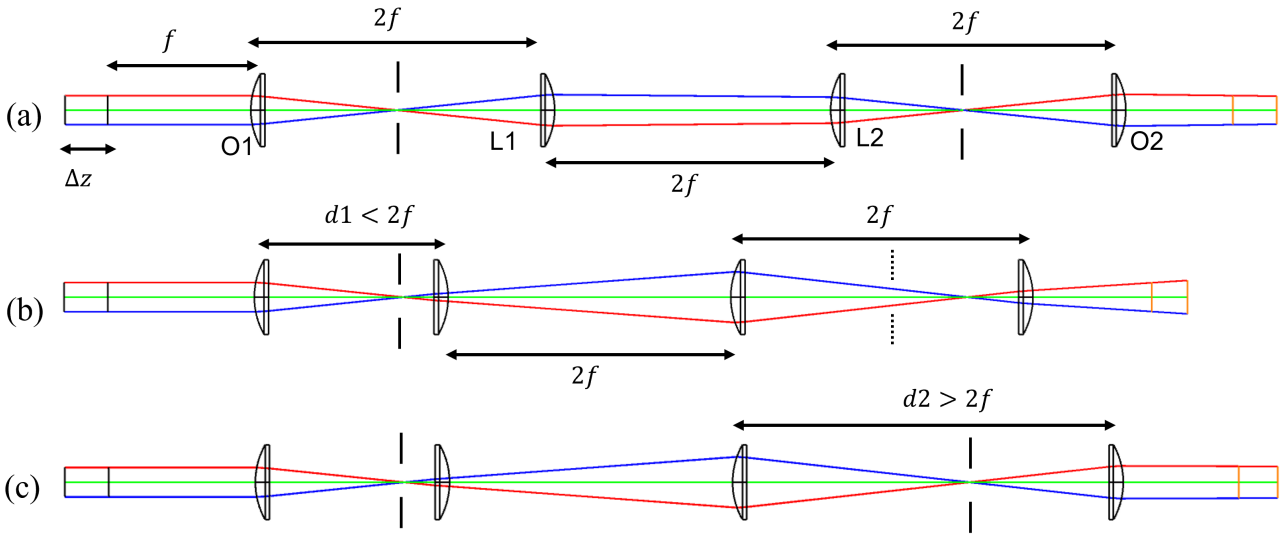

Figure 3.3: Four lenses labelled O1, L1, L2 and O2 have the same focal length f. The system images two extended objects placed at f and $f + \Delta z$. Similar to objective lenses, the aperture stop is set at the back focal plane of O1 and O2. (a) Shows the ideal configuration where the distance between O1-L1, L1-L2 and L2-O2 is equal to $2f$. If we trace the chief ray (blue and red lines), it passes through the centre of the two aperture stops. (b) Configuration similar to the microscope system used in this thesis where $d1 < 2f$. Here, the chief rays do not pass through the centre of the aperture stop (black dotted vertical lines) of O2 leading to depth-dependant magnification in image space. (c) O2 is shifted such that the chief rays pass through the centre of the aperture stop and the system is again telecentric. The simulation was performed on Zemax using a $f = 100$ mm lens (Thorlabs LA1050-A).

focal length of L2. In inverted microscopes, the distance between O1 and L1 is usually closer than the sum of their focal lengths [71]. In such cases, O2 will have to be shifted further away from L2 (Figure 3.3).

Next, we carefully set the relative distance between O2 and O3. We move O3 using the piezo translator PT2 to the mid point (200 µm) of its 400 µm scan range. We then translate O2 axially until we obtain a collimated beam at the output of O3. This ensures that the focal plane of O1 coincides with the midpoint of the scan range of the reimaging objective O3. It should be noted that the plane of best resolution shifts to the nominal focal plane in the presence of aberration balancing in the system. From here, O2 and O3 are translated together as a pair.

Once these distances are set, the microscope is setup again in the widefield

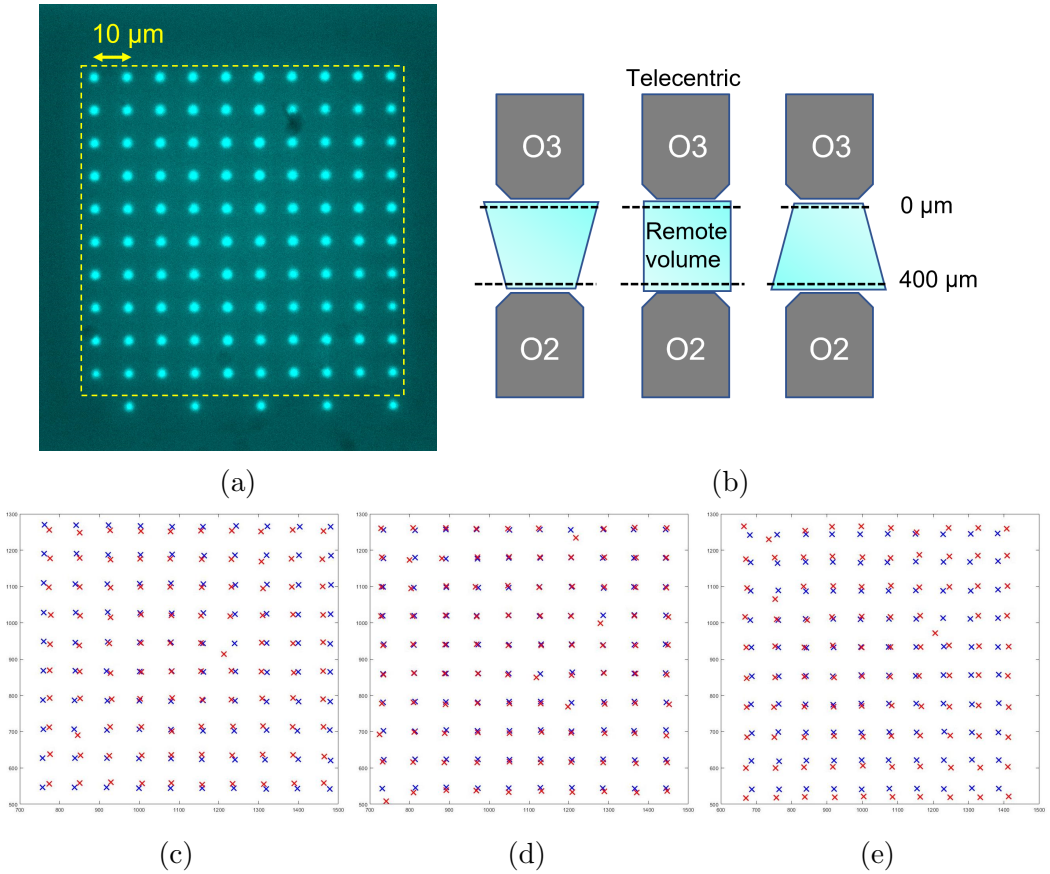

Figure 3.4: (a) Fluorescence calibration standard used to check for telecentricity. Dashed yellow lines show the features used for centroid detection. (b) Measuring the magnification near the start and end of the scan range of O3 verifies magnification change across the remote volume. (c) Change in relative magnification when PT2 is at 10 µm (blue cross) and at 360 µm (red cross). Here the BFP of O2 is below the telecentric position. (d) O2 is in telecentric position and (e) BFP of O2 is above the telecentric position.

fluorescence imaging mode. The distance d_2 is determined using a water index fluorescence calibration standard 'waterslide' which is mounted on the piezo translator PT1 (Figure 3.4a). We image a periodic array (10x10) of points on the waterslide, spanning across 100x100 µm of the lateral FOV. Such an array can be used to measure the absolute magnification of the remote volume (as shown in Figure 3.7). Here, we use it to set the unknown distance d_2.

PT1 is adjusted to bring the sample into focus when PT2 = 10 µm. From the captures image, we measure the centroids of the calibration pattern. We do the same at the maximum scan range position, PT2 = 360 µm. If the centroid superposition from these locations show the presence of distortion (Figures 3.4c and 3.4e), the O2-

O3 pair is translated axially until the distortions are compensated (Figure 3.4d). Once this position is set, the RF system has a telecentric alignment.

This method of finding the telecentric position removes the need of measuring the exact distance between O1 and L1. More importantly, knowledge of the exact location of the back focal plane of the objectives is not required.

3.1.2 Sample Preparation

A standard method of measuring the PSF of a microscope is to image subresolution fluorescent beads which act as point sources. The beads were suspended in agarose gel prepared at a concentration of 1 % (w/v) to obtain a refractive index of ≈1.333 [72].

We used yellow-green microspheres of 100 nm diameter (F8803, ThermoFisher) with excitation at 505 nm and emission at 515 nm. The concentrated colloidal bead solution was diluted in ethanol (1:1000 µL). This was performed to achieve a sparse distribution of beads across the sample which then allows for volumetric imaging without the need for sectioning. The diluted bead solution was then mixed with the melted agarose gel (1:22 µL).

The gel-bead mixture was allowed to set in a custom-made well chamber sealed using # 1.5 coverslips at both ends. The sample was made thick enough to image beads across the entire scan range of PT2.

3.1.3 Measurement of PSF

Image stacks were obtained by translating O3 every 0.2 µm using PT2 across a 400 µm range. The beads at every 5 µm depth was analysed using PSFj software [73]. With multiple beads present in a given Field of View (FOV), the average lateral and axial FWHM of the PSF was calculated to get the resolution of the system at each depth. As described in section 1.2.4, the theoretical FWHM for the current RF configuration can be calculated as:

$$\mathrm{FWHM_{x,y}} = 0.84\left(\frac{0.61\lambda}{\mathrm{NA}}\right) = 229\,\mathrm{nm} \tag{3.1}$$

$$\mathrm{FWHM_{z}} = 0.88\left(\frac{2\mathrm{n}\lambda}{\mathrm{NA}^2}\right) = 0.912\,\mu\mathrm{m} \tag{3.2}$$

Here $\lambda = 515$ nm, $n = 1.33$ and NA $= 1.15$. It should be noted that for $\beta = 1$ system, the magnification of the remote volume is 1.33 x. Therefore, a translation of 0.2 µm in the remote volume space corresponds to a shift of 0.150 µm (0.2 µm/1.33) in sample space. Similarly, for the $\beta = 1.04$ system, each 0.2 µm step is equal to 0.163 µm shift in sample space.

3.2 Results and Discussion

3.2.1 Computational Model Prediction

Using the computational model we predict the decrease in the diffraction-limited range for the ideal and non-ideal system. We see a seven-fold decrease in the axial range from 173 µm for β=1 to 25 µm for the β=1.04 RF system (Figure 3.5). The plot also shows the increase in the diffraction-limited range for small changes in magnification (around $\beta = 1.01$). This is due to the aberration balancing between the residual spherical aberration in the RF system and the aberration introduced by the magnification mismatch. This has been previously discussed in Chapter 2, section 2.3.1.

As described in Section 2.2.4, we set the boundary of the diffraction-limited range when the Strehl ratio falls to 0.8. Such a cut off is not defined for the PSF. Therefore, when characterising the system using PSF measurements, we choose a arbitrary percentage increase in the axial FWHM and compare between ideal and non-ideal systems.

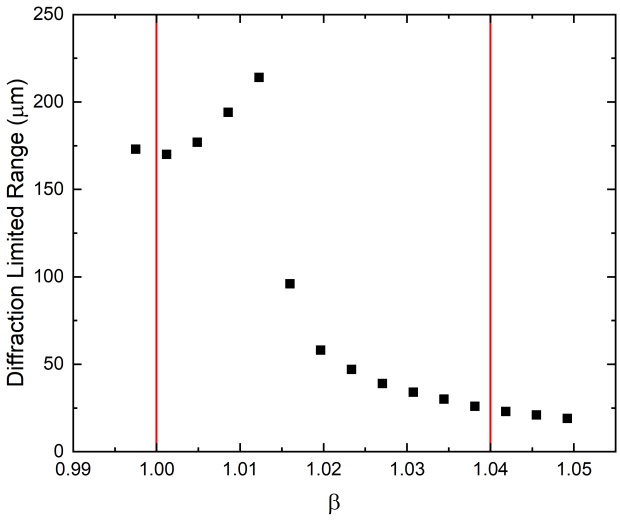

Figure 3.5: Decrease in Diffraction-Limited Range with small changes in β for the RF system described in this chapter. The vertical red lines indicate the axial range at β=1 and β=1.04.

Table 3.1: Decrease in axial imaging range going from $\beta = 1$ to $\beta = 1.04$ system

Percentage increase from $FWHM_z$ (%)	Axial range, $\beta = 1$ (µm)	Axial range, $\beta = 1.04$ (µm)	Factor Increase in axial range
10	75	27	2.7
20	124	74	1.6
30	161	105	1.5
40	184	148	1.2

3.2.2 PSF Measurement

The measured FWHM of the axial and lateral PSF were plotted against sample depth (Figure 3.6). Here, $z = 0$ is the focal plane of O1. To quantify the decrease in the performance of the two RF systems, we calculate the axial range where the measured FWHM is within 10, 20, 30 and 40 percentage of the theoretical $FWHM_z$ (Table 3.1).

Within a 10% increase of $FWHM_z$ ($\approx$1.0 µm), we observe that the $\beta = 1$ system has a 2.7x increase in the axial range. This drops to 1.2x for a 40% increase. At $z = 80$ µm, where the axial FWHM is equal to 1.2 µm for the $\beta = 1$ system, the axial FWHM increases to 1.65 µm for $\beta = 1.04$.

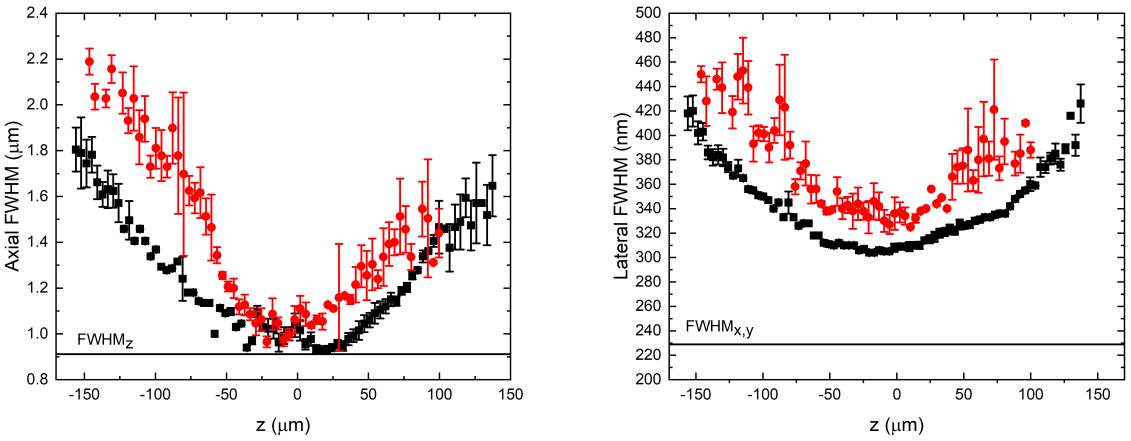

(a) (b)

Figure 3.6: FWHM of the (a) Axial and (b) Lateral PSFs. The black squares and red circles correspond to the β=1 and β=1.04 RF system respectively. The solid horizontal lines corresponds to the theoretically derived FWHM (from equations 3.1 and 3.2). The system refocuses deeper into the sample for increasing z.

It should be noted that even though the axial FWHM around the focal plane matches with $FWHM_z$, the lateral FWHM is at least 30% higher than $FWHM_{x,y}$. This discrepancy between the FWHM of lateral and axial PSFs and their theoretical values has been observed before in [73]. This is due to the scalar formalism used to derive equation 3.2, which applies to paraxial optics but underestimates the resolution obtained for high-NA objectives [74].

As the decrease in the axial range is not as dramatic as the computational model predicts we used a PSFCheck calibration slide to measure the magnification of the remote volume [75]. Though the measured magnification (Figure 3.7) is close to the expected value, due to low precision, there is some overlap between the two measurements. This could mean that the actual difference in magnification between the two systems could be lower than the calculated value. However, it can be inferred from the PSF measurements that the overall performance reduces for the non-ideal RF system.

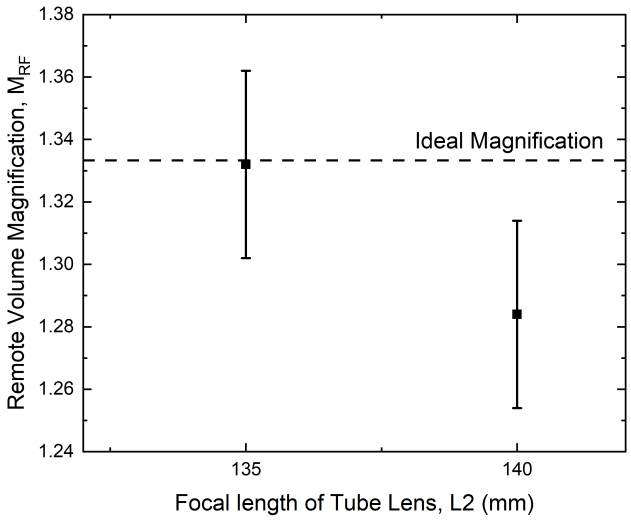

Figure 3.7: Measured magnification of the remote volume for $f_{L2} = 135\,\text{mm}$ ($\beta = 1$) and $f_{L2} = 140\,\text{mm}$ ($\beta = 1.04$) RF system. The horizontal dashed line represents the ideal magnification of the RF system: $M_{RF}^{Id} = \frac{n_1}{n_2} = 1.33$

3.2.3 Empirical validation

In chapter 2, we discussed the cancellation of the linear z-dependant terms for an ideal RF system (Equations 2.9 - 2.11). This is reflected in the symmetric profile of the curve corresponding to $\beta = 1$ in Figure 2.9 leading to positive spherical aberration on either side of the focal plane. Whereas for systems with magnification errors, there is a flip in the sign of spherical aberration from one side of the focus to the other. This information can be used as a practical guide when characterising an RF system to check if the final remote volume has been formed with uniform magnification of $\frac{n_1}{n_2}$.

The yz projections of the bead images were used to check the direction of elongation of the PSF 'tail' (Figure 3.8). For an ideal system ($\beta = 1$), positive spherical aberration is observed on either side of the focal plane where the axial profile is elongated towards the refocusing objective O2. Whereas, in an overmagnified system ($\beta = 1.04$) the sign of the spherical aberration changes from positive to negative from -z to +z.

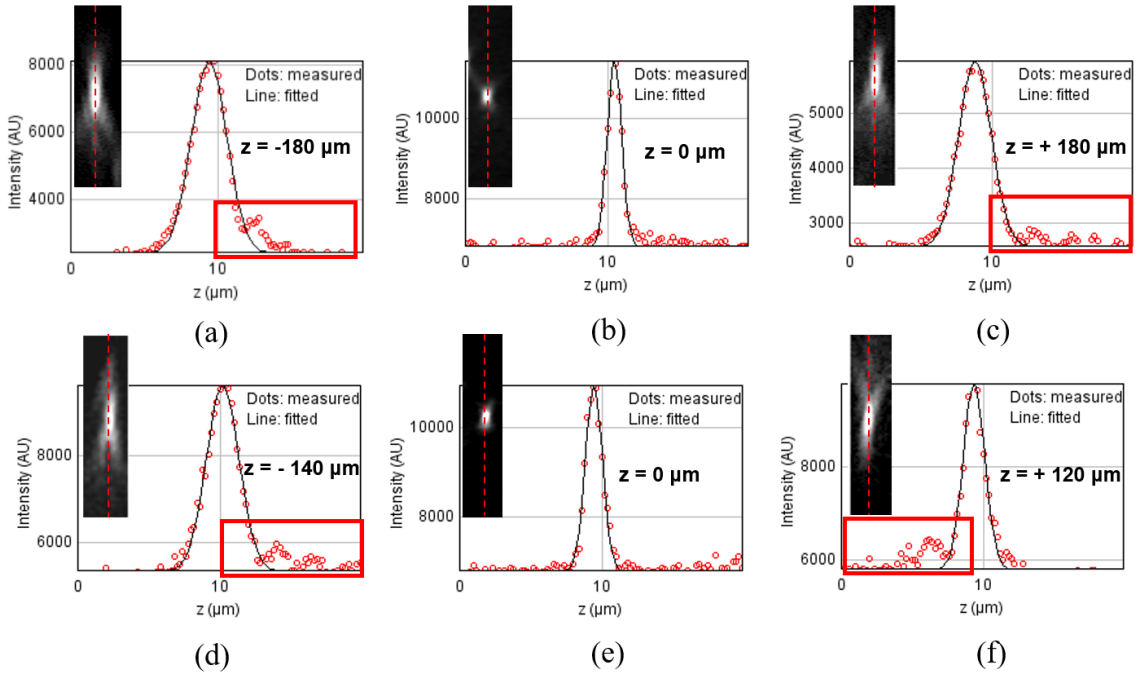

Figure 3.8: Qualitative assessment of magnification in an RF system. Positive z on the axis is towards the refocusing objective O2. Top row shows the line profile of the axial PSF taken for $\beta = 1$ at z = -180 µm (a), $z = 0$ µm (b) and $z = +180$ µm (c). Bottom row for $\beta = 1.04$ is imaged at z = -140 µm (d), $z = 0$ µm (e) and $z = +120$ µm (f). For a 1.15 NA water immersion objective, the diffraction-limited range is 173 µm (±86.5 µm). The PSFs shown for (a), (c), (d) and (f) above were acquired outside of this range to better visualise the change in the sign of the spherical aberration. The red boxes highlight the direction of elongation of the PSF tail for ideal and nonideal magnifications.

3.3 Conclusion

In this chapter we have presented a method of characterising the performance of an RF system using PSF measurements in addition to measuring the absolute magnification of the remote volume. For a magnification mismatch of about 4%, we observe a decrease in overall resolution across the remote volume due to the presence of increased residual spherical aberration when compared to an ideal RF system. Such characterisation of the system helps to quantify the axial range within which the resolution is sufficient to image the substructures of interest within the specimen. Additionally, we present a relatively easy method of checking if ideal magnification conditions have been reached by noting the direction of the elongation of the PSF 'tail' at the ends of the axial scan range of the remote volume.

In the next chapter, we apply the RF system and the characterisation procedures developed here to perform volumetric imaging of live biological samples. To implement in vivo imaging, we transform the widefield system to include sectioning capabilities via spinning disk to remove out of focus fluorescence.

CHAPTER 4

SPINNING DISK REMOTE FOCUSING MICROSCOPE

This chapter has been adapted from the research article *'Spinning disk-remote focusing microscope'* [61].

So far, we have discussed the possible limitations in the implementation of RF systems. In chapter 3, we built the RF system along with a standard inverted microscope and characterised it in widefield imaging modality. When performing volumetric imaging on biological samples with dense features, RF needs to be implemented along with sectioning methodologies.

The current chapter applies the RF system to perform volumetric imaging of live samples. This novel microscope combines the high-NA remote refocusing capabilities of the RF unit along with sectioning via spinning disk. To minimise complexity, a commercial off-the-shelf spinning disk unit was used (Clarity, Aurox Ltd.). The system was characterised similar to the procedure detailed in Chapter 3 and showed an axial and lateral FWHM of 5 µm and 490 nm respectively over a 130 µm axial range with a 256 x 128 µm FOV. The system was applied to image calcium-based neuronal activity at 1 volume/s in live *Platynereis dumerilli* larvae.

4.1 Introduction

RF can be efficiently combined with a variety of commonly used sectioning methodologies. This compatibility has been discussed in section 1.5. As an extension to the widefield RF system explained in Chapter 3, we introduce sectioning capabilities using structured illumination via spinning disk (SD). Being a parallelised

imaging technique, the SD unit allows for faster volumetric acquisition than standard confocal techniques. An added advantage being that, unlike current OPM implementations, the system does not require complicated off-axis alignment.

4.2 Methods

4.2.1 SDRF imaging principle

Following the widefield RF microscope configuration, the SDRF system consists of the IX73 inverted microscope and the RF unit (Figure 4.1). The spinning disk unit forms the structured illumination pattern at the focal plane of O3. When O3 is translated using the piezo stage PT2 (in Z), the illumination pattern is axially shifted around the focus of O2. As O2 is conjugate to O1, PT2 determines the depth into the sample the illumination pattern is formed. Due to the symmetry in the system, fluorescence from the plane of interest is collected by O1 and re-imaged by O3 on to the spinning disk. The fluorescent light is spatially filtered before being imaged on to the scientific CMOS camera.

4.2.2 The RF unit

The system components are the same as the widefield RF system except for the following: O1 is a 0.8 NA water dipping objective (LUMPFLN40XW, Olympus). This system was built before the compound 135 mm lens was available to us and therefore used the 140 mm lens for L2. This resulted in the system having a magnification mismatch of $\beta = 1.04$. The dichroic mirror (DM) after L2 is an optical flat with a broadband, visible spectrum coating (Chroma). The final achromatic 180 mm tube lens (L3, #36-401, Edmund Optics) was used to re-image the focal plane of the re-imaging lens onto the spinning disk (SD).

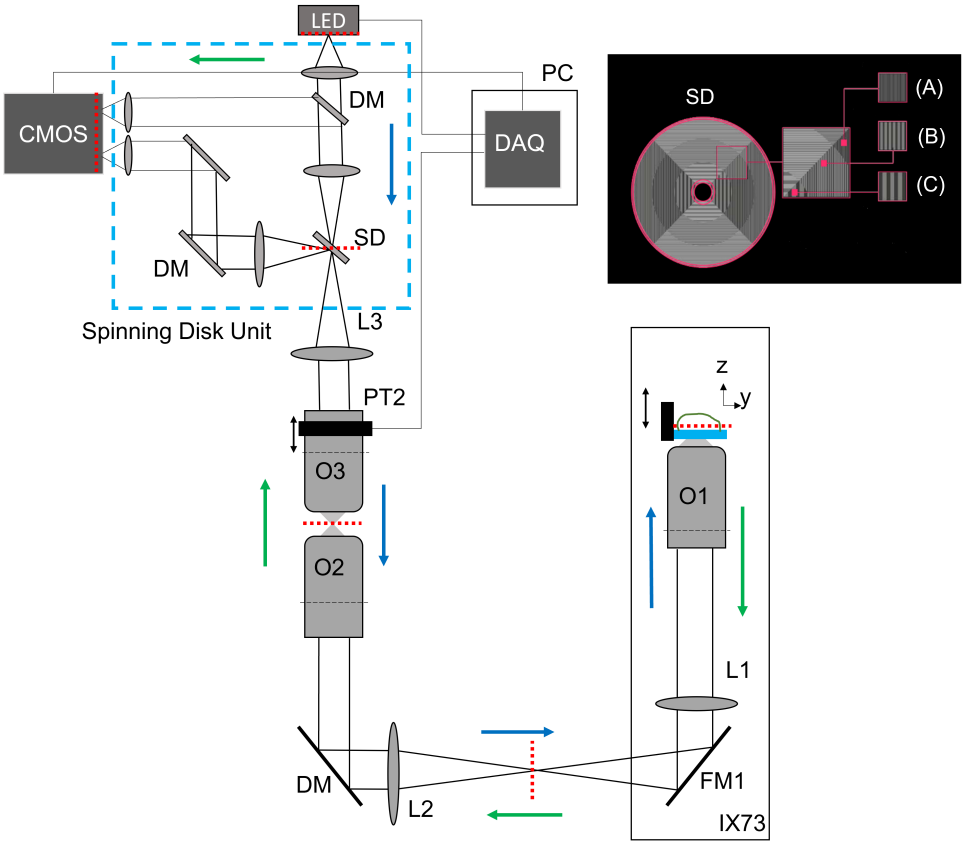

Figure 4.1: Schematic of the SDRF setup. In addition to the inverted microscope (IX73) and RF unit explained in Chapter 3, the system includes a spinning disk unit (within the blue dashed lines) allowing for sectioning capabilities. Other changes made to the system include using a 0.8 NA water dipping objective for O1 and L2 is a 140 mm lens resulting in non-ideal magnification. At the spinning disk (SD), the in-focus fluorescence passes through into the upper path on to one half of the sCMOS camera. The out of focus fluorescence is reflected by the SD and is imaged on to the lower half of the camera. The camera performs on-the-fly processing to provide a confocal image of the sample. Red dotted lines indicate the conjugate planes. PT2 translates O3 axially and determines the imaging plane within the sample. The inset shows the grid pattern etched onto the SD and provides high sectioning, medium sectioning and low sectioning capabilities. These are labelled as (A), (B) and (C) respectively. The inset is adapted from the technical notes provided by Aurox Ltd. [76]. DM - Dichroic Mirror.

4.2.3 The Spinning Disk Unit

Using the principles in reference [36], the quartz spinning disk (SD) is imprinted with a reflective binary grating pattern (shown in the inset of Figure 4.1). This grid pattern, compared to the traditional pinholes used in Nipkow disks, results in efficient use of the illumination light. This allows for the use of LEDs rather than lasers resulting in cheaper implementation of the optical setup. The grid pattern is made of 50% aluminium and 50% transmissive quartz, with light falling on the disk being reflected or transmitted. The spinning disk unit also provides sectioning capabilities corresponding to three different thickness of the transmissive and reflective regions of the grid pattern. This allows for imaging with low signal - high sectioning to high signal - low sectioning. In the 'bypass' mode, the spinning disk unit works as a widefield microscope.

The SD is aligned to be conjugate to the sample. Excitation light from the LED passes through the disk and the RF unit to be re-imaged in the specimen. Axially translating PT2, shifts the illumination plane across the sample. Fluorescence emission is de-scanned in z and is re-imaged on to the spinning disk. The SD is inclined with respect to the optical axis such that the in-focus fluorescence is transmitted through the disk and the out-of-focus light is reflected into a separate path. Each of these light paths are focused onto one half of the camera to form the raw image. A weighted subtraction between the in-focus and out-of-focus images provides high-contrast, optically sectioned images.

To reduce alignment and registration errors between these two imaging paths, the two halves of the image are aligned using an internal calibration pattern made available on the Aurox custom software.

4.2.4 Synchronised Imaging

As the camera captures both in-focus and out-of-focus images, the native resolution is halved to 2048x1024 pixels. A data acquisition card (PCIe-6363, National

Instruments) was used to generate an external trigger of constant frequency (1-20 Hz) with jitter ± 1 ms. This was found to be more accurate than the default camera trigger. MicroManager was used to control the timing for the camera frame buffer acquisition, frame exposure time, frame delay, PT2 drive signal and LED illumination. To reduce photobleaching in the live samples, the LED was triggered 'on' only during frame acquisition and the 'Fire All' TTL output of the camera was in the 'on' state.

4.2.5 Characterisation techniques

The SDRF system was checked for resolution and telecentricity across the remote volume of the RF system. The resolution measurements were compared against the 'RF-only' configuration where the spinning disk was replaced with the sCMOS camera. This is similar to the widefield system discussed in Chapter 3 (Figure 3.1). Additionally, the magnification and resolution measurements were taken in the 'side-port' configuration by placing the camera at the side port of the IX73.

The resolution at each depth was measured by imaging fluorescent beads as described in sections 3.1.2 and 3.1.3. The system magnification was measured using laser written fluorescence features on the 'waterslide' across the 400 µm scan range of PT2. It should also be noted that in this chapter, axial positions are stated in terms of the displacement of the piezo translator PT2, denoted by Z. These values can be converted to the shift from the focal plane in object space using the formula:

$$\text{Object Position (in z)} = (\text{Z} - 160\,\mu\text{m})/1.24 \tag{4.1}$$

Here, 160 µm corresponds to the position of the focal plane of O1 along the translation length of PT2. The factor 1.24 is the axial magnification if the lateral magnification across the remote volume is 1.28x (from equation 1.5).

Table 4.1: Magnification measurements for different microscope configurations.

Configuration	Magnification (xy)	Z scaling
Theoretical value	51.42x	1.33x
	Min. Max.	Min. Max.
Side port	40.0x 40.1x	1x 1x
SDRF	50.3x 51.6x	1.26x 1.28x

4.2.6 Sample Preparation for Live Imaging

The Platynereis larvae were GCaMP6-expressing via microinjection of GCaMP6s RNA (1000 µg/µL) at one-cell stage [77]. They were reared at 18°C on a 16 hour light 8 hour dark cycles until the imaging experiments. Experiments were conducted between 36 and 52 hour-post-fertilization. Live larvae were mounted for imaging on glass slides and held with a coverslip spaced with adhesive tape to avoid placing excessive pressure on the larvae.

4.3 Results

4.3.1 Magnification measurements

In the 'side-port' configuration, the mean lateral separation of the 10x10 features on the waterslide was measured to be 61.6 pixels. The pixel size of the Andor Zyla camera is 6.5 µm corresponding to 400.5 µm separation between two features. This gives an absolute magnification of 40.05x which is close to the expected 40x magnification of O1.

In the SDRF configuration, the final magnification is $(f_{L1}/f_{L2}) * M_{O1} = (180/140) * 40\text{x} = 51.42\text{x}$. At the focal plane of this system (PT2 = 160 µm), the magnification is shown be 51.1x. Shown in Figure 4.2, the system is not exactly telecentric as there is a 3% depth dependant magnification variation over the 400 µm scan range of PT2. In such cases, variation in lateral magnification will also change the axial scaling at each depth. The magnification measurement for each of the microscope configuration is listed in table 4.1.

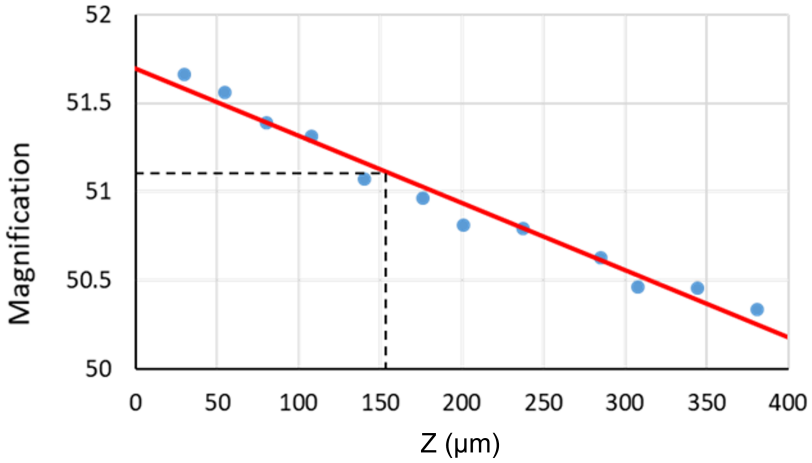

Figure 4.2: Variation of lateral magnification across the depth of the remote volume. The blue dots correspond to the experimental values and the red line is the line of best fit. At the focal plane of O1, PT2 = 160 µm, the magnification of the system is 51.1x.

4.3.2 PSF measurements

Using equations 3.1 and 3.2, the theoretical $FWHM_{x,y}$ and $FWHM_z$ for the 0.8 NA water dipping objective is 330 nm and 1.88 µm respectively. The variation in FWHM measurements across the scan range is shown in Figure 4.3. Maximum resolution for the SDRF system is observed around z = 50 µm - 100 µm. The plot further confirms that the performance of the 'RF-only' and SDRF configurations are the same.

There is a significant variation in the $FWHM_z$ values after z = 170 µm. This arose due to the warping of the dichroic mirror after L2, introducing astigmatism in the system in addition to the residual spherical aberration in the RF unit. These distortions to the axial PSF profile make a simple Gaussian fit to the central Airy disk erroneous in predicting the true axial extent of the intensity PSF.

The resolution of the system in 'side-port' configuration is shown as the solid black horizontal line in Figure 4.3. The FWHM in x-y and z for this configuration was measured to be 424 ± 10 nm and 4.6 ± 0.2 µm respectively. The reason for this significant degradation of the axial PSF is due to the introduction of a coverslip when imaging with a dipping objective. The coverslip was required to perform live imaging

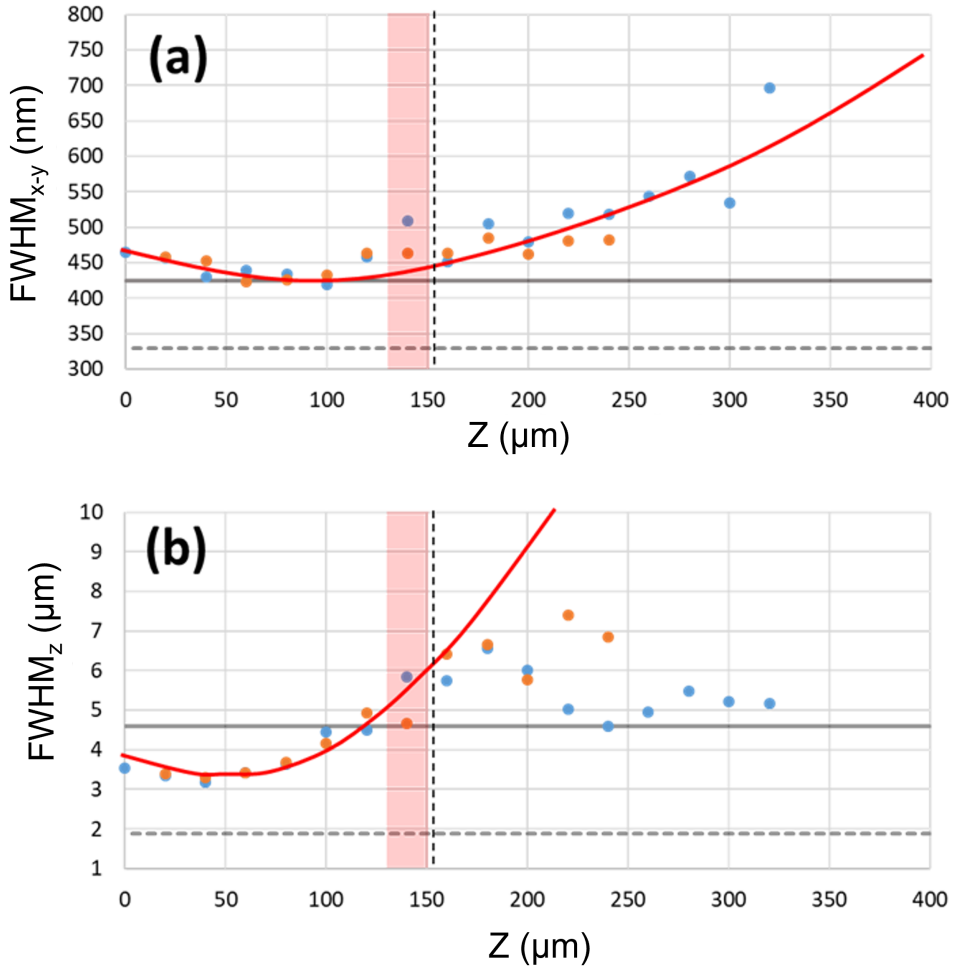

Figure 4.3: (a) Lateral FWHM of sub-resolution beads as a function of displacement of PT2 (Z). (b) Axial FWHM as a function of Z. The dashed horizontal lines denote the theoretical FWHM values. The dashed vertical line is the focal plane of O1. The solid black horizontal lines denotes the FWHM values measured in the 'side-port' configuration. The pink bars indicate the region where the live imaging of the larva was performed.

Table 4.2: PSF characterisation measurements for different microscope configurations.

Configuration	FWHM$_{xy}$ (nm)	FWHM$_z$ (µm)
Theoretical value	330	1.88
Side port	424 ± 10	4.6 ± 0.2
RF-only	424 ± 11	3.3 ± 0.3
SDRF	419 ± 22	3.2 ± 0.4

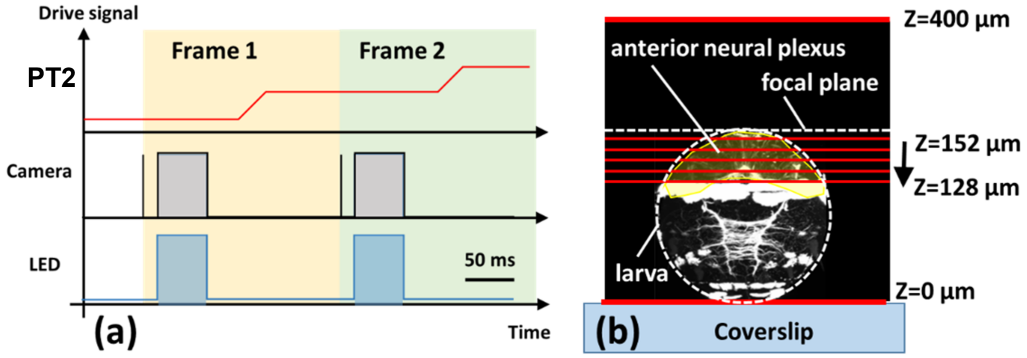

Figure 4.4: (a) Timing diagram for volume acquisition. (b) The red lines indicate the PT2 positions (Z) within the larva where the images were acquired. Image of the Platynereis larva adapted from reference [78].

experiments to support the sample from underneath on the inverted microscope. Interestingly we see that the SDRF and 'RF-only' configurations outperforms this value between z = 0 µm to 125 µm range. The reason for this behaviour is considered further in the discussion section. The PSF measurements for each of the microscope configuration are listed in table 4.2.

4.3.3 Volumetric Imaging in *Platynereis dumerilii*

As discussed in the previous chapters, remote focusing allows for rapid imaging of volumes without introducing vibrational artefacts. We have demonstrated this by imaging live *Platynereis dumerilii* larvae. A two day old larvae is largely spherical with a diameter of about 125-175 µm. We set up a five frame stack to image the anterior neural plexus which extends across most of the anterior hemisphere of the larva (Figure 4.4b).

Increase in the position of PT2 (Z) indicates imaging deeper into the sample. The images were captured from $\sim$ 15 µm from the surface of the larva to $\sim$ 40 µm deep into the sample in steps of 6 µm. Scans started from Z = 152 µm and ended at Z = 128 µm (Figure 4.4b). The volume was imaged for 10 seconds with a 5 Hz frame rate resulting in a sampling of 1 volume/s.

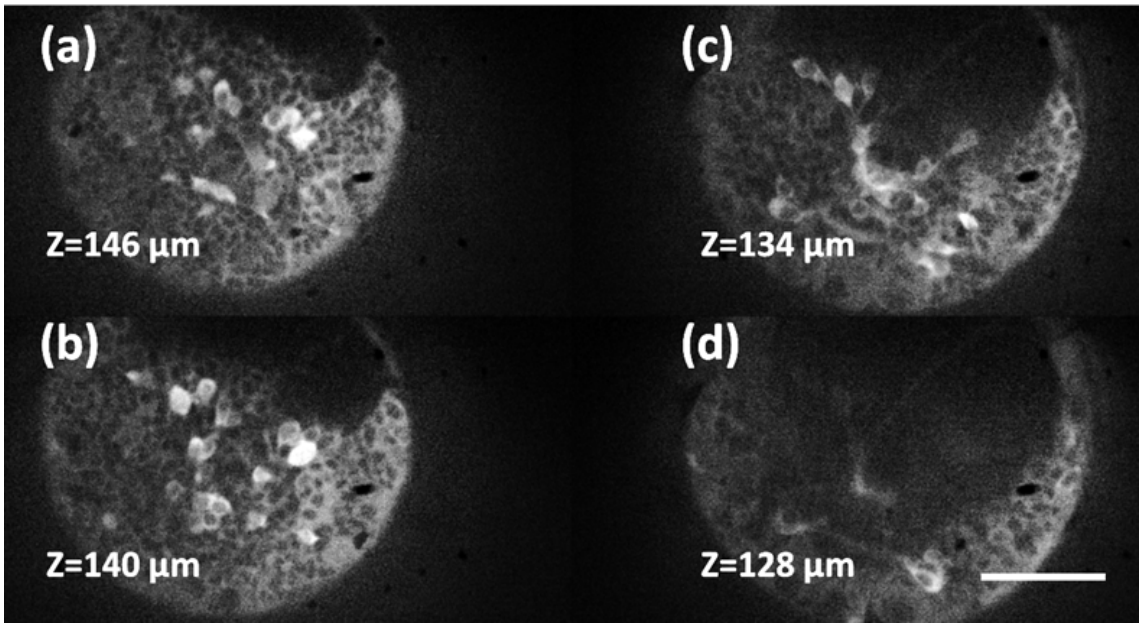

Figure 4.5: Four of the five sections imaging the anterior neural plexus of the *Platynereis dumerilii* larva (anterior view). The axial sections are separated by 6 µm. Scale bar: 50 µm.

Figure 4.4a shows the timing diagram for the volumetric image acquisition. Acquisition starts with the frame trigger signal being sent to the camera (vertical black line). The frame exposure starts after a 30 ms delay for 50 ms (grey box). To reduce photobleaching in the live samples, the LED was switched 'on' only during frame exposure. After frame acquisition, the drive signal was sent to PT2 leaving a 150 ms window for translation and settling ($\sim$25 ms). Therefore, two frames were acquired with a temporal separation of 200 ms.

Figure 4.5 shows four of the five planes imaged for each volume. The SDRF microscope is able to provide cellular resolution at each of the depths. It was also able to detect electrical activity for normal spontaneous behaviour due to Ca^{2+} flux associated with the action potential bound to the genetically expressed GCaMP. Highlighted in Figure 4.6a, three ROI containing 64x64 pixels were defined to calculate the traces of electrical activity. At each time point and at each depth, the intensity values within each ROI were averaged to get the average fluorescence (F). The relative change in fluorescence was then calculated (ΔF/F). Due to the low baseline noise level of < 0.03 for quiescent traces, averaging over multiple traces was

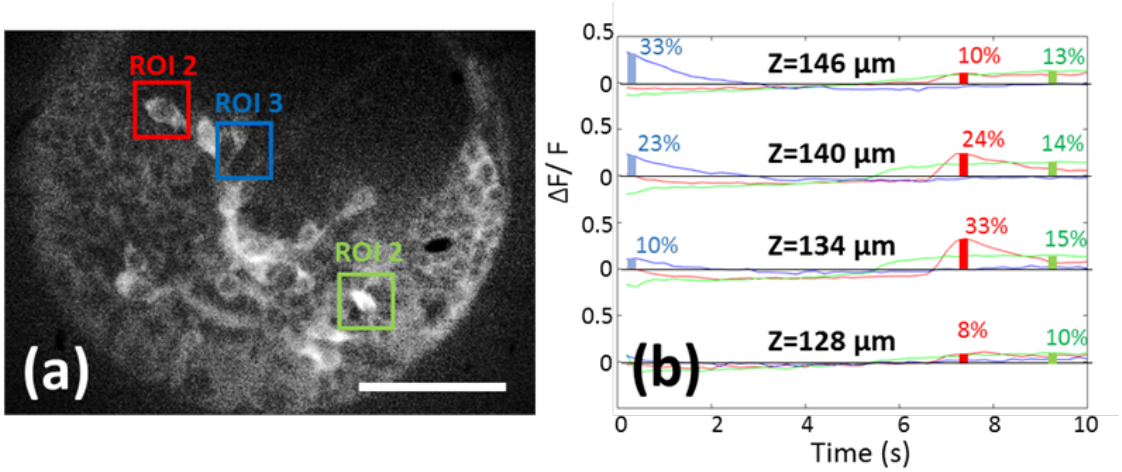

Figure 4.6: Electrical activity measured through Ca^{2+} binding to GCaMP. (a) The three regions of interest (ROI) highlighted were defined for all the four planes. Scale bar: 50 µm. (b) Fluorescence changes relative to average fluorescence ($\Delta F/F$) as a function of time for the four planes. The volumes were acquired for 10 seconds. Overlays indicate values of ($\Delta F/F$) at three distinct time points.

not required which improved sensitivity.

4.4 Discussion

4.4.1 Improving temporal resolution

The biggest bottleneck in improving the temporal resolution in the current SDRF system has to do with the translation of PT2. PT2 has to move, stop and settle before the camera is exposed for the next frame after which PT2 is again translated. This scanning procedure forms a large fraction of the volume acquisition duty cycle. An alternative is to implement extended depth of field (EDOF) imaging where PT2 is translated across the volume within a single frame exposure [79]. This method optically integrates the sectioned images to compress the 3D stack into a 2D image on the detector. For this 2D image to be optically sectioned, PT2 needs be translated by less than the axial FWHM of the SDRF system during the time the spinning disk takes to complete one revolution. The spinning disk rotates at a speed of 3000 rpm. Therefore, for an axial FWHM of 4 µm, the translation speed corresponds to <12 mm/s with a frame rate of 120 Hz over a 100 µm axial range. This method

is feasible to implement in the current SDRF system, however, for thick samples, integrating over the volume can hide fluorescent changes.

Other approaches to improve the temporal resolution would be to reduce the exposure time or the number of frames in a stack. However, these parameters are set largely by the sample. The exposure time is determined depending on the signal to noise ratio and is a function of the number of fluorophores in the sample. It is possible to increase the emission flux by increasing the excitation intensity, however, this leads to rapid photobleaching in the sample. The minimum axial sampling is determined by the axial FWHM of the system. However, the axial frame separation can be increased if the features of interest are separated by a larger distance.

4.4.2 Improving spatial resolution

The main factor affecting the spatial resolution of the SDRF microscope was the introduction of a sample coverslip when using a dipping objective. Even though a significant degradation in the lateral FWHM was not evident, the axial resolution was affected. This is due to the refractive index mismatch between the glass coverslip and water immersion which results in a static amount of spherical aberration across the imaging volume.

A clever method to mitigate this issue was shown by Yang et al in reference [80]. In an RF system, the NA of O2 is effectively transformed to that of O1. Therefore, removing the coverslip on O2, which is an air-spaced objective (UPlanSApo40X2, Olympus), cancels out the aberrations introduced by the presence of a coverslip at O1. This allows for the use of water dipping objectives with long working distances along with samples supported by coverslips.

It is observed that the axial resolution for the SDRF and 'RF-only' configurations exceed that measured for the 'side-port' configuration. This behaviour can be attributed to aberration balancing in the system. The introduction of equivalent and opposite aberration in the optical train of the microscope can cancel the static

aberration introduced by the coverslip. A likely reason for this is the non-ideal magnification of the RF system introducing additional residual spherical aberration in the microscope which could compensate for the static spherical aberration.

Another source of aberrations was the 3 mm thick dichroic mirror after L2 which introduced astigmatism into the system. This mirror was replaced with a prism fold mirror as used in chapter 3 (FM2 in Figure 3.1).

4.5 Conclusion

In this chapter, we presented the capability of remote focusing system to perform volumetric imaging of live *Platynereis dumerilii* larva. Sectioning capabilities using an off-the-shelf spinning disk was introduced to allow for fast confocal imaging. We were able to obtain an axial and lateral FWHM of 5 µm and 490 nm respectively over a 130 µm axial range with a 256 x 128 µm field of view (FOV). The calcium-based neuronal activity of the larva was imaged at 1 volume/s.

In chapters 3 and 4, we have observed that there is a rapid decrease in resolution away from the nominal focal plane - even for an ideal RF system. When imaging biological samples, additional aberrations are introduced due to index mismatch between the sample and immersion media. This informs the study in the next chapter where we try to improve upon the diffraction-limited axial range provided by an ideal RF system by performing adaptive aberration correction using the correction collar on an immersion objective.

4.6 Contributions

The microscope was developed along with Dr. Michele Gintoli and Dr. Alex Corbett. Implementation of synchronised imaging using Micromanager and subsequent analysis to retrieve the electrical activity across the sample was performed by Dr. Michele Gintoli. Dr. Elizabeth Williams prepared the larval samples for live imaging.

CHAPTER 5

RESIDUAL ABERRATION CORRECTION IN REMOTE FOCUSING SYSTEMS

In the previous chapters we have explored the limitations and application of the RF technique. Now, we investigate a possible method to improve on current RF systems. The performance of an RF system can degrade due to non-ideal alignment of the optical system and from sample-induced aberrations. We focus our efforts in compensating for system induced aberrations. In particular, we try to correct for residual aberrations in an ideal RF system. Such compensation can reduce the discrepancy between the theoretically predicted axial range and experimentally obtained one. The motivation for this project is to obtain an extended diffraction-limited volume for imaging biological samples.

The aberration compensation has been implemented using the correction collar on the water immersion objective. First, the origin of residual spherical aberration in an RF system is discussed. Next, the RF system from Chapter 3, modified for Shack-Hartmann wavefront measurements is described. In parallel, we employ PSF measurements to calculate reduction in spherical aberration after compensation. The study is extended to understand the contribution of off-axis aberrations to the image quality. In the final sections, the implications of the experimental findings and the possibility of improving current RF methodology is discussed.

5.1 Introduction

We first consider the two sources of spherical aberration in a remote focusing system.

Refractive index mismatch

Spherical aberration is introduced in the presence of refractive index mismatch between the immersion media of the objective and the specimen (Figure 5.1b). It is depth-dependant and increases with increasing depth for a homogenous index-mismatched sample [20]. In volumetric imaging of thick biological specimens, local changes in the refractive index can induce varying amounts of aberration at different depths. This when combined with imaging dynamic processes in live samples requires active aberration compensation techniques.

Another source of index mismatch is the introduction of a coverslip in the optical path to support the sample. These glass coverslips introduce spherical aberration especially in air and water immersion lenses. However, immersion objectives are internally corrected to compensate for coverslips of specific thickness. High-NA objectives have low tolerance to variations in coverslip thickness and therefore include correction collars to cancel the residual spherical aberration generated by the coverslip. As such, correction collars are routinely used to compensate for spherical aberration in an optical microscope irrespective of its origin [81, 82]. As the collars are designed to compensate for spherical aberration, off-axis aberrations such as coma and astigmatism cannot be corrected [83].

Residual Lens-induced Spherical Aberration

An RF system is constructed to cancel spherical aberration generated from defocused positions. However, for high-NA systems, the experimental diffraction-limited range is about half of the theoretically predicted range [32, 62]. This decrease is attributed to the assumption in the simulation that the lenses are ideal and perfectly obey the sine and Herschel condition within 3D Field of View (FOV). In non-ideal lenses as shown in Figure 5.1a, spherical aberration is introduced as the focal length changes with the ray height. Interferometric measurements of the pupil plane of high-NA objectives show an increase in phase error towards the edges of the pupil [84]. As

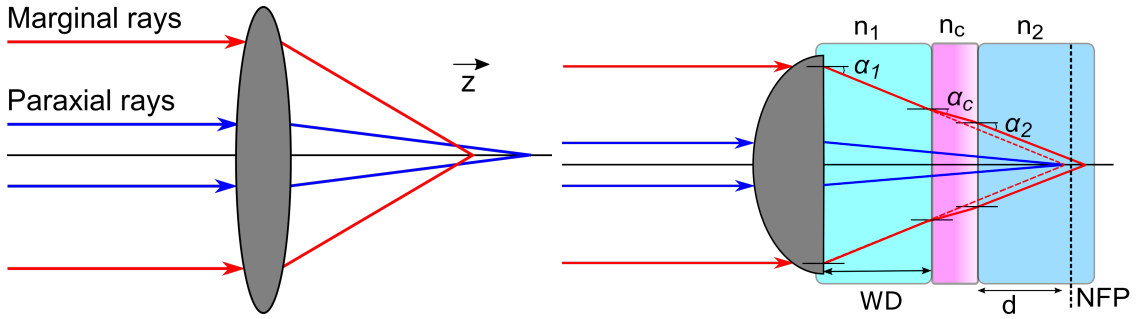

Figure 5.1: (a) Lens-induced spherical aberration where the marginal rays are focused at a different axial position compared to the paraxial rays. (b) Specimen-induced spherical aberration. The objective lens images into three different media - the immersion media having a refractive index of n_1, the coverglass (n_c) and the sample (n_2). Immersion objectives are corrected for the spherical aberration introduced by the coverslip. Additional spherical aberration is introduced if $n_2 \neq n_1$. α_1, α_c and α_2 are the angles of refraction for the converging marginal ray in the respective medium. In the presence of spherical aberration, the focal plane shifts to the nominal focal plane (NFP). WD is the working distance of the objective when $d = 0$.

this phase error may not be compensated for by the refocusing objective O2, it can result in increasing amounts of uncorrected residual aberrations. It should be noted that if non-ideal RF systems ($\beta \neq 1$) are built as described in previous chapters, it results in additional residual depth dependant spherical aberration.

In this chapter, we primarily focus on using the correction collar to improve the diffraction-limited range by compensating for the residual lens induced spherical aberration in an ideal RF system ($\beta = 1$).

5.2 Methods

5.2.1 Simulation

The collar on the primary imaging objective O1 (UAPON40XW340, Olympus) can correct for coverslip thickness between 130 µm and 250 µm. We use the following formalism to predict the range of spherical aberration correction that can be provided by the correction collar [85]:

$$\mathrm{OPD}_c = -\mathrm{n}_1 \sin\alpha_1 d_t \left[\sqrt{\frac{1}{\sin^2\alpha_c} - \rho^2} - \sqrt{\frac{1}{\sin^2\alpha_1} - \rho^2}\right]. \tag{5.1}$$

OPD_c is the optical path difference introduced by the correction collar for all rays across the pupil. d_t is the difference in the correction collar position and the coverslip thickness. In our experiments, a 170 µm coverslip was used and if the collar was set to the CC = 150 µm position, d_t = 20 µm. If an index matched immersion medium is used, α_1 is equal to the maximum acceptance angle of the objective. Therefore, the term $\mathrm{n}_1 \sin\alpha_1$ is the NA of the objective. α_c is the angle of refraction of the marginal ray in the coverslip. α_c can be calculated using Snell's law where $\mathrm{n}_c \sin\alpha_c = \mathrm{n}_1 \sin\alpha_1$. For a glass coverslip, $\mathrm{n}_c = 1.515$. ρ is the normalised pupil radius (Figure 2.2a). A negative sign is included as the correction collar introduces opposite amounts of aberration as introduced by the coverslip. As discussed in section 2.2.3, the optical path difference across the pupil is then decomposed to individual Zernike terms to obtain the amount of first order spherical aberration (Figure 5.5a).

In Chapter 2, we discussed the calculation of the residual spherical aberration present in the defocussed positions in a remote focusing system. We do the same for an ideal magnification system where O1 is a 1.15 NA 40x water immersion objective (Figure 5.5b).

5.2.2 Shack-Hartmann Setup

We modify the experimental setup in Chapter 3 (Section 3.1.1) to measure the amount of spherical aberration in the remote focusing system using a Shack-Hartmann sensor. In the present study, the RF system has an ideal magnification ($\beta = 1$). A 50:50 plate beamsplitter (Thorlabs, BSW10R) is mounted in the filter wheel of the Olympus IX73 to reflect the collimated laser light towards O1 (Figure 5.2). Mirror M1 is placed at the focal plane of O1. A thin layer of water is sandwiched between the mirror and a 170 µm coverslip with the space between the

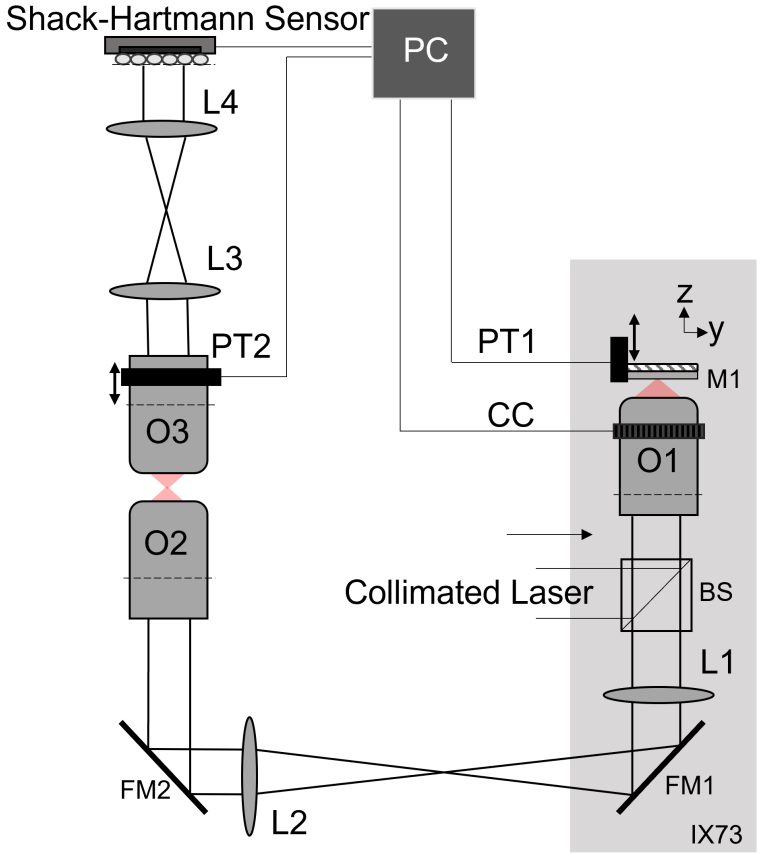

Figure 5.2: The ideal remote focusing setup from Chapter 3 modified to measure the residual spherical aberration at defocused positions using a Shack-Hartmann sensor. O1 is a 1.15 NA 40x water immersion objective. O2 and O3 are 0.95 NA 40x air spaced objectives. The back focal plane of O3 is mapped on to the Shack-Hartmann sensor using L3-L4 relay lenses. The rotation of the correction collar is automated to provide precise adjustment.

coverslip and the objective filled with a drop of water. M1 is defocused using the piezo translator PT1. The system is refocused by translating O3 using PT2. The piezo translators are controlled using Micromanager software. The back focal plane of O3 is mapped onto the lenslet array of the Shack-Hartmann sensor using relay lenses L3 and L4. The final pupil diameter mapped on to the sensor is equal to the pupil diameter of O1 multiplied by the magnification of L1 and L2 (0.75x) and the magnification of L3 and L4 (0.6x).

5.2.3 Automation of Correction Collar

The correction collar on O1 needs to be set at different positions depending on the spherical aberration compensation required. O1 (UAPON40XW340, Olympus) has a correction range from 130 µm to 250 µm with major ticks every 40 µm and minor ticks every 20 µm. As repeatable and precise adjustment was required, the collar rotation was automated.

A stepper motor (Sanyo Denki, 103H5208-5240) was coupled to the correction collar using a timing belt (Figure 5.3). The objective was fit with a 3D printed gear so that timing belt could effectively grip the collar. The motor was controlled using an Arduino UNO microcontroller and an A4498 driver [86]. Most stepper motors rotate in steps of 1.8° (200 steps = 360°). We set the A4498 driver to allow for microstepping which increases the resolution of the steps and facilitates smooth rotation of the collar, albeit with reduction in the output torque. For the current application, the system was configured to microstep to a quarter of the original resolution (800 steps = 360°).

A novel addition is the use of an absolute encoder (Bourns, EMS22A) which was coupled to the shaft of the stepper motor to provide positional feedback. The encoder uses the Serial Peripheral Interface (SPI) protocol for synchronous communication with the microcontroller. The encoder has a resolution of 1024 positions (0.35°) with an accuracy of ±1.4° which translates to ± 1° on the correction collar (gear

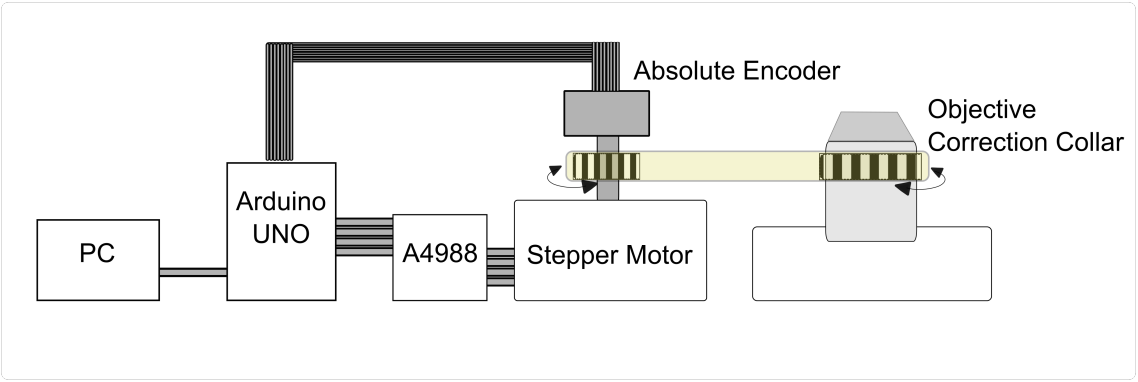

Figure 5.3: Schematic showing the setup used to remotely set the position of the correction collar. The stepper motor is controlled using an Arduino UNO as the microcontroller and an A4988 driver. The gear on the motor shaft is coupled to the correction collar using a timing belt. The absolute encoder sends positional information back to the microcontroller. The user serially communicates with the microcontroller via the PC.

ratio = 1.46).

Feedback from the encoder allows us to set the positional limits at the ends of the rotation range of the collar. It also allows for the setting of a 'Home' position which is a reference position that the user can set (e.g.: 0.17 in the case of using a 170 µm coverslip). In our microscope, where the markings of the collar are positioned away from the user, the feedback gives us the position of the collar and the compensation being applied at different depths.

The collar rotates through an 120° arc to provide correction from 130 µm to 250 µm. A single step of the motor allows for a 1.2 µm correction (change in coverslip thickness) to be applied. As the spacing between the collar marking are not uniform across the 120° range, the rotation was calibrated to take this account.

The PC communicates with the microcontroller using serial commands. A GUI developed on Labview allows the user to set the speed, direction of rotation, home position and the limits of rotation (Figure 5.4). The custom script uploaded to the Arduino UNO board reads the serial commands and sends TTL signals to the driver to rotate the motor. It simultaneously receives data from the encoder regarding the positional information which is serially read by Labview and displayed in the GUI.

With the current implementation, the collar can be rotated at a maximum speed

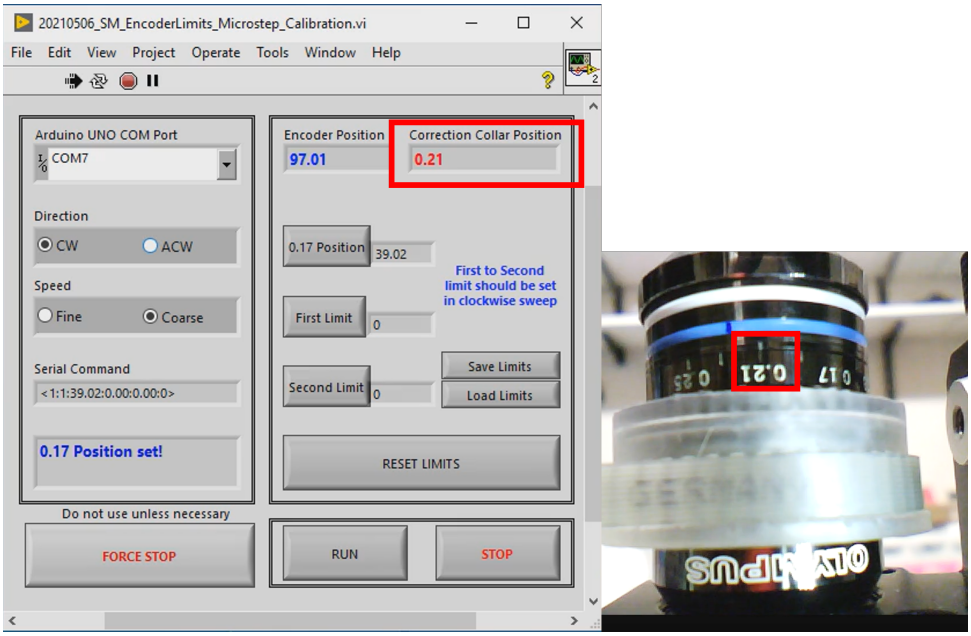

Figure 5.4: The Labview GUI allows to set the direction, speed of rotation and positional limits. Feedback from the encoder (highlighted in red) informs the user of the current collar position and therefore the compensation being applied to the RF system.

of 0.6 degree/ms. However, for the current experiments, the collar was rotated at low speeds so as to not disturb the sample. In addition to performing repeatable and accurate remote adjustment, the current implementation is cost effective with the entire setup costing less than £100.

5.2.4 Axial FWHM measurements

The improvement in axial resolution due to spherical aberration cancellation was also measured using the axial FWHM of sub-diffraction 100 nm fluorescent beads (F8803, ThermoFisher). The general methodology of sample preparation and PSF measurement is explained in detail in section 3.1.2 and section 3.1.3. A 1% Agarose gel solution was used to suspend the beads. O3 was scanned through the remote volume across a range of ±200 µm in 0.2 µm steps. To measure the effect of the lateral (x-y) FOV on the average Axial FWHM, the image stack was cropped to approximately half (148 x 148 µm) or to just the centre (45 x 30 µm). Error bars indicate standard deviation of axial FWHM for beads taken within a specific lateral

FOV. For small lateral FOV at least three beads were included in measurement.

5.3 Results and Discussion

5.3.1 Shack-Hartmann Measurements

We first measured the amount of spherical aberration generated by the correction collar. Mirror M1 was placed at the focal plane of O1 and the correction collar was rotated across its full range. Outside the CC=170 µm position, increasing amounts of spherical aberration is introduced in the system. The introduction of spherical aberration by the correction collar generates a small amount of defocus which is compensated by O3 to get $C_2^0 = 0$. From Figure 5.5a we observe that the experiment is largely consistent with the simulation predictions.

To measure the amount of residual spherical in the remote focusing system, M1 is defocused by z and the system is refocused by translating O3 by 2 x 1.33 x z. Simulation predicts introduction of positive residual spherical on either side of the focal plane in an ideal remote focusing system with a theoretical diffraction-limited range of 175 µm for a 1.15 NA 40x water immersion objective. The experimental remote focusing system has a diffraction-limited range of 90 µm (Figure 5.5b).

When the correction collar is rotated incrementally towards the CC=130 µm position, negative spherical aberration cancels out the residual aberrations in the system in the defocused positions. For positive z, the maximum correction required at the 75 µm position was CC=154 µm. When high amounts of spherical aberration is present at defocussed positions, such as in the -75 µm position, the collar was not able to not completely compensate even at CC=130 µm. We also observe an increased amount of second order spherical aberration in this region (Figure 5.5d). After collar correction, we get an enhanced diffraction-limited range of 145 µm.

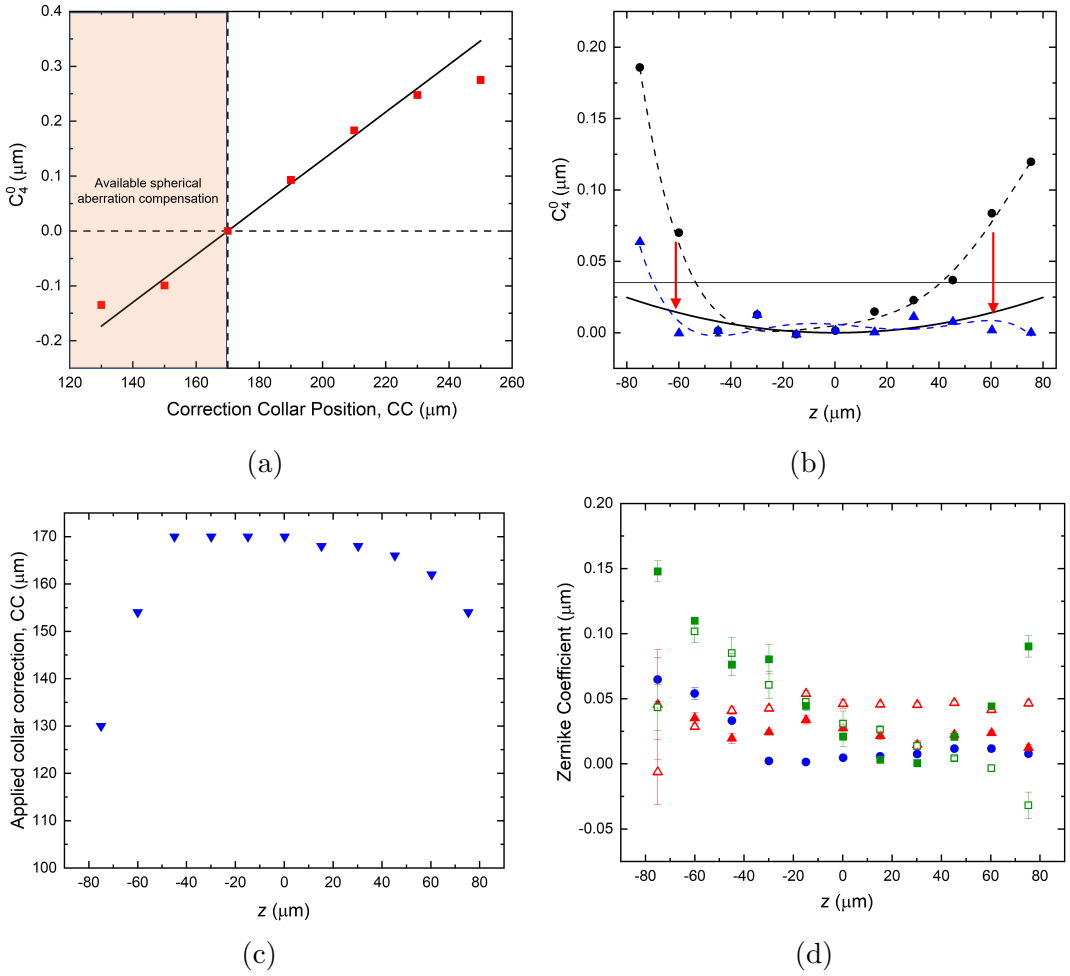

Figure 5.5: (a) Spherical aberration generated at different positions of the correction collar when using a 170 µm coverslip. Solid line is the simulation prediction and the red squares are the experimental values. (b) Residual spherical aberration in an ideal remote focusing system. Solid black curve: Simulation prediction for ideal remote focusing system. Black circles: Experimental residual spherical aberration. Blue triangles: System corrected for spherical aberration using the correction collar. Black horizontal line indicates the threshold above which the Strehl ratio decreases below 0.8. (c) Position of the correction collar when correcting for residual spherical aberration in the RF system at different depths. (d) Residual aberration coefficient in the RF system. Solid blue circle: second order spherical aberration. Open red triangle: Y astigmatism. Solid red triangle: X astigmatism. Open green square: Y coma. Solid green square: X coma. The Zernike polynomials for these aberration terms are defined in Chapter 2, section 2.2.6

5.3.2 Bead Measurements

We measured the spread of the axial PSF by measuring the axial FWHM of the fluorescent beads at various depths of the sample volume averaged across half of the lateral FOV (148x148 µm). Figure 5.6b shows that the Nominal Focal Plane (NFP) was shifted from the focal plane of O1 by +50 µm. This could be due to aberration balancing in the system. The presence of static spherical aberration also required the collar to be at 150 µm to reduce the aberrations over the entire range.

However, further introduction of negative spherical aberration did not improve the axial resolution at defocused positions (shown here for CC=130 µm in Figure 5.6b). The system forms a typical 'W' curve where the introduction of negative spherical aberration reduces the resolution and increases the axial FWHM around the nominal focal plane of the system (Figure 5.6a,(v)). However, it is expected to provide diffraction-limited imaging at two planes on either side of the NFP. The position of these planes should move outwards from the NFP as the amount of negative aberration introduced in the system increases.

It should be noted here that rather than imaging beads, similar PSF measurements can be performed using a collimated laser and focusing it on to a mirror placed at the focal plane O1. This greatly simplifies finding the centre of the FOV and improves contrast obtained at defocused positions. However, this experiment cannot be currently implemented due to the high amounts of astigmatism introduced by the 50:50 plate beamsplitter mounted on the filter wheel of the IX73 microscope required to steer the laser into O1.

In the following sections, we investigate the reason for the correction collar not providing residual aberration compensation in the remote focusing system.

5.3.3 Effect of Coma on the Axial PSF

The primary assumption made at the start of the study was that the elongation of the axial PSF and therefore the axial FWHM is only affected by spherical aberration.

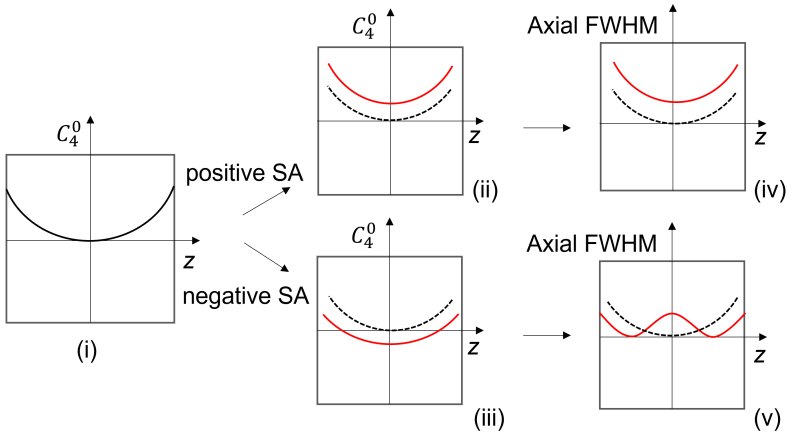

(a)

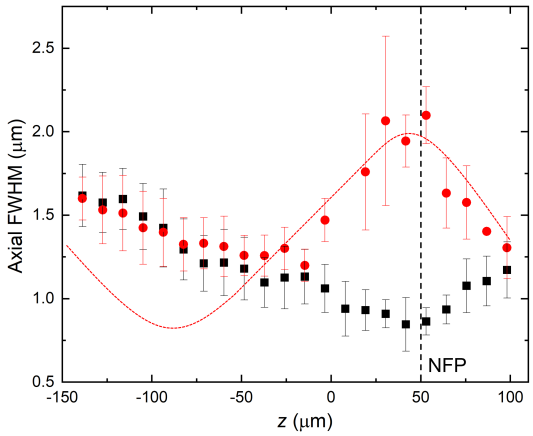

(b)

Figure 5.6: (a) An ideal remote focusing system (i) having positive spherical on either side of the focal plane requires the introduction of negative spherical (iii) to cancel the aberrations in the defocused positions. It results in a 'W' shaped profile (v) when measuring the axial FWHM. (b) Axial FWHM measured at defocused positions in the RF system. The focal plane is shifted from $z = 0$ to the NFP ($z = 50\,\mu m$). Axial FWHM when CC=150 µm (black squares). Additional negative spherical is introduced by rotating the collar to the CC=130 µm position (red circles). The red dashed curve illustrates the trend that was predicted.

However, looking at the individual bead profiles, it was evident that coma reduces the axial resolution. This could be due to vignetting effects as the off-axis beam is clipped at the edges of the aperture stop. We demonstrate this by introducing coma into the system at the NFP by misaligning the folding mirror FM2 5.7a. Increasing the beam tilt, increases the amount of coma resulting in increased axial FWHM. This results in a characteristic curved axial profile when the axial projection is taken in the direction of the coma 'tail'.

Coma is introduced in the remote focusing system in one of two ways: a) optical misalignment and b) field-dependant coma.

Optical misalignment, in particular lateral misalignment between optical components can introduce a constant amount of coma across the FOV. It is also introduced when the coverslip on immersion objectives (especially for water and air lenses) is tilted [87]. The current optical configuration of the remote focusing system contains three objectives all requiring coverslips. The sample holder used with the piezo translator PT1, contains clamps to hold the sample in place. However, the clamping mechanism introduced sample tilt, therefore tilting the coverslip. The sample was imaged unclamped to remove coverslip induced coma. As seen in Figure 5.7b, the axial FWHM for a clamped sample shows a significant decrease in resolution.

Field-dependant or off-axis coma is introduced when the object is laterally shifted away from the optical axis. Therefore, the amount of coma increases with field height. The field number specified by objective manufacturers denotes the magnified lateral FOV that can observed through the eyepiece. It is assumed that the objective is well corrected for off-axis aberrations within this flat field. For a remote focusing system, the usable lateral FOV decreases away from the NFP due to the increase in off-axis aberrations. Unlike coma introduced via misalignment, off-axis coma is due to the departure from sine condition at defocused positions and cannot be improved upon for a given remote focusing system without additional off-axis aberration correction methodologies.

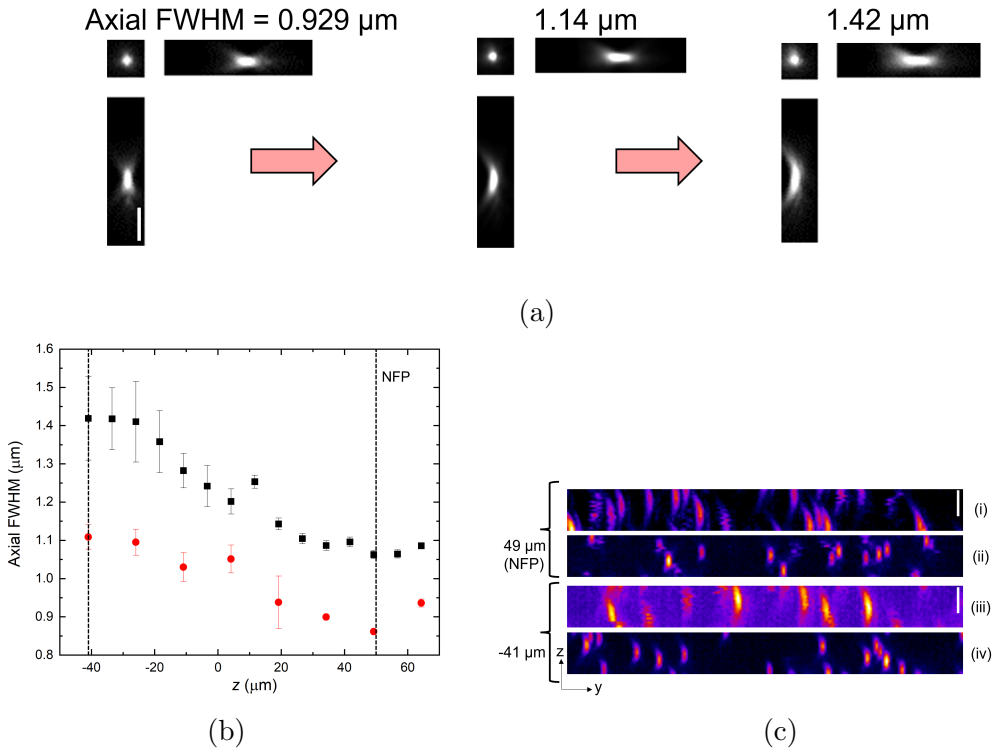

Figure 5.7: (a) Coma introduced by misaligning FM2 and resulting increase in axial FWHM. Scale Bar = 2 µm (b) Axial FWHM due to coma introduced by coverslip tilt (black squares) and corrected for the same tilt (red circles). (c) yz projections of the axial FWHM at the z planes indicated by the vertical dashed lines in (b). (i) and (iii) correspond to the system with coma. (ii) and (iv) are corrected for coma. Scale Bar = 2 µm

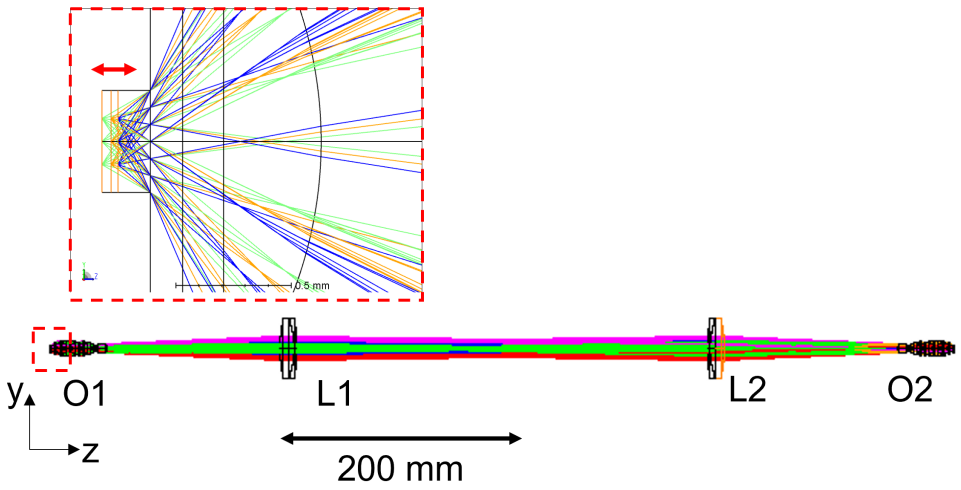

Figure 5.8: Zemax simulation of an RF system where O1 and O2 are 1.4 NA 40x oil immersion objectives and L1 and L2 are 180 mm lenses. The inset shows the enlarged portion of the object space where the shift in the working distance is introduced for on-axis and off-axis objects.

5.3.4 Simulation of Off-Axis Aberrations

We further investigate the decrease in the diffraction-limited FOV by performing ray tracing simulation using Zemax (Figure 5.8). Here, two Olympus 1.4 NA 60x oil immersion objectives were used as O1 and O2. The Zemax optical design for this objective is made available in references [88, 89]. Optical designs are rarely shared by objective manufacturers; therefore, the authors have inferred the design from patents for objectives that closely match with commercial products [90]. In these patents, the lens curvatures, refractive index of the glass, Abbe number and distance between the lens elements are specified. However, details of lens diameters are absent. To confirm the correct lens dimensions, some of the objectives were disassembled. The authors further confirmed the design by reproducing distortion and spherical aberration plots from the patents.

For the tube lenses, a two-inch diameter lens with focal length of 180 mm was used (Thorlabs, AC508-180-A). The simulation was performed for the wavelength λ = 587.5 nm. The system specifications showed the back focal plane of the objectives

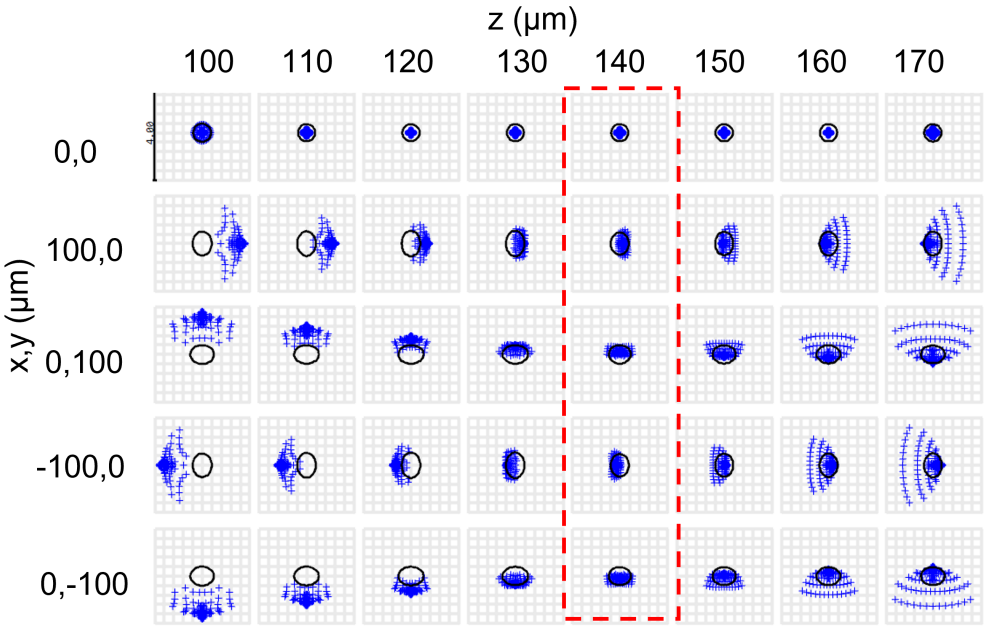

Figure 5.9: Multi-configuration spot diagram showing the effect of off-axis imaging using an RF system. The object position is shifted by changing the thickness of the immersion medium. Each column corresponds to a 10 µm shift in axial position of the object with the red highlighted column corresponding to the native focal plane of the objective. The rows show the change in field positions (x,y) in micrometers. The black circles in each graph corresponds to the Airy disk.

to be at -31.5 mm from the final lens element. The tube lenses were then placed in telecentric alignment with the objectives. The working distance (140 µm) of O1 was varied by changing the thickness of the immersion media layer resulting in change in the axial position of the object. Additionally, imaging at off-axis positions was studied by shifting the object ± 100 µm in x and y. The closest commercial Olympus objective is a 1.4 NA 60x apochromat objective 'PLAPON60XOSC2' which has a field number of 22 mm allowing for imaging across 366 µm lateral FOV.

The spot diagram for the various object positions is shown in Figure 5.9. The system images at the focal plane when the working distance is set at 140 µm (highlighted with dashed red line). The simulation is carried out across -40 µm to +30 µm from the focal plane in steps of 10 µm. As expected, for on-axis position (x,y) = $(0, 0)$ across the axial range, the system is diffraction-limited as the rays fall within the Airy disk (black ellipse). However, when evaluating for off-axis positions for the

same axial range, the system can no longer be considered diffraction-limited.

The ray fan for off-axis positions outside the focal plane is shaped typical of coma aberration. This is not the case for positions inside the focal plane where the ray fan presents a more complicated distortion, possibly due to the effect of multiple aberrations. The results from the simulation confirm the experimental observation regarding the decrease in the diffraction-limited lateral FOV for an ideal RF system.

Given that coma affects the axial FWHM and the amount of coma present in a remote focusing system increases with defocus even for well aligned systems, we try to measure the dependence of the axial FWHM on the size of the lateral FOV. Additionally, we investigate the amount of degradation in the axial PSF resulting from residual spherical aberration.

5.3.5 Effect of Residual Spherical Aberration on Image Quality

The aim of the experiment was not just to correct for on-axis spherical aberration but to improve the range of diffraction-limited imaging and therefore the image quality at defocused positions. It was assumed that the major contributor to the degradation in image quality was residual spherical aberration. If the increase in axial FWHM is mainly due to off-axis aberrations, the use of correction collar cannot improve the diffraction-limited range (observed for comatic aberration in Figure 5.6b).

We show that decreasing the FOV from half to the centre of the lateral FOV decreases the measured axial FWHM (Figure 5.10a). This is especially evident near the NFP where only small amounts of residual spherical aberration is present in the system. Selecting a larger FOV also results in a larger spread of values due to radial increase in the axial FWHM from off-axis aberrations.

We characterise this further by looking at the increase in the axial FWHM from the centre to the edge of the lateral FOV. We show this at the NFP and at $-90\,\mu m$ shifted position. Close to the optical axis, the residual spherical aberration only

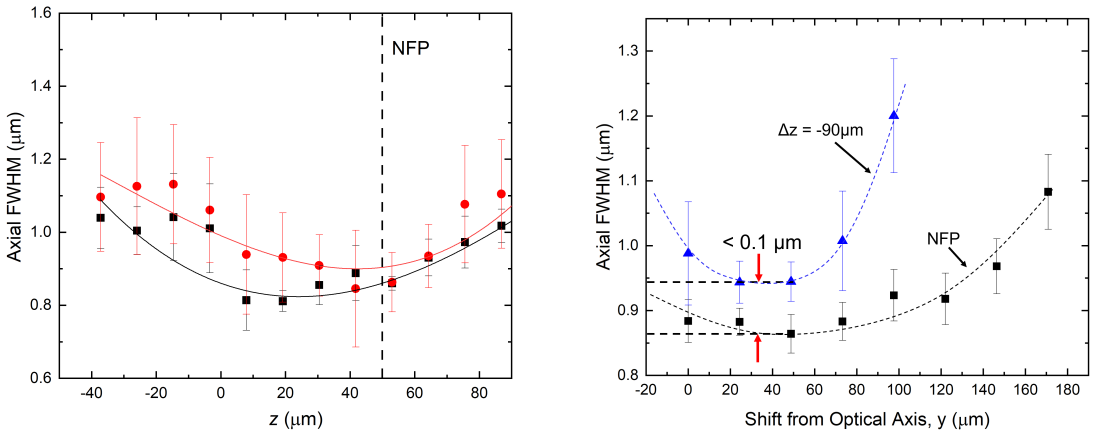

(a) (b)

Figure 5.10: (a) Red circles: Axial FWHM measured for half of the lateral FOV (148 x 148 µm, black squares) and only for the centre of the FOV (45 x 30 µm, red circles). (b) Variation in the axial FWHM across the lateral FOV at the NFP (black squares) and at the 90 µm shifted (blue triangles) position.

amounts to a 0.1 µm increase in the axial FWHM in the defocused plane (Figure 5.10b).

This shows that in order to obtain a significant improvement in image quality outside the experimental diffraction-limited range (and even within it), off axis aberrations should be compensated. This correction cannot be performed using a correction collar. However, static spherical or sample induced spherical aberration at defocussed positions can still be compensated for using the collar.

5.4 Conclusion

The current remote focusing system has an axial FWHM of 1 µm across 75 µm axial range. This range is extended if smaller lateral FOVs are chosen. Depending on the application and type of sample, this is sufficient in obtaining cellular resolution across an extended volume. However, as most samples introduce additional aberrations, it is desirable to offset for aberrations originating from the optical system. Our aim was to improve the diffraction-limited range using the correction collar. However, it was observed that contribution to the degradation of the axial PSF by spherical aberration was minimal. This means that the correction collar cannot improve

upon a well aligned ideal remote focusing system. Additionally, we note that the rapid rotation of the correction collar on the imaging objective O1 can introduce vibrational artefacts. However, utilising the correction collars on O2 or O3 will provide the same compensation as O1 without introducing sample perturbation.

We also comment at the drawbacks of the metrics used in the current study. The Shack-Hartmann setup does not provide information regarding the reduction in the lateral FOV. Furthermore, in the current double-pass configuration, coma being an odd aberration would be cancelled. Measuring the axial FWHM of the sub-resolution beads gives a good indication of the effect of all aberrations and therefore an indirect measure of the image quality. However, it is difficult to extract the effect of a single aberration on the PSF when multiple aberrations are present in the system.

CHAPTER 6

DISCUSSION AND FUTURE OUTLOOK

In chapter 1, the need for rapid, agitation-free refocusing when imaging biologically relevant specimens was discussed. Another requirement is for the sample volume to be imaged with isotropic high resolution. Remote focusing resolves both of these bottlenecks by introducing a second high-NA objective in the optical path to cancel aberrations when imaging away from the focal plane. This technique, though powerful, imposes stringent constraints on the optics and alignment required for its implementation.

In the research presented in this thesis, I have investigated multiple aspects of remote focusing - its limitations, application in live biological imaging and a possible method of improving the diffraction-limited range.

Building an Ideal RF System

An important aspect of the studies presented in the thesis is the push for wider utilisation. Given the introduction of distortions due to aberrations and scattering from the biological sample, it is essential that additional aberrations are not introduced by the RF system. When building the RF system, the factors that can ensure the best performance are:

- Standardised characterisation
- Ease of alignment

In Chapters 2 and 3, we have developed and applied a computational model for remote focusing systems that can predict the diffraction-limited range in the

presence of magnification mismatch. The study focuses on the magnification errors that can be introduced by the relay lenses as they play a vital role in satisfying the sine and Herschel condition for the RF system. Importantly, we have provided a procedure to measure the absolute magnification of the remote volume using calibration standards. An even easier method to check for magnification error has been implemented by checking the sign of the residual spherical aberration on either sides of the focal plane. With PSF measurements, it can be implemented by observing the direction of elongation of the PSF tail.

There has been work done to help microscopists choose the best combination of lenses and alignment practices for their imaging application [91]. The easiest way to ensure ideal magnification is to use the same objective for O1 and O2 therefore requiring tube lenses of equal focal lengths. For biological imaging this would mean using three water dipping or immersion objectives. Such an OPM system has been recently implemented and requires a flexible water chamber between O2 and O3 containing the immersion media during imaging [92].

Most high-NA remote focusing systems use immersion-dry pairs for O1 and O2 requiring non-standard tube lenses. Given the sensitivity of high-NA systems to small magnification mismatch - as predicted by the computational model, the design of these non-standard lenses should not degrade the volumetric imaging quality. Recent work in this direction demonstrates a method to design optimum tube lenses of the required focal length from off-the-shelf optics [93].

An extension of the computational model would be to include azimuthal terms and assess the contribution of off-axis aberrations such as coma and astigmatism at defocussed positions. Such studies can also be implemented using ray tracing software if the optical design of the objective lenses is available [89]. This can give a better understanding of the image quality across the entire 3D FOV which is of great relevance to the aberration compensation project discussed in Chapter 5 of this thesis.

Additionally, we have presented an RF system that can be easily built along

with a standard inverted microscope which reduces the complexity of the optical alignment procedure. This along with the protocol for telecentric alignment and resolution characterisation with standardised resolution and magnification metrics will lead to easier accessibility and reproduction of the setup.

The Next Generation

In chapter 4, the limits to imaging speed in the SDRF microscope were imposed by the scanning methodology. We have discussed the methods by which this hardware bottleneck can be resolved. However, the ultimate temporal limiting factor in an imaging system will be the SNR. Faster scanning would mean lesser dwell time on the ROI, increasing the relative shot noise. This is highly sample dependant but it also assumes the absence of system aberrations.

In order to ensure that the SNR is not further reduced due to aberrations from the optical system, it is important to know the experimentally attainable 3D diffraction-limited volume for a given imaging objective. This requires quantifying the contribution of both on and off-axis aberrations. This becomes especially relevant when implementing off-axis imaging systems such as in OPM, where the image planes are tilted by about 60 degrees from the native focal plane. Another aspect is the utilisation of three objectives in the RF system. In addition to increasing complexity, it reduces the optical throughput of the system. Technological innovation in this field would require to simplify the optical design and preserve the native SNR of a single objective microscope.

One approach to improve on remote focusing systems is to implement adaptive correction to compensate for residual aberrations. Following this line of thought, we built a simple adaptive correction system using the correction collar. A more robust system would be the use of adaptive optics to correct for both on and off-axis aberrations [94]. As the RF system compensates for the bulk of spherical aberration generated at defocussed positions, the DM used in the adaptive optics system would require a relatively lower mechanical stroke size to compensate for the resid-

ual aberrations. Such a microscope architecture would be complex to implement but provides the flexibility to compensate for both specimen and system induced aberrations. It should be noted here that both the collar and adaptive optics compensation can limit temporal resolution either due to the requirement of optimising an imaging metric or from SNR limitations.

Finally, I comment on the assumption made regarding the ideality of the lenses used in the RF system. Most manufacturers of tube lenses provide the lens design allowing for detailed prediction of their performance using ray tracing software. This is not the case with objectives. Without any additional compensation, the performance of an ideal RF system is ultimately limited by the optical design of the objective lens. The objectives used for biological imaging are very well corrected for aberrations across the focal plane. However, their performance at defocussed positions cannot be predicted without access to their optical design.

There are valid reasons to investigate alternate paradigms to objective and microscope architecture that can satisfy the current requirements of 3D imaging. In this regard, I highlight a patent held by Zeiss illustrating the design for a variable focal length objective lens [95]. Similar to the operation of a correction collar, the objective utilises an axially movable lens group to shift the focus and includes the arrangement for a 20x 1 NA water immersion objective. Such objectives can greatly simplify the optical design of an RF system allowing for wider utilisation. However, for successful implementation, it would have to maintain telecentricity and provide isotropic high resolution across the imaging volume.

APPENDIX A
LIST OF ACRONYMS

2PEM Two-photon excitation microscopy

BFP Back focal plane

CC Correction collar

CCD Charged coupled device

CLSM Confocal laser scanning microscopy

DM Deformable mirror

DSLM Digitally scanned laser light-sheet microscopy

ETL Electro-tunable lenses

FOV Field of view

FWHM Full-width half-maximum

GUI Graphical user interface

LED Light emitting diode

LSFM Light-sheet fluorescence microscopy

NA Numerical aperture

NFP Nominal focal plane

OPM Oblique plane microscopy

PBS Polarising beam splitter

PMT Photomultiplier Tube

PSF Point spread function

QWP Quarter wave plate

RF Remote focusing

ROI Region of interest

sCMOS Scientific complimentary metal-oxide-semiconductor

SCAPE Swept confocally-aligned planar excitation

SDRF Spinning disk remote focusing

SNR Signal-to-noise ratio

TAG Tunable acoustic gradient

APPENDIX B
DATA AVAILABILITY

We have made available some of the codes and datasets presented in this thesis on the institutional online repository ORE (Open Research Exeter).

Chapter 2: Computational model code and experimental data.
Chapter 3: PSF characterisation dataset.
`https://doi.org/10.24378/exe.2943`

Chapter 4: Dataset for resolution/telecentricity characterisation and volumetric live imaging of larvae.
`https://doi.org/10.24378/exe.2343`

BIBLIOGRAPHY

[1] David Bardell. "The invention of the microscope". In: *Bios* 75.2 (2004), pp. 78–84.

[2] Frank N Egerton. "A history of the ecological sciences, part 19: Leeuwenhoek's microscopic natural history". In: *Bulletin of the Ecological Society of America* 87.1 (2006), pp. 47–58.

[3] Tiemen Cocquyt et al. "Neutron tomography of Van Leeuwenhoek's microscopes". In: *Science Advances* 7.20 (2021), eabf2402.

[4] Robert Hooke. *Micrographia*. BoD–Books on Demand, 2020.

[5] Ernst Abbe. "Beiträge zur Theorie des Mikroskops und der mikroskopischen Wahrnehmung". In: *Archiv für mikroskopische Anatomie* 9.1 (1873), pp. 413–468.

[6] August Köhler. "New method of illumination for photomicrographical purposes". In: *Journal of the Royal Microscopical Society* 14 (1894), pp. 261–262.

[7] Stefan W Hell et al. "The 2015 super-resolution microscopy roadmap". In: *Journal of Physics D: Applied Physics* 48.44 (2015), p. 443001.

[8] Lothar Schermelleh et al. "Super-resolution microscopy demystified". In: *Nature cell biology* 21.1 (2019), pp. 72–84.

[9] Nico Scherf and Jan Huisken. "The smart and gentle microscope". In: *Nature biotechnology* 33.8 (2015), pp. 815–818.

[10] Douglas B Murphy. *Fundamentals of light microscopy and electronic imaging*. John Wiley & Sons, 2002.

[11] Yueqian Zhang and Herbert Gross. "Systematic design of microscope objectives. Part I: system review and analysis". In: *Advanced Optical Technologies* 8.5 (2019), pp. 313–347.

[12] Robert H Webb. "Confocal optical microscopy". In: *Reports on progress in physics* 59.3 (1996), p. 427.

[13] Alex Small. "Spherical aberration, coma, and the Abbe sine condition for physicists who don't design lenses". In: *American Journal of Physics* 86.7 (2018), pp. 487–494.

[14] Herbert Gross. *Handbook of Optical Systems, Volume 1, Fundamentals of Technical Optics*. Vol. 1. 2005.

[15] Peter J Shaw and David J Rawlins. "The point-spread function of a confocal microscope: its measurement and use in deconvolution of 3-D data". In: *Journal of Microscopy* 163.2 (1991), pp. 151–165.

[16] Richard W Cole, Tushare Jinadasa, and Claire M Brown. "Measuring and interpreting point spread functions to determine confocal microscope resolution and ensure quality control". In: *Nature protocols* 6.12 (2011), pp. 1929–1941.

[17] Daniel Malacara. *Optical shop testing*. Vol. 59. John Wiley & Sons, 2007.

[18] Peter Török and Fu-Jen Kao. *Optical imaging and microscopy: techniques and advanced systems*. Vol. 87. Springer, 2007.

[19] Kjell Carlsson. "The influence of specimen refractive index, detector signal integration, and non-uniform scan speed on the imaging properties in confocal microscopy". In: *Journal of Microscopy* 163 (1991).

[20] Erin E Diel, Jeff W Lichtman, and Douglas S Richardson. "Tutorial: avoiding and correcting sample-induced spherical aberration artifacts in 3D fluorescence microscopy". In: *Nature Protocols* 15.9 (2020), pp. 2773–2784.

[21] Prashant Prabhat et al. "Simultaneous imaging of different focal planes in fluorescence microscopy for the study of cellular dynamics in three dimensions". In: *IEEE transactions on nanobioscience* 3.4 (2004), pp. 237–242.

[22] Sripad Ram et al. "High accuracy 3D quantum dot tracking with multifocal plane microscopy for the study of fast intracellular dynamics in live cells". In: *Biophysical journal* 95.12 (2008), pp. 6025–6043.

[23] Sara Abrahamsson et al. "Fast multicolor 3D imaging using aberration-corrected multifocus microscopy". In: *Nature methods* 10.1 (2013), pp. 60–63.

[24] Robert Prevedel et al. "Simultaneous whole-animal 3D imaging of neuronal activity using light-field microscopy". In: *Nature methods* 11.7 (2014), pp. 727–730.

[25] Omar E Olarte et al. "Decoupled illumination detection in light sheet microscopy for fast volumetric imaging". In: *Optica* 2.8 (2015), pp. 702–705.

[26] Florian O Fahrbach et al. "Rapid 3D light-sheet microscopy with a tunable lens". In: *Optics express* 21.18 (2013), pp. 21010–21026.

[27] SeungYeon Kang, Martí Duocastella, and Craig B Arnold. "Variable optical elements for fast focus control". In: *Nature Photonics* 14.9 (2020), pp. 533–542.

[28] Yuichiro Nakai et al. "High-speed microscopy with an electrically tunable lens to image the dynamics of in vivo molecular complexes". In: *Review of Scientific Instruments* 86.1 (2015), p. 013707.

[29] Rory M Power and Jan Huisken. "Adaptable, illumination patterning light sheet microscopy". In: *Scientific reports* 8.1 (2018), pp. 1–11.

[30] M Bawart et al. “Remote focusing in confocal microscopy by means of a modified alvarez lens”. In: *Journal of Microscopy* 271.3 (2018), pp. 337–344.

[31] Mantas Žurauskas et al. “Rapid adaptive remote focusing microscope for sensing of volumetric neural activity”. In: *Biomedical optics express* 8.10 (2017), pp. 4369–4379.

[32] Edward J Botcherby et al. “An optical technique for remote focusing in microscopy”. In: *Optics Communications* 281.4 (2008), pp. 880–887.

[33] José-Angel Conchello and Jeff W Lichtman. “Optical sectioning microscopy”. In: *Nature methods* 2.12 (2005), pp. 920–931.

[34] Ruth Rebecca Sims. “Volumetric Imaging Across Spatiotemporal Scales in Biology with Fluorescence Microscopy”. PhD thesis. University of Cambridge, 2019.

[35] CJR Sheppard and XQ Mao. “Confocal microscopes with slit apertures”. In: *Journal of Modern Optics* 35.7 (1988), pp. 1169–1185.

[36] R Juskaitis et al. “Efficient real-time confocal microscopy with white light sources”. In: *Nature* 383.6603 (1996), pp. 804–806.

[37] Fritjof Helmchen and Winfried Denk. “Deep tissue two-photon microscopy”. In: *Nature methods* 2.12 (2005), pp. 932–940.

[38] Maria Göppert-Mayer. “Elementary processes with two quantum transitions”. In: *Annalen der Physik* 18.7-8 (2009), pp. 466–479.

[39] Lina Streich et al. “High-resolution structural and functional deep brain imaging using adaptive optics three-photon microscopy”. In: *Nature methods* 18.10 (2021), pp. 1253–1258.

[40] Gert-Jan Bakker et al. “Intravital deep-tumor single-beam 3-photon, 4-photon, and harmonic microscopy”. In: *Elife* 11 (2022), e63776.

[41] Siegfried Weisenburger et al. “Volumetric Ca2+ imaging in the mouse brain using hybrid multiplexed sculpted light microscopy”. In: *Cell* 177.4 (2019), pp. 1050–1066.

[42] Francesca Anselmi et al. “Three-dimensional imaging and photostimulation by remote-focusing and holographic light patterning”. In: *Proceedings of the National Academy of Sciences* 108.49 (2011), pp. 19504–19509.

[43] Erich E Hoover et al. “Remote focusing for programmable multi-layer differential multiphoton microscopy”. In: *Biomedical optics express* 2.1 (2011), pp. 113–122.

[44] Nicholas James Sofroniew et al. “A large field of view two-photon mesoscope with subcellular resolution for in vivo imaging”. In: *elife* 5 (2016), e14472.

[45] Jerome Mertz. “Optical sectioning microscopy with planar or structured illumination”. In: *Nature methods* 8.10 (2011), pp. 811–819.

[46] Peter A Santi. "Light sheet fluorescence microscopy: a review". In: *Journal of Histochemistry & Cytochemistry* 59.2 (2011), pp. 129–138.

[47] Steffen Lindek and Ernst HK Stelzer. "Confocal theta microscopy and 4Pi-confocal theta microscopy". In: *Three-dimensional microscopy: image acquisition and processing*. Vol. 2184. SPIE. 1994, pp. 188–194.

[48] Steffen Lindek, Rainer Pick, and Ernst HK Stelzer. "Confocal theta microscope with three objective lenses". In: *Review of scientific instruments* 65.11 (1994), pp. 3367–3372.

[49] Arne H Voie and Francis A Spelman. "Three-dimensional reconstruction of the cochlea from two-dimensional images of optical sections". In: *Computerized medical imaging and graphics* 19.5 (1995), pp. 377–384.

[50] J Huisken et al. "Live Embryos by Selective Plane Illumination Microscopy". In: *Science* (), pp. 13–16.

[51] Hosein Kafian et al. "Light-sheet fluorescence microscopy with scanning non-diffracting beams". In: *Scientific reports* 10.1 (2020), pp. 1–12.

[52] Sébastien Wolf et al. "Whole-brain functional imaging with two-photon light-sheet microscopy". In: *Nature methods* 12.5 (2015), pp. 379–380.

[53] C Dunsby. "Optically sectioned imaging by oblique plane microscopy". In: *Optics express* 16.25 (2008), pp. 20306–20316.

[54] Matthew B Bouchard et al. "Swept confocally-aligned planar excitation (SCAPE) microscopy for high-speed volumetric imaging of behaving organisms". In: *Nature photonics* 9.2 (2015), pp. 113–119.

[55] Bin Yang et al. "Epi-illumination SPIM for volumetric imaging with high spatial-temporal resolution". In: *Nature methods* 16.6 (2019), pp. 501–504.

[56] Alfred Millett-Sikking and Andrew York. *AndrewGYork/high_na_single_objective_lightsheet: Work-in-progress*. Version 0.0.2. Aug. 2019. DOI: 10.5281/zenodo.3376243. URL: https://doi.org/10.5281/zenodo.3376243.

[57] Etai Sapoznik et al. "A versatile oblique plane microscope for large-scale and high-resolution imaging of subcellular dynamics". In: *Elife* 9 (2020), e57681.

[58] Younghoon Shin, Dongmok Kim, and Hyuk-Sang Kwon. "Oblique scanning 2-photon light-sheet fluorescence microscopy for rapid volumetric imaging". In: *Journal of biophotonics* 11.5 (2018), e201700270.

[59] Penelope F Lawton et al. "Multi-plane remote refocusing epifluorescence microscopy to image dynamic Ca 2+ events". In: *Biomedical Optics Express* 10.11 (2019), pp. 5611–5624.

[60] Sharika Mohanan and Alexander David Corbett. "Sensitivity of remote focusing microscopes to magnification mismatch". In: *Journal of Microscopy* (2021).

[61] Michele Gintoli et al. “Spinning disk-remote focusing microscopy”. In: *Biomedical Optics Express* 11.6 (2020), pp. 2874–2888.

[62] Kevin T Takasaki, Dmitri Tsyboulski, and Jack Waters. “Dual-plane 3-photon microscopy with remote focusing”. In: *Biomedical Optics Express* 10.11 (2019), pp. 5585–5599.

[63] CJR Sheppard. “Aberrations in high aperture optical systems”. In: *Optik* 105.1 (1997), pp. 29–33.

[64] Max Born et al. *Principles of Optics: Electromagnetic Theory of Propagation, Interference and Diffraction of Light*. 7th ed. Cambridge University Press, 1999. DOI: 10.1017/CBO9781139644181.

[65] Joseph J. M. Braat. “Abbe sine condition and related imaging conditions in geometrical optics”. In: *Fifth International Topical Meeting on Education and Training in Optics*. Ed. by Christiaan H. F. Velzel. Vol. 3190. International Society for Optics and Photonics. SPIE, 1997, pp. 59–64. URL: https://doi.org/10.1117/12.294417.

[66] Virendra N Mahajan. “Zernike polynomials and aberration balancing”. In: *Current Developments in Lens Design and Optical Engineering IV*. Vol. 5173. International Society for Optics and Photonics. 2003, p. 517302.

[67] Christopher Wilcox. *Zernike Polynomial Coefficients for a given Wavefront using Matrix Inversion in Matlab*. 2020. URL: https://www.mathworks.com/matlabcentral/fileexchange/27072-zernike-polynomial-coefficients-for-a-given-wavefront-using-matrix-inversion-in-matlab.

[68] Virendra N Mahajan. “Strehl ratio for primary aberrations: some analytical results for circular and annular pupils”. In: *JOSA* 72.9 (1982), pp. 1258–1266.

[69] Johannes Pfund, Norbert Lindlein, and Johannes Schwider. “Misalignment effects of the Shack–Hartmann sensor”. In: *Applied optics* 37.1 (1998), pp. 22–27.

[70] Guang-ming Dai. *Wavefront optics for vision correction*. Vol. 179. SPIE press, 2008.

[71] Martin Thomas. *Multifocus Imager Theory and Practice*. [Online; accessed 9-January-2022]. 2017. URL: https://www.cairn-research.co.uk/wp-content/uploads/2015/10/Martin-Thomas-Objective-Theory-Oct-2017.pdf/.

[72] Aadhar Jain, Allen HJ Yang, and David Erickson. “Gel-based optical waveguides with live cell encapsulation and integrated microfluidics”. In: *Optics letters* 37.9 (2012), pp. 1472–1474.

[73] Patrick Theer, Cyril Mongis, and Michael Knop. “PSFj: know your fluorescence microscope”. In: *Nature methods* 11.10 (2014), pp. 981–982.

[74] CJR Sheppard and HJ Matthews. "Imaging in high-aperture optical systems". In: *Josa a* 4.8 (1987), pp. 1354–1360.

[75] Alexander D Corbett et al. "Microscope calibration using laser written fluorescence". In: *Optics express* 26.17 (2018), pp. 21887–21899.

[76] Aurox Ltd. *Brochures & Application notes*. URL: https://www.aurox.co.uk/brochures.php.

[77] Nadine Randel et al. "Neuronal connectome of a sensory-motor circuit for visual navigation". In: *elife* 3 (2014), e02730.

[78] Albina Asadulina et al. "Whole-body gene expression pattern registration in Platynereis larvae". In: *EvoDevo* 3.1 (2012), pp. 1–13.

[79] Edward J Botcherby et al. "Real-time extended depth of field microscopy". In: *Optics express* 16.26 (2008), pp. 21843–21848.

[80] Bin Yang et al. "DaXi—high-resolution, large imaging volume and multi-view single-objective light-sheet microscopy". In: *Nature Methods* (2022), pp. 1–9.

[81] Pamela A Muriello and Kenneth W Dunn. "Improving signal levels in intravital multiphoton microscopy using an objective correction collar". In: *Optics communications* 281.7 (2008), pp. 1806–1812.

[82] HW Yoo et al. "Automated spherical aberration correction in scanning confocal microscopy". In: *Review of Scientific Instruments* 85.12 (2014), p. 123706.

[83] Raphaël Turcotte, Yajie Liang, and Na Ji. "Adaptive optical versus spherical aberration corrections for in vivo brain imaging". In: *Biomedical optics express* 8.8 (2017), pp. 3891–3902.

[84] Rimas Juškaitis. "Measuring the real point spread function of high numerical aperture microscope objective lenses". In: *Handbook of biological confocal microscopy*. Springer, 2006, pp. 239–250.

[85] MJ Booth and T Wilson. "Strategies for the compensation of specimen-induced spherical aberration in confocal microscopy of skin". In: *Journal of microscopy* 200.1 (2000), pp. 68–74.

[86] Dejan. *How To Control a Stepper Motor with A4988 Driver and Arduino*. [Online; accessed 9-January-2022]. 2015. URL: https://howtomechatronics.com/tutorials/arduino/how-to-control-stepper-motor-with-a4988-driver-and-arduino/.

[87] RJMM Arimoto and JM Murray. "A common aberration with water-immersion objective lenses". In: *Journal of microscopy* 216.1 (2004), pp. 49–51.

[88] Jonathan Kurvits, Mingming Jiang, and Rashid Zia. *Zemax (optical design) files of microscope objectives, tube lenses, and Fourier imaging setups*. 2015. DOI: 10.6084/M9.FIGSHARE.1481270.V3. URL: https://figshare.com/articles/dataset/Zemax_optical_design_files_of_microscope_objectives_tube_lenses_and_Fourier_imaging_setups/1481270/3.

[89] Jonathan A Kurvits, Mingming Jiang, and Rashid Zia. "Comparative analysis of imaging configurations and objectives for Fourier microscopy". In: *JOSA A* 32.11 (2015), pp. 2082–2092.

[90] Toshinobu Suzuki. *Immersion microscope objective*. US Patent 5,517,360. May 1996.

[91] Alfred Millett-Sikking et al. *calico/remote_refocus: Pre-print*. Version v0.1. Jan. 2018. DOI: 10.5281/zenodo.1146084. URL: https://doi.org/10.5281/zenodo.1146084.

[92] Manish Kumar et al. "Crossbill: an open access single objective light-sheet microscopy platform". In: *Biorxiv* (2021).

[93] Wenzhi Hong and Chris Dunsby. "Automatic tube lens design from stock optics for microscope remote-refocusing systems". In: *Optics Express* 30.3 (2022), pp. 4274–4287.

[94] Karen M Hampson et al. "Adaptive optics for high-resolution imaging". In: *Nature Reviews Methods Primers* 1.1 (2021), pp. 1–26.

[95] Thomas Nobis. *Arrangement for changing the focus of a microscope objective*. US Patent 9,696,536. July 2017.